Low Pressure Plasmas in Magnetic Nozzles

Alexander Declan Bennet

A thesis submitted for the degree of
Doctor of Philosophy
of The Australian National University

June 2019

Declaration

This thesis is an account of research undertaken between August 2015 and June 2019 at the Research School of Physics and Engineering, College of Science, The Australian National University, Canberra, Australia.

Except where acknowledged in the customary manner, the material presented in this thesis is, to the best of my knowledge, original and has not been submitted in whole or part for a degree in any university.

Alexander Declan Bennet

29th October 2019

Acknowledgments

Completing this thesis would not have been possible without the support and encouragement of the wonderful people around me throughout my time in Canberra. First and foremost, I would like to thank my fantastic supervisor Christine Charles, without whom I never would have even started a PhD. Christine gave me the freedom to get my hands dirty, try new things and explore the lab at my own speed while knowing that there was a watchful eye ensuring that my work remained both relevant and interesting. The most rewarding moments of my PhD were those when I felt that we were working as a team to solve a problem in the lab or figure out the missing link in the narrative of a paper. Four years would be just as long for a supervisor as it is for a student so thank you for putting your faith in me, for your unwavering interest in my research and for your guidance throughout my time at SP3.

This lab has an incredibly open, honest and collegial culture and no one embodies these traits more than Rod Boswell. Rod's ability to simplify and communicate concepts in plasma physics was invaluable for my education as a physicist and my ability to intuitively understand the systems that I worked with. Rod's door was always open to me when I was looking for help and I was always met with equal doses of good humour and healthy scepticism. More often than not, our discussions over lunch or in Rod's office would turn philosophical and, while I didn't always understand what we were talking about, I always learned something new about the world or a new perspective to view it through. Both Christine and Rod have been instrumental in my development as a scientist and an engineer, and I would like to thank you both for your friendship past, present and future.

All of the experiments reported in this thesis would not have been possible if not for the expert knowledge and craftsmanship of Peter Alexander. I had the absolute privilege of working closely with Peter during the design and construction of the Echidna plasma reactor and I am very grateful for being able to spend so much time learning from and becoming friends with such a genial, open and honest person (he's also a fellow Saints supporter which is a big tick). I know that Peter will be sorely missed by the lab when he finally does retire for the second time.

During my time with SP3 I have shared the labs with a number of excellent students and collaborators who became great friends along the journey and made completing this PhD that much easier. My sincerest thanks go to my fellow PhD students within SP3: Yunchao who answered my countless questions about plasma physics and taught me all about diagnostic probes and the Chi Kung reactor; Andy who taught me the ins and outs of CFD-ACE+ plasma simulations; and Dimitris from whom I have learned so much about radiofrequency engineering and electronics. Similarly, it was a pleasure to work with Andrew, Kazu, Ashley, Alex 2, Thomas, Felicien, Scott, Broden and Matt during their various stints in SP3.

The CPF hallway was far more than just an office space to me and it was never hard to find a smiling face or someone to laugh with. Thanks must go to Michael for his tireless efforts as HoD and to the rest of the fluids group for all of the advice and support. I shared many fruitful and interesting discussions with Horst, Hua, Nico, Sunny, Jia, JB, Mahdi, Tobias and Florian while playing squash, stinking out the corridor with raclette, cooking wood-fired pizzas and having lunch in the tea room.

RSPE is a peculiar place but my time here was made all the better by a number of people who supported my research in a variety of different ways. Special thanks to Stuart for all of the useful discussions we had about plasmas, especially when I was trying to get my head around the compensated probe. Solutions to administrative matters were always easy to find thanks to help from Uyen, Susie, Gaye, Sonia, Nikki, Karen and Luda, and the friendly faces of Jo and Gale in the tea room made starting each day that little bit easier with a coffee in hand. I spent plenty of time with Goran, Patricio, Ben and the rest of the Stores team looking for obscure parts and always enjoyed their good-humoured sarcasm. Many thanks must also go to Luke, Dennis, Paul, David and the rest of the EU team who always had a solution to my electrical woes, taught me a lot about electronics and never balked when I walked in with some bizarre new idea.

I am very lucky to have made a number of good friends through my time at Bruce Hall who helped to make my first year particularly unproductive in the best way possible. I was very fortunate to get to know a number of people through many afternoons and Sunday mornings playing baseball for the Ainslie-Gungahlin Baseball Club and it was the people more than the baseball that brought me back three years in a row. A special thank you must go to Matt and Karen Conway who frequently had me over for dinner and made me feel like I was really part of their family. Through lucky coincidence, my time in Canberra crossed over almost perfectly with Tom Adolph who I must thank for his many hours preparing for and running our D&D sessions, introducing me to the rest of the group and giving me a bit of home away from home. I have been very fortunate to live with Max, Will and Brendan who have really

made our house in Lyneham feel like a home. Special thanks to Will who has become a close friend over the last 2 years, in which time we have shared many visits to the friendliest of golf courses and the Old Canberra Inn.

I would like to acknowledge and wholeheartedly thank my Mum for everything that she has done for me and all that she continues to do for our family. She has been a pillar of support throughout my life and has always encouraged and empowered me to follow my heart and do what interests me most. I also need to say a big thank you to Dad and Kaarina for all of the many lunches and dinners that we've shared, the weeks I've spent skiing with you and all of the support that you've provided along my journey through universities. I have been very lucky to have siblings spread across Australia, meaning that family is never too far away. I will always be grateful for the generosity of Stacey, Michael, David and their families who were always keen to hear about my studies and give me advice or a couch to sleep on during my jaunts away from Canberra.

Last, but certainly not least, I would like to thank my wonderful partner Camilla for nearly two years of love and support. I can't thank you enough for patiently sitting through many hours of me talking about plasma physics, for your empathy and understanding during the harder times of my PhD, and for continually motivating me to push through.

Publications

This thesis has resulted in the following publications in peer reviewed journals:

C. Charles, T. S. Ho, A. Pascale, T. Charoy, **A. Bennet**, A. Stuchbery, R. W. Boswell, W. Liang, L. Raymond and J. Rivas-Davila.
The Pocket Rocket electro-thermal plasma thruster for 'CubeSat' nano-satellites
International Astronautical Congress, Adelaide, Sept 2017.

A. Bennet, K Takahashi, C. Charles, A Bish, R. Boswell, A. Ando, R. Georges and A. Benidar.
The mini-helicon thruster for 'CubeSat' nano-satellites: experiments and simulations
International Astronautical Congress, Adelaide, Sept 2017.

A. Bennet, C. Charles and R. Boswell.
In situ *electrostatic characterisation of ion beams in the region of ion acceleration*
Physics of Plasmas, Vol. 25, p. 023516, 2018.

A. Bennet, C. Charles and R. Boswell.
Separating the location of geometric and magnetic expansions in low-pressure expanding plasmas
Plasma Sources Science and Technology, Vol. 27, p. 075003, 2018.

A. Bennet, C. Charles and R. Boswell.
Selective radial release of hot, magnetised electrons downstream of a low-pressure expanding plasma
Journal of Physics D: Applied Physics, Vol. 51, p. 375204, 2018.

A. Bennet, C. Charles and R. Boswell.

Field-aligned Boltzmann electric triple layer in a low-pressure expanding plasma

Plasma Sources Science and Technology Letters, Vol. 28, p. 06LT01, 2019.

A. Bennet, C. Charles and R. Boswell.

Non-local plasma generation in a magnetic nozzle

Physics of Plasmas, Vol. 26, p. 072107, 2019.

Abstract

This thesis details experiments of low pressure plasmas interacting with magnetic nozzles in two different plasma reactors. In the Chi Kung reactor, a radiofrequency (RF) plasma is created in the throat of the magnetic nozzle and is allowed to expand through the diverging field. Under the experimental conditions used in this thesis (0.3-0.7 mTorr argon, 145 Gauss peak axial magnetic field, 315 W RF power), a current-free double layer is measured on axis and its characteristics are explored with *in-situ* diagnostic probes as the argon pressure is increased. With increasing pressure, the magnitude of the potential drop and beam velocity decrease. The axial beam velocity profiles are consistent with those previously published using an *ex-situ* laser technique, giving confidence in the *in-situ* measurements and allowing for reliable measurement of the beam density.

The axial plasma properties in Chi Kung were measured when a pyrex extension tube was inserted in the expansion region, thereby separating the geometric and magnetic expansions. The plasma density in the source region increased and the peak velocity of the ion beam decreased. With the extension tube inserted, measurements of the electron transport showed that those electrons that would normally ionise high-density conics downstream are blocked by the extension tube and increase the rate of ionisation in the source. The extension tube was then positioned further downstream, creating a window through which these electrons could pass. With increasing window sizes, the conics were seen to reform and the beam characteristics return to the standard case, thereby demonstrating the relationship between the conics and the ion beam.

The field-aligned electron transport from the plasma source to the region of high-density conics was investigated by measuring the plasma potential and density along the most radial magnetic field line to escape the source region. The results demonstrate an electric triple layer at the point where the magnetic field line passes closest to the radial wall. This is found to be due to negative charging of the radial wall and the build up of negative charges repel the electrons streaming along the field line.

In the Echidna reactor, a solenoidal magnetic field and RF plasma source are progressively

separated meaning the plasma is incident on an increasingly distant converging magnetic nozzle. For 1 mTorr argon, 300 Gauss maximum axial magnetic field and 200 W RF power, axial plasma density profiles measured in the Echidna reactor showed two regimes of operation depending on the ion magnetisation under the RF antenna. When ions are magnetised, electrons heated by the antenna are effectively transported along a column defined by the converging magnetic field lines and increase in density as the cross-section decreases. The peak density is located underneath the antenna and the system appears to behave in a Boltzmann-like manner. When ions are unmagnetised under the antenna, electrons are not as effectively transported to the region of high magnetic field strength, resulting in a doubly-peaked axial density profile where one peak is under the solenoids and the other is under the RF antenna.

Contents

Chapter 1

Introduction

1.1 Plasma

This thesis details research on the behaviour of low pressure (10^{-4} to 10^{-3} Torr) plasmas interacting with magnetic nozzles. Low pressure plasmas in magnetic fields are found throughout the universe, from the accretion disks surrounding black holes to the aurorae at the Earth's magnetic poles [1, 2]. While the study of these plasmas helps to understand astrophysical processes, interest in this area has been piqued over the last few decades due to its relevance to the microelectronics manufacturing and electric propulsion communities. For those interested in microelectronics, low-pressure plasmas provide an indispensable tool for uniformly and precisely etching trenches out of silicon wafers which can then be filled with conductors using a separate plasma process [3, 4]. Plasma processes have allowed for giant leaps in the semiconductor industry, boosting the performance and availability of computers, smart phones and other consumer electronics. For the electric propulsion community, research into low-pressure magnetised plasmas is key to understanding the behaviour of plasma thrusters - highly fuel efficient forms of propulsion used in space. Plasma thrusters such as gridded ion and Hall effect thrusters can offer over tenfold improvements in fuel efficiency over the classical chemical propulsion used to launch rockets from the face of the Earth into orbit and beyond [5, 6]. One type of electric propulsion device is the helicon thruster which accelerates a high-density plasma through a magnetic nozzle, allowing it to expand into space [7]. The plasma dynamics in these devices is not fully understood, hence experimental investigation is required to better understand their operation and design future thrusters.

This chapter gives an introduction to low-pressure magnetised plasmas, their general properties and how they are made in the laboratory. This is followed by literature studies of previous experimental work done on plasmas in diverging and converging magnetic field geometries,

areas which are pertinent to understanding helicon plasma thrusters.

1.1.1 General properties

Transitions between states of matter occur with the addition of energy [8]. Take water, for example. Below its freezing point of 0 °C it exists as solid ice for standard atmospheric pressure conditions. By adding energy in the form of heat, the temperature increases and with the addition of enough heat to overcome the latent heat of fusion, it becomes liquid water. With the addition of even more heat, the temperature will reach the boiling point of 100 °C. With enough energy to overcome the latent heat of vaporisation, the liquid water transitions to the gaseous state as steam. These three states of matter account for the vast majority of substances that we encounter in everyday life on Earth. Plasma, however, is far more abundant throughout the universe and is regularly referred to as the fourth state of matter [2, 3]. It can be described as a superheated gas in which the particles have enough energy for molecular dissociation and ionisation collisions to occur. Formally, it is a quasineutral gas of charged particles that demonstrates collective behaviour when subjected to external electric and magnetic fields. Plasmas can contain a wide variety of species including electrons, positive ions, negative ions, neutral atoms and neutral molecules. The low-pressure plasmas discussed in this thesis are made by ionising neutral argon gas, meaning that they only contain neutral background argon atoms, electrons and positive argon ions in any significant amount. As such, the rest of the discussion presented here on general properties of plasmas will be focused on electropositive argon plasmas.

The requirement of quasineutrality means that there must be equal numbers of ions and electrons in the bulk plasma, i.e. $n_i = n_e = n$ where n_i is the ion number density, n_e is the electron number density and n is the plasma number density [3, 9]. This is understandable given that plasmas in the laboratory are made from a neutral gas, meaning that there are equal numbers of positive and negative charges to begin with. If the quasineutrality condition is violated, electric fields will develop in order to restore neutrality, e.g. if the plasma loses electrons to a physical wall and becomes positively charged it will repel ions, accelerating them out of the plasma until it returns to neutrality. However, charge imbalances resulting in electric potential differences much less than the electron temperature (T_e) are permitted over a short length scale know as the Debye length (λ_{De}). λ_{De} is a function of T_e and the plasma density (n), and can be calculated using equation 1.1.

$$\lambda_{De} = \left(\frac{\epsilon_0 T_e}{qn} \right)^{1/2} \tag{1.1}$$

In equation 1.1, $\epsilon_0 = 8.854 \times 10^{-12}$ F/m is the permittivity of free space and $q = 1.602 \times$

10^{-19} C is the elementary charge. For a low-pressure argon plasma typical of those discussed in this thesis, $T_e \sim 8$ eV and $n \sim 10^{10}$ cm^{-3}, yielding a Debye length of approximately 200 μm. As such, the scale length over which charge imbalances are permitted within the plasma is significantly smaller than the size of the experimental apparatus that are used in this thesis (described in chapter 2).

Both the ions and electrons in these plasmas are normally defined by single or multiple Maxwellian energy distribution functions characterised by a temperature and density [3]. In the low pressure plasmas discussed in this thesis, the electrons and ions are not in thermal equilibrium and the ion temperature, T_i, is orders of magnitude lower than the electron temperature, T_e, i.e. $T_i << T_e$. In fact, while electron temperatures are typically in the range of 2 eV to 10 eV (i.e. 20000 K to over 100000 K), ions are mostly in thermal equilibrium with background neutrals which are at or around room temperature. With increasing power and ionisation fraction, the ion temperature can approach the electron temperature, e.g. in fusion devices, however the plasmas in this thesis typically feature quite low ionisation and are strongly out of thermal equilibrium. Given that the mass of an electron, $m_e = 9.109\times10^{-31}$ kg, is significantly smaller than the mass of an argon atom or ion, $M_{Ar} \simeq M_{Ar^+} = 6.634\times10^{-26}$ kg, the thermal velocity of ions (qT_i/M_{Ar}) and electrons (qT_e/m_e) are extremely different and the significantly lighter electrons are much more mobile. Because of this, electron dynamics dominate the plasma behaviour [3]. These plasmas are typically weakly ionised, i.e. $n_i = n_e << n_g$ where n_g is the neutral gas density, which means that collisions between ions, electrons and neutral atoms dominate plasma behaviour. For a simple monatomic species like argon the situation is much more simple than for molecules, which have rotation and vibration modes that can be excited through collisions. In reality, even argon plasmas present a complex set of collision reactions, however they can broadly be categorised into elastic, exciting and ionising collisions [3, 9]:

$$\mathrm{Ar} + \mathrm{e} \rightarrow \mathrm{Ar} + \mathrm{e} \qquad \text{(Elastic)}$$

$$\mathrm{Ar} + \mathrm{e} \rightarrow \mathrm{Ar}^* + \mathrm{e} \qquad \text{(Exciting)}$$

$$\mathrm{Ar} + \mathrm{e} \rightarrow \mathrm{Ar}^+ + 2\mathrm{e} \qquad \text{(Ionising)}$$

Elastic collisions refer to those which preserve kinetic energy throughout the reaction. In inelastic collisions, some of the initial kinetic energy is used in either excitation or ionising processes. In excitation reactions, kinetic energy is transferred to electrons orbiting an argon atom or ion and causes these electrons to enter higher energy levels. Deexcitation can also occur through the release of a photon, causing electrons to transition to lower energy levels, which is why plasmas are seen to glow. There is a threshold energy under which excitation

reactions do not occur and this is 12.14 eV in argon [3, 9]. Similarly, ionisation reactions, which create electrons and ions, cannot occur for energies under the ionisation energy of argon which is 15.76 eV. As the electron population is much hotter than the ion populations, the initial energy in these collision reactions is almost entirely due to the kinetic energy of the incident electron. As such, the rate of excitation and ionisation reactions is directly related to the temperature of the electron population, T_e.

When a plasma is in contact with a solid boundary, as is the case in laboratory plasmas, the mobile electrons will leave the bulk plasma faster than ions if they are not contained in some way. If electrons leave the plasma and reach an absorbing boundary, the quasineutrality condition will be violated unless ions also leave at the same rate. In order to achieve this, a narrow region of strong electric field, named a sheath, is generated just in front of the wall and serves to contain electrons and eject ions [2, 3, 9]. The magnitude of the electric field is such that the flux of electrons and ions to the wall are equal, thereby maintaining the quasineutrality condition in the bulk plasma. The existence of the sheath means that the bulk plasma exists at an electric potential greater than that of the wall. This potential is known as the plasma potential (V_p). The electric potential in the sheath is significantly negative compared to the plasma potential, hence the electron density decreases rapidly and quasineutrality is violated in this region.

Figure 1.1 shows a diagram of the potential structure in a 1-D plasma exisiting between two absorbing walls separated by a distance d. In the centre of the plasma, there are no strong electric fields present and the potential profile is flat and equal to the plasma potential, V_p. The sheaths are visible as sharp decreases in the plasma potential profile within a distance s of the walls and create an electric field, E, directed towards the walls. This electric field accelerates ions away from the bulk plasma while impeding electron transport to the wall. If the walls are electrically insulated then they can float to some arbitrary voltage, V_f, known as the floating potential. However, if the wall is grounded or set to some fixed voltage then the plasma potential will adjust to account for this such that the magnitude of the sheath remains the same. The magnitude of the sheath voltage, i.e. the difference between V_p and V_f, can be calculated using equation 1.2.

$$V_s = V_p - V_f = \frac{T_e}{2} \ln\left(\frac{M_{Ar}}{2\pi m_e}\right) \simeq 4.7 \times T_e \tag{1.2}$$

where T_e has units of eV, V_s is the magnitude of the sheath voltage, V_f is the absolute floating potential of the wall and $k = 1.38 \times 10^{-23}$ J/K is the Boltzmann constant. For the typical argon plasma properties discussed earlier, i.e. $T_e = 8$ eV, the sheath potential would be approximately 37.5 V. The width of the sheaths, s, can be estimated using the Child law in

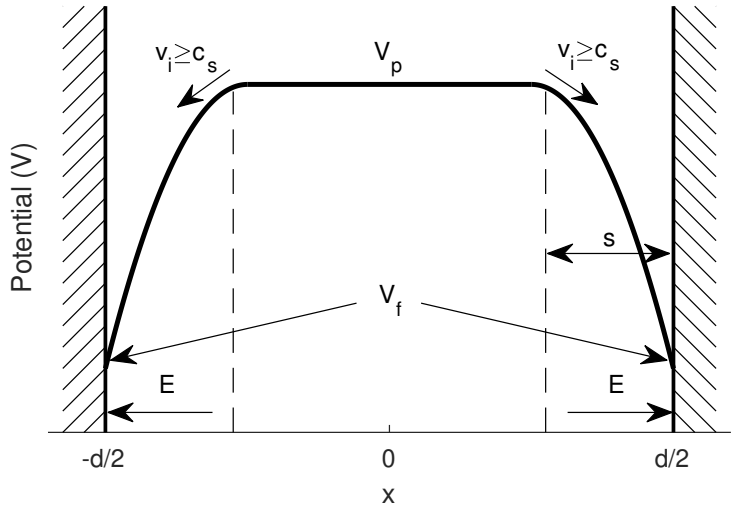

Figure 1.1: Generalised potential structure of a 1-D plasma contained between two absorbing walls. The bulk plasma has a flat potential profile at the plasma potential, V_p, and contains no large electric fields. The large potential drop within s of the walls is the sheath and creates an electric field, E, towards the wall. Ions entering the sheath must do so with a velocity greater than or equal to the local ion sound speed, i.e. $v_i \geq c_s$. If the wall is electrically insulating then it will charge to the floating potential V_f.

equation 1.3 [3].

$$s = \frac{\sqrt{2}}{3}\lambda_{De}\left(\frac{2V_s}{T_e}\right)^{3/4} \tag{1.3}$$

Equation 1.3 shows that the width of the sheath is on the order of the Debye length but with some extra dependence on the electron temperature and the sheath potential. For the typical plasma with $T_e = 8$ eV, $n_i = 10^{10}$ cm^{-3} and the calculated sheath voltage of 37.5 V above, the sheath width would be about 500 μm, i.e. very thin compared the typical size of vacuum chambers used to study these low pressure plasmas.

Ions entering the sheath must do so with a velocity, v_i, at or above the local ion sound speed, c_s [10]. This is known as the Bohm criterion and is necessary to balance the flux of ions and electrons to the wall. The local ion sound speed can be calculated using equation 1.4.

$$c_s = \sqrt{\frac{qT_e}{M_{Ar}}} \tag{1.4}$$

where T_e is in units of eV.

The requirement that ions must enter the sheath with a velocity $v_i \geq c_s$ means that there must be some electric field which accelerates ions before they reach the sheath edge. Indeed,

this is the case and the accelerating structure is known as the presheath (not shown in figure 1.1). By calculating the kinetic energy of the ion entering the sheath, the presheath potential drop is found to be equal to $T_e/2$. Therefore, a plasma with $T_e = 8$ eV would require a presheath potential drop of 4 V and the ion sound speed is about 4400 m/s.

If the electron population in a plasma is isothermal then there is a direct relationship between the potential profile and the electron density [9]. This is known as Boltzmann equilibrium and the plasma potential can be expressed by the Boltzmann relation in equation 1.5.

$$V_p(x) = V_p(x_0) + T_e ln[\frac{n_e(x)}{n_e(x_0)}] \tag{1.5}$$

where $V_p(x)$ and $n_e(x)$ are the plasma potential and electron density at some position x and $V_p(x_0)$ and $n_e(x_0)$ are the plasma potential and electron density at some initial position x_0. As electrons are very light, they will be accelerated to high velocities quickly by potential differences in the plasma [2]. Ions are not accelerated to the same velocities and would therefore violate the quasineutrality condition locally. Therefore, the Boltzmann relation essentially balances the flux of ions and electrons to maintain this condition. However, as will be seen in the next section, plasmas in a magnetic field behave differently to unmagnetised plasmas and the Boltzmann relation only holds along each magnetic field line, describing the field-aligned transport behaviour [2].

1.1.2 Magnetised plasmas

Plasmas are made up of charged particles and can therefore interact with magnetic fields. Interactions with both electric and magnetic fields are primarily due to the Lorentz force, which is given by equation 1.6 [2, 11].

$$\mathbf{F} = q(\mathbf{E} + \mathbf{v} \times \mathbf{B}) \tag{1.6}$$

where $\mathbf{F}$ is the resultant force vector acting on a charged particle, $\mathbf{E}$ is the local electric field vector, $\mathbf{v} \times \mathbf{B}$ is the cross product of the charged particle's velocity vector, $\mathbf{v}$, and the local magnetic field vector $\mathbf{B}$. In the bulk plasma away from any significant variations in the plasma potential, contributions to $\mathbf{F}$ from the electric field are small. As such, the particle motion is dominated by $\mathbf{v} \times \mathbf{B}$ term. In the case where $\mathbf{E}$ is negligible and $\mathbf{v}$ is parallel to $\mathbf{B}$, there is no force on the particle. When $\mathbf{v}$ is not parallel to $\mathbf{B}$, the resultant force on the particle is perpendicular to both $\mathbf{v}$ and $\mathbf{B}$ and causes it to rotate around the magnetic field line. Therefore, the motion of a charged particle in the presence of a constant magnetic field is helical with perpendicular velocity components contributing to circular motion around the

magnetic field lines and parallel components defining its velocity along the field lines. The radius of the orbit around the magnetic field line is called the Larmor radius, r_L and can be calculated using equation 1.7 [2, 3].

$$r_L = \frac{mv_\perp}{NqB} \tag{1.7}$$

where m is the mass of the particle, $v_\perp$ is the component of the particle's velocity perpendicular to $\mathbf{B}$, N is the charge number of the particle and B is the magnetic field strength. For the plasmas discussed in this thesis, argon is only singly ionised in any significant amount, meaning that $N = 1$ for all charged particles. The cyclotron frequency, i.e. the frequency at which charged particles rotate about a magnetic field line, is independent of the perpendicular velocity and can be calculated using equation 1.8 [2, 3].

$$\omega_c = \frac{NqB}{m} \tag{1.8}$$

where ω_c is the cyclotron frequency.

The magnetic field strengths used in this thesis are typically around 150 Gauss. The thermal velocity of electrons with an electron temperature of 8 eV is approximately 1.2×10^6 m/s. Therefore, using equation 1.7 the electron Larmor radius, r_{Le}, is found to be approximately 0.5 mm. Similarly, for a thermal velocity of 400 m/s, the ion Larmor radius, r_{Li}, in an argon plasma is calculated to be about 1 cm. The difference between r_{Le} and r_{Li} shows that the electrons are much more tightly bound to the magnetic field lines than the ions due to their mass. The difference in mass also results in much higher cyclotron frequencies for electrons than ions, i.e. 2.6×10^9 rad/s for electrons compared to 3.6×10^4 rad/s for argon ions for the conditions above.

Characteristic of magnetic nozzles are gradients in magnetic field strength and variations in field geometry. As charged particle are trapped to magnetic field lines through the Lorentz force, magnetic nozzles can be used to contain, guide, compress and expand plasmas. In this thesis, plasmas are typically flowing through magnetic nozzles between regions of strong and weak magnetic fields. When discussing plasmas in magnetic fields like these, it is important to introduce the concept of a magnetic mirror. Consider a magnetic field with cylindrical geometry which increases in strength in the $+z$ direction. A charged particle travelling in the $+z$ direction and orbiting a magnetic field line with a perpendicular velocity of $v_\perp$ will experience an average force, F_z, in the z direction given by equation 1.9 [2].

$$F_z = -\frac{1}{2}\frac{mv_\perp^2}{B}\frac{\partial B_z}{\partial z} \tag{1.9}$$

Equation 1.9 shows that for an increasing magnetic field strength, F_z is negative and will act against particle motion parallel to the field line. The $\frac{1}{2}\frac{mv_\perp^2}{B}$ term in equation 1.9 is known as the magnetic moment, μ, and is invariant under interactions with the magnetic mirror. As the particle moves closer to the region of high magnetic field strength, the value of $v_\perp$ must increase such that μ is kept constant. If B is high enough then the velocity parallel to the field line, $v_{||}$, will become zero given that the total kinetic energy must also be conserved. In this case, the particle is reflected back to the region of low magnetic field strength. Of course, as the B field decreases, equation 1.9 shows that the particle would accelerate away from the region of high magnetic field strength. Magnetic mirrors have been used previously to axially confine plasmas [12]. This confinement is not perfect however as some particles travelling towards the region of high magnetic field strength have small or negligible values of $v_\perp$, i.e. all of their velocity is parallel to the field lines. A loss cone can be defined which identifies the particles which will not be reflected by the magnetic mirror. For a particle travelling towards the magnetic mirror, the pitch angle, θ, at any point can be defined by $v_\perp^2/(v_\perp^2 + v_{||}^2) = \sin^2\theta$. If the particle originates from a region where the initial magnetic field strength is B_i and is travelling towards the maximum field strength B_{max}, the smallest pitch angle that will be reflected θ_{min} is given by equation 1.10 [2].

$$\sin^2(\theta_{min}) = \frac{B_i}{B_{max}} = \frac{1}{R_m} \tag{1.10}$$

where R_m is called the magnetic mirror ratio.

The magnetic mirror effect can quite frequently be disregarded when analysing the low pressure plasma systems in this thesis because electric fields parallel to the magnetic field lines generated by the plasma typically dominate the particle dynamics in system.

1.1.3 Radiofrequency plasmas

In this thesis, external power is provided to the plasma using a radiofrequency (RF) power source. RF plasmas are useful for low pressure plasma creation because they can achieve plasma breakdown at much lower voltages than DC discharges [13] and are convenient for propulsion applications because a dielectric can be used to separate the plasma from the antenna, meaning that the antenna is not eroded over long operation times [5, 7]. For frequencies greater than ~ 1 MHz, RF antennas provide energy to electrons in the plasma using oscillating electric and magnetic fields in the near field of the antenna. Ions are too massive to respond to the RF fields at these frequencies and only interact meaningfully with the time averaged electric fields generated in the plasma [3, 9]. The plasmas in this thesis are created

using RF at 13.56 MHz at powers of a few hundred Watts. Given that there is a source of strong oscillating electric fields near the plasma, the sheath potentials in the plasma discussed in the last section and shown in figure 1.1 also oscillate, i.e. $V_p = V_{DC} + V_{RF}\sin(\omega t)$ where V_{DC} is the DC component of the plasma potential, V_{RF} is the amplitude of the RF oscillation of the plasma potential, ω is the angular frequency of the RF and t is time in seconds. How the antenna fields couple to the plasma determines how efficiently power can be deposited into the system and therefore how much plasma is created. As such, some time is taken here to discuss the coupling modes in RF plasmas. Descriptions of the coupling modes discussed here are in no way complete, however these are the most relevant to the plasmas discussed in this thesis. With increasing RF power, discrete jumps between coupling modes are visible in measurements of the plasma density as higher power modes are typically more efficient [14].

Capacitively coupled plasmas

At low powers, RF plasmas are typically in the capacitively coupled mode. In capacitively coupled plasmas, the RF electric fields generated by the antenna cause large oscillations in the sheath potential and width [3]. Within capacitively coupled plasmas, plasmas can be created in some combination of two modes; alpha and gamma [9]. In the alpha mode, electrons undergo stochastic heating which means that energy is provided to the electrons as they are reflected between the high voltage sheaths [15, 16]. The energy gained from this collisionless interaction is then used to ionise neutrals. In gamma mode operation, ionisation is dominated by secondary electron emission from the wall as it is bombarded by high energy ions that fall through the high voltage sheath and liberate electrons [17, 18]. These electrons are accelerated by the full sheath potential and contribute significantly to ionisation of neutrals. Combinations of alpha and gamma modes operating at the same time are also possible. In practice, the capacitive mode is typically associated with a square root relationship between density and RF power, P_{RF}, i.e. $n \propto \sqrt{P_{RF}}$.

Inductively coupled plasmas

When the plasma density increases with increasing RF power coupled to the plasma, the RF skin depth decreases. The RF skin depth, δ_{RF}, is a measure of how far RF electric fields can propagate into a material. For an incident RF electric field, the amplitude of the oscillation will reduce by $1 - 1/e = 63\%$ within one skin depth, $1 - 1/e^2 = 86\%$ within two skin depths, etc. The skin depth can be calculated for a plasma using equation 1.11 [3].

$$\delta_{RF} = \frac{c}{\omega_{pe}} \approx \frac{c}{2\pi 9000\sqrt{n}} \tag{1.11}$$

where δ_{RF} has units of cm, c is the speed of light in cm/s, ω_{pe} is the plasma frequency, and n is the plasma density in cm^{-3}. As the RF power and plasma density increase, the RF skin depth shrinks and becomes comparable to the dimensions of the system, meaning that only those electrons within this layer near the antenna are efficiently heated. This enhances ohmic heating within a few skin depths of the antenna and screens the bulk plasma from RF fields, thereby reducing the amplitude of RF oscillations to the plasma potential in the centre of the plasma. In a cylindrical geometry, the current flowing through the RF antenna will induce opposing azimuthal currents in the plasma. As such, the power transfer from antenna to plasma has been modelled as a transformer coupled circuit model for inductive discharges [3, 9, 19]. This effect leads to a more efficient coupling with the plasma and is typically identified in experiments as a linear relationship between plasma density and RF power, i.e. $n \propto P_{RF}$.

Helicon plasmas

A helicon wave is a right-hand polarised electromagnetic wave travelling between the ion and electron cyclotron frequencies, i.e. $\omega_{ci} < \omega < \omega_{ce}$. While helicon waves had previously been studied in metals and treated mathematically [20, 21], Boswell was the first to use them to excite a low pressure gaseous discharge [22, 23] and later showed their ability to create a high density plasma relative to the input RF power [24]. The power transferred from the RF antenna to the helicon wave can be absorbed by the plasma through both collisional and collisionless mechanism with the former dominating behaviour at high pressure [25], i.e. when electron-neutral collisions are more frequent. The collisionless coupling mechanisms which dominate at low pressure have been the focus of debate and significant research [14, 22, 25–28] and detailed descriptions of this can be found elsewhere in the literature. As this thesis does not delve deeply into the world of helicon waves, it is sufficient to say that the power from the wave is transferred to the electrons in the plasma through interactions with the helicon wave fields. Previous experiments have demonstrated that when helicon wave coupling is present, the system can exhibit very high densities due to a power law relationship between plasma density and RF power [14], i.e. $n \propto P_{RF}^{a}$ where $a > 1$. The observation of a "blue core" in argon plasmas is typically associated with a helicon wave coupled mode as the blue ArII lines dominate the emission spectrum.

1.1.4 Electric double layers

Before launching into a literature review on the previous work done on plasmas interacting with magnetic nozzles, it is important to briefly describe the concept of an electric double layer

which can form in a plasma. Electric double layers (DLs) in plasmas are sheath-like structures where local quasineutrality is violated over distances greater than the Debye length (λ_D) and consist of a region of stationary positive charge situated adjacent to a region of stationary negative charge [29, 30]. This can be measured as a plasma potential drop greater than the electron temperature ($V_{DL} \geq T_e$, where V_{DL} is the magnitude of the potential drop in V and T_e has units of eV) occurring sharply over a few tens to hundreds of λ_D [29]. The "strength" of a DL is commonly denoted by the ratio of V_{DL}/T_e with higher values indicating a stronger DL.

The simplified spatial potential structure of a DL is depicted in figure 1.2 and can be interpreted as an ion sheath (on the left side in figure 1.2) adjacent to an electron sheath (on the right side in figure 1.2), meaning that ions are accelerated towards the DL from one direction while electrons are attracted from the other. Particles in a 1-D system containing a DL fit into one of four categories (trapped or free ions or electrons) depending on their energy and which side of the DL they are on, as shown in the figure [30, 31]. Higher order structures, such as triple (TLs) and quadruple layers have also been studied [30, 32] and can be thought of similarly but with more trapped and free particle conditions possible due to the more complex spatial structure.

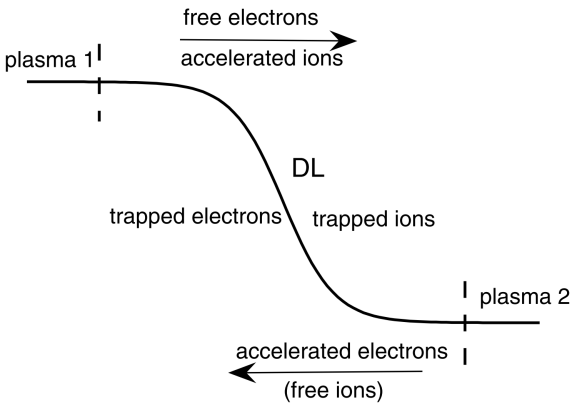

Figure 1.2: A generalised potential profile of a double layer, taken from [31]. The DL acts as an interface between two regions of different plasmas properties shown as plasma 1 and plasma 2. The location of trapped and free ion and electron populations are shown on either side of the DL.

DLs are typically found at the interface between two regions of plasma that exhibit different properties or abruptly change size (denoted as plasma 1 and plasma 2 in figure 1.2) [31, 33]. While they have been found in astrophysical plasmas [34, 35], this thesis focuses on laboratory plasmas. In laboratory plasmas, DLs have been measured in unmagnetised and magnetised

plasmas and have been found in front of cathodes, near geometric constrictions, in Q-machines and in triple plasma devices [33, 36–38]. In 1991, Hairapetian measured a DL in a plasma expanding away from a DC plasma source along a weak, uniform magnetic field [39]. The DL was only detected at very low pressures ($\leq 2 \times 10^{-5}$ Torr) and was determined to be current-free, i.e. no relative electron-ion drift. The authors noted that their experimental setup could easily be altered to test the same plasma behaviour in expanding or converging magnetic fields. However, it wasn't until 2003 that a current-free double layer was detected in a laboratory plasma expanding through a diverging magnetic nozzle [40].

1.1.5 Expanding plasmas in diverging magnetic nozzles

Measurement of ions accelerated to Mach numbers up to ~ 3 by a converging-diverging magnetic nozzle were presented decades ago in the seminal work of Andersen et al. [41], however laboratory plasmas expanding through magnetic nozzles have attracted increased interest from the electric propulsion community over the last two decades largely due to the discovery of a current-free double layer (CFDL) in an expanding plasma device at The Australian National University (ANU) in 2003 [40]. Charles et al. demonstrated that, for 0.2 mTorr argon gas and 250 W of RF power, a CFDL was created in the Chi Kung plasma reactor at the interface between the helicon plasma source and a larger diameter grounded expansion chamber. A Helmholtz pair of solenoids provided a near-constant magnetic field ($>$200 Gauss) in the source region which diverged in the expansion chamber, decreasing in strength to only a few tens of Gauss. The CFDL was detected as a sharp drop in both the axial density and axial potential profiles measured using *in-situ* diagnostic probes. The CFDL was characterised by a potential drop approximately 3 times the electron temperature and the authors proposed that this potential drop would accelerate ions from the plasma source into the expansion region, thereby generating a thrust that could be useful for space propulsion. For argon pressures above $1-2$ mTorr, the sharp potential drop was not detected. In the same year, Cohen et al. independently demonstrated ion acceleration in an expanding magnetic field with similar geometry to the Chi Kung reactor in the Magnetic-Nozzle-Experiment facility (MNX) using a laser induced fluorescence diagnostic [42].

Charles et al. extended their work by measuring the time development of the CFDL, showing that it is created during plasma breakdown and it is stationary and stable thereafter [43]. The existence of supersonic ion populations with energies of ~ 20 eV in hydrogen and argon, and later, xenon and molecular plasmas was also shown through the use of retarding field energy analysers (RFEAs) in the Chi Kung reactor under similar experimental conditions [44–47]. Ion beams with similar energies were also observed at West Virginia University

(WVU) by Sun et al. in the Hot hELIcon eXperiment (HELIX) as the argon plasma expanded along diverging magnetic field lines into the much larger grounded expansion chamber (LEIA) [48]. The study by Sun et al. investigated the dependence of the beam velocity on pressure and showed that it is inversely proportional to the argon gas pressure for a constant magnetic field. A collaboration between the WVU and ANU groups showed that the LIF technique could be extended to measure the axial beam energy profiles throughout the HELIX/LEIA and Chi Kung apparatuses and therefore indirectly measure the accelerating potential structure [49, 50] with an *ex-situ* technique. The observed potential structures were seen to be consistent with the results of 1-D, Monte Carlo particle-in-cell (MCC/PIC) simulations which demonstrated both the existence of the CFDL and supersonic ion population [51, 52]. In the PIC codes, the double layer formation was driven by an enforced loss process that represents the reduction in density along the axis of the expanding plasma in the diverging magnetic field.

As interest in this area of research grew, other researchers also demonstrated the existence of CFDLs and supersonic ion beams accelerating away from diverging magnetic nozzles where a low pressure RF plasma source is connected to a larger diameter expansion chamber [53–60]. Charles et al. showed that there was a magnetic field strength threshold over which an ion beam could be observed [61]. This was associated with a jump in the upstream plasma potential and density in the source region and was later explained as being due to ion magnetisation in the source region which acts as a trigger for ion beam creation [62]. Detachment of the ion beam from the magnetic field lines was studied by simulating the ion beam trajectory throughout the Chi Kung plasma reactor and the beam was considered to be detached when the curvature of that trajectory approached zero [63]. This occurred within a few centimetres downstream of the interface between the plasma source and the expansion region.

Aanesland et al. showed the presence of an upstream ionisation instability in the source region of Chi Kung and investigated its cause [64, 65]. The authors theorised that the instability was due to an energetic electron population accelerated into the plasma source from the expansion region by the CFDL. However, measurements of the axial upstream EEPF taken by Takahashi et al. in the same reactor were unable to demonstrate an electron beam in the source [66]. These EEPFs showed a two-temperature Maxwellian distribution with low energy, hot electrons and cooler electrons at higher energy. This is characteristic of a depleted tail, and the break energy, i.e. the energy above which the distribution is depleted, was consistent with the double layer potential, indicating that the higher energy electrons in the source region are able to overcome over the double layer. These electrons can traverse the entire experiment and are not heated as effectively by the RF antenna because their residence

time in the source region is reduced relative to those that cannot overcome the CFDL.

Takahashi et al. continued to study the electron dynamics in the source region of Chi Kung for experimental conditions that produced an axial CFDL and radial measurements of the EEPF revealed that the electron temperature was minimum on axis ($T_e \sim 8$ eV) and increased towards the walls ($T_e \sim 16$ eV) [67]. The break energies in the EEPFs taken radially in the plasma source were also seen to increase towards the wall and possibly indicated how off-axis potential structures were influencing the electron transport. On-axis, downstream of the CFDL, the EEPF demonstrated a single Maxwellian distribution of electrons with a temperature of 5 eV [68]. Off-axis, however, the EEPFs showed a two temperature Maxwellian, this time with a hot tail above some break energy. The EEPFs with a hot tail were measured at positions corresponding to the location of the most radial magnetic field lines to escape the plasma source region. The electrons have very small Larmor radii and are tightly bound to the magnetic fields and due to their large mean free path for collisions of all types, they stream along the magnetic field lines without collisions. Therefore the hot electrons that were detected off-axis in the source region are transported to the downstream and detected as the hot tail in the EEPF. This non-local treatment of the electron transport was confirmed by measuring the EEPFs on axis throughout the chamber and the results showed that the sum of kinetic and potential energy was conserved for electrons travelling along the field line [69].

By mapping the density downstream of the double layer, Charles later showed that the hot, high energy electrons detected off-axis ionise locally in the expansion chamber, creating regions of high density plasma along the most radial field lines to escape the source region [70]. These high density regions follow the expanding magnetic field lines, forming a conical shell of locally ionised plasma and are hence named "conics". This means that the downstream region of these expanding plasma devices can be described by an axial supersonic ion beam surrounded radially by the stationary high density conics structure. The conics structure was determined by Saha et al. to be unrelated to the presence of the CFDL as electrons will be transported along the field lines regardless of the axial potential structure [71]. Takahashi et al. showed that the topography of the electron temperature throughout the system was entirely controlled by the position of the RF antenna relative to the magnetic field [72] and that the existence of hot electrons in the downstream region could be suppressed by ensuring that the electrons heated most effectively by the antenna could not flow along field lines that escape the source region. Since their first discovery, high density conics located at the radial boundary of the ion beam have been measured in multiple devices, also reported as a hollow radial density structure downstream of the source chamber [73–75], however their importance to the axial beam characteristics are yet to be explored.

1.1.6 Plasmas incident on converging magnetic nozzles

In a study assessing the performance of a helicon thruster, Takahashi et al. showed that the magnetic field configuration that results in the largest thrust was actually that which used a converging-diverging magnetic nozzle [76]. This magnetic field geometry was investigated in the Chi Kung reactor by Zhang et al. and the results showed that the axial density and potential profiles strongly followed that of the axial magnetic field strength for sufficiently high solenoid current, i.e. the density and potential were maximum under the solenoid, not the centre of the antenna [77, 78]. Similarly, a study by Samuell et al. conducted in the MAGnetised Plasma Interaction Experiment (MAGPIE) when the solenoidal magnetic field was somewhat distant from the RF antenna (∼40 cm separation) showed that the density profile is a maximum under the solenoids, increasing with increasing magnetic field strength [79]. This increase in density appears to be proportional to the magnetic field strength and allows for the creation of a very high density plasma under the solenoids. The authors explain that the mechanism behind this density increase is due to contraction of the plasma as it flows along the converging magnetic field lines. This is useful for fusion related research as high density plasma sources can be used to investigate fusion relevant turbulence effects [80, 81] and instabilities [82], test plasma-facing materials [83, 84], and are being investigated for uncaesiated negative ion production for neutral beam injection systems [85]. As such, the converging magnetic field geometry provides a good testbed for high density plasma research. However, while the density profiles have been seen to closely align with the throat of the converging-diverging magnetic nozzle even when the solenoid is not located near the antenna, the nature of the coupling between the plasma source and the remote magnetic field is unclear.

Previous studies investigating the power deposition and RF coupling mechanisms in the vicinity of a converging magnetic field have demonstrated different behaviour to those in a constant magnetic field. Instead of the distinct jumps in density found by Degeling et al. as the RF power was increased and the coupling mode changed [14], Mori et al. showed that the density transitioned smoothly with increasing RF power when the magnetic field geometry was converging [86]. Chen also briefly investigated the operation of a helicon device when the magnetic field was cusping in the antenna region and showed that the plasma density was maximum for this configuration [87]. A number of other authors addressed helicon wave propagation in converging magnetic field geometries, e.g. [88–91], however the results reported by Zhang et al. and Samuell et al. are produced using low RF power and the plasma is therefore unlikely to be operating in a helicon mode. It is interesting then to investigate the nature and limits of the coupling between an RF plasma source and a remote solenoidal magnetic field as this is yet to be fully understood.

1.2 Scope of thesis

This thesis focuses on the experimental investigation of low pressure plasmas interacting with magnetic nozzles. The experiments are conducted in two different experimental systems; the Chi Kung plasma reactor (chapters 3 to 6), which has been used extensively in the previous work to study plasmas in diverging magnetic nozzles, and the Echidna plasma reactor (chapter 7), which is a new, purpose-built device which can be used to study plasmas in converging magnetic nozzles. These reactors, their subsystems and a variety of electrostatic diagnostic probes are described in chapter 2.

In chapter 3, the standard operating characteristics of the Chi Kung reactor are established and the properties of a supersonic ion beam accelerated by a double layer-like potential structure are shown. The pressure dependence of the ion beam velocity and density are assessed and the results are compared to a previous study which used an *ex-situ*, non-perturbative laser technique.

In chapter 4, the behaviour of the plasma in the Chi Kung reactor is measured when the location of the geometric expansion is moved downstream with a pyrex extension tube. When the extension tube is inserted, the geometric expansion and diverging magnetic nozzles are no longer colocated. Measurements of the ion energy distribution function and the axial ion transport characteristics are presented for cases when the extension tube is and is not present. Radial measurements of the plasma properties throughout the system are presented and allow for conclusions about the electron transport to be made.

In chapter 5, a variable gap between the extension tube used in chapter 4 and the source tube is introduced. This allows for selective radial release of certain electron populations streaming along magnetic field lines that can pass through the gap.

In chapter 6, measurements of the plasma density and potential taken along the most radial magnetic field line to escape the source region of Chi Kung are presented. The results allow for conclusions to be made about the field-aligned electron transport from the antenna region to the high density conics downstream.

In chapter 7, measurements of the axial density profiles in Echidna are presented for cases when the solenoidal magnetic field and the RF antenna are progressively separated. Investigation of the electron transport and the modes of operation are also investigated.

Chapter 2

Experimental apparatus

2.1 Overview

The experiments presented in this thesis are conducted across two different experimental setups. Chapters 3-6 are the subject of results garnered using the Chi Kung plasma reactor while chapter 7 refers to a study completed in a new, purpose built plasma reactor, "Echidna". The Chi Kung reactor is an expanding plasma device in which a current-free double layer (CFDL) was first demonstrated in an expanding magnetic field [40]. In the Chi Kung reactor, plasma is created in the region of high magnetic field and flows through a diverging magnetic nozzle to regions of lower magnetic field strength. This setup provides a good analog for thruster applications, where exhaust plasma expands away from the spacecraft until it detaches from the magnetic field lines, and some astrophysical processes, like the origin of the solar wind in the solar corona, where the source plasma is created in the throat of a magnetic nozzle. In other processes, like those in the polar regions of Earth, the source plasma is incident on the magnetic nozzle from the weak regions of the magnetic field. The Echidna plasma reactor, named for its long "snout", was built to test the behaviour of plasmas incident on a converging magnetic field with increasing field strength and features a movable set of solenoids that produce the magnetic field which can be progressively separated from the radiofrequency (RF) antenna. Each of these plasma reactors requires vacuum and gas subsystems in order to provide low pressure environments suitable for plasma creation and manipulation using RF power and solenoid subsystems. The Chi Kung reactor and its subsystems are described in section 2.2 while Echidna and its subsystems are described in section 2.3. A variety of diagnostic probes are used in each device to measure plasma parameters of interest and these are described in section 2.4.

2.2 Chi Kung

As shown in figure 2.1a, the Chi Kung plasma reactor consists of a RF plasma source contiguously attached to a larger diffusion chamber, herein referred to as the expansion chamber. The point on axis at the intersection between the plasma source and expansion chamber is set as the origin of the cylindrical coordinate system used throughout this thesis. The plasma source itself consists of a 31 cm long, 13.7 cm inner diameter, 15 cm outer diameter Pyrex tube. A grounded aluminium end plate fit with an axial KF-25 port seals the end of the plasma source using a Viton o-ring compressed around the outer face of the Pyrex source tube. A 5 mm thick annular Pyrex plate with an inner radius of 1 cm is inserted between the pyrex source tube and the aluminium end plate, to allow gas injection through the KF-25 port at $z = -33$ cm while ensuring that almost all of the source region is insulated from electrical ground. Connected to the other end of the plasma source is the 30 cm long, 32 cm inner diameter grounded aluminium expansion chamber which seals the Pyrex tube in a similar manner to the aluminium end plate at $z = -33$ cm. The expansion chamber has a number of ports available for pumping, gas injection, pressure gauges and diagnostic probes, as has been described at length previously [92]. The end plate of the expansion chamber is removable, allowing for internal access to Chi Kung, and is fitted with a "VacuumSlide". The VacuumSlide features a KF-25 port mounted on an aluminium bar which has been ground flat, allowing it to slide over an elongated slot without breaking the vacuum held by an o-ring concentric with the slot. This can be fit with the diagnostic probes discussed in section 2.4 and allows for both radial and axial movement of the probes.

In chapters 4 and 5, the layout of Chi Kung reactor is altered slightly with the inclusion of a Pyrex glass tube inserted into the expansion chamber. The Pyrex tube is referred to as the "extension tube" and has the same inner diameter as the source tube of Chi Kung, a wall thickness of 0.7 cm and is 18.5 cm long. The extension tube sits on top of an aluminium support structure such that it is concentric with the source tube. The aluminium support can be manually moved in the z-direction using a 0.25" stainless steel rod which is sealed using the same type of vacuum feedthrough as that used for the probe shaft. A diagram of Chi Kung featuring the extension tube is given in chapter 4 where its positioning and purpose is discussed.

An Alcatel ACT600 controller is used to operate an Adixen ATP400 turbmolecular pump which is connected upstream of a MVP60 rotary pump. The pumps connect to the side wall of the expansion chamber at $z = 25$ cm and can maintain a base pressure below 2×10^{-6} Torr. The pressure in the system is monitored using an array of pressure gauges. In the range $\sim 10^{-2}$

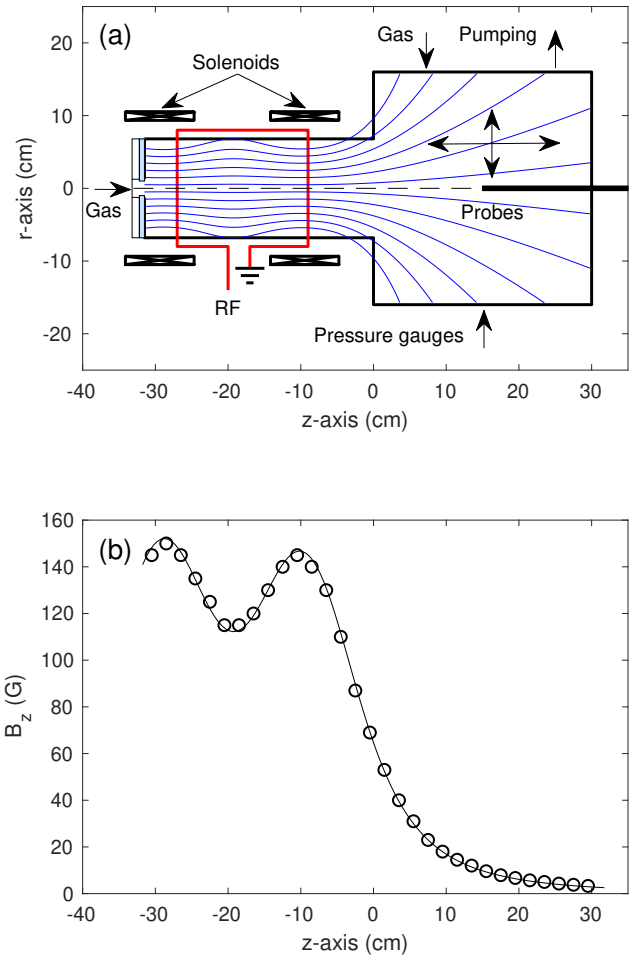

Figure 2.1: (a) 2-D schematic of the Chi Kung reactor showing the locations of the RF antenna, solenoids, gas inputs, pressure gauges, pumping and diagnostic probes. The magnetic field lines (blue solid lines) are calculated using the BScalc program. (b) Measured (circles) and simulated (solid line) axial magnetic field strength.

to 10^2 Torr, a Granville Phillips 275 Convectron Vacuum Gauge (Convectron, herein) is used with a Granville Phillips 307 Vacuum Gauge Controller to roughly measure the background pressure while venting and pumping the chamber. To measure the base pressure of the system (10^{-7} to 10^{-6} Torr), a MDC 432025 Ion Gauge Tube (ion gauge, herein) is used with the same controller as the Convectron. A type 220CA MKS Baratron Absolute Pressure Transducer (Baratron) is used to measure the pressure in the range which experiments are conducted (10^{-4} to 10^{-3} Torr). Argon gas can be introduced into the system either through the KF-25 port on axis at $z = -33$ cm or through a KF-25 port on the radial wall of the expansion chamber at $z = 7$ cm. The injection of argon gas is monitored by a type 2169B MKS Mass Flow

Controller (20 SCCM range) which is controlled using a type 247 MKS 4 Channel Readout. In this thesis, the quoted value of argon gas pressure for each experiment is measured prior to igniting the plasma and, by connecting the Baratron gauge to different vacuum ports over the chamber, it was observed that the pressure was uniform throughout the system. Even when the plasma is ignited, the RF power and ionisation rate are quite low, meaning that there is no neutral depletion. Further, given that the pressure is very low and the gas is in the free molecular flow regime, transfer of thermal energy to the background neutral gas is minimal and the pressure is not significantly affected by the plasma.

Much of the interesting plasma behaviour in Chi Kung is a result of the expanding magnetic field's diverging geometry. This magnetic field is produced by two solenoids in a Helmholtz pair configuration mounted concentrically with the source tube. Each solenoid consists of 12 layers of approximately 67 turns of polyamideimide enameled copper wire and is wired in a doubly wound configuration. This means that two halves of a single solenoid are electrically in parallel. Therefore, the current in the solenoids is actually half of that provided by the Aim-TTi CPX400A DC PSU used to power them. For the rest of this thesis, any reference to the current in the Chi Kung solenoids will refer to the current supplied by the power supply before being halved due to the doubly wound configuration. The magnetic field generated by the solenoids can be calculated using the BScalc program used previously [92], which discretises a solenoid into a number of straight line segments and solves the Biot-Savart equation for each segment. The total field is then calculated by summing the fields generated by each straight line segment. Figure 2.1b shows the axial magnetic field strength in Chi Kung for a solenoid current of 6 A found through measurements with a Bell 640 incremental Gaussmeter (circles) and simulation using the BScalc program (solid line). The measured and calculated field strengths are in excellent agreement and show that the axial magnetic field has a peak axial value of 145 Gauss in the source region before rapidly decreasing to a few tens of a Gauss in the expansion chamber. The overall shape of the magnetic field lines can also be plotted using the results of BScalc and the solid blue lines in figure 2.1a show that a near parallel field is created in the source region before diverging near $z = 0$ cm.

Centred on $z = -18$ cm and surrounding the source tube is a 18 cm long double-saddle RF antenna used to excite the plasma. The antenna is fed with RF power from an ENI OEM-25 (0-3 kW) generator at a constant frequency of 13.56 MHz via an L-matching network. The L-matching network is required to match the 50 Ω output impedance of the RF power supply to the variable and complex impedance of the combined antenna/plasma system. A diagram of the full RF circuit used in the Chi Kung experiment is shown in figure 2.2. The L-match consists of two variable vacuum capacitors, C_{load} and C_{tune}, with ranges from 20-2000 pF

and 20-500 pF, respectively and the output of C_{tune} is directly connected to the antenna. RF diagnostic probes are also present in the circuit and these consist of a model 4391 Bird RF Power Analyst (Bird meter, herein) and a Revex W502 SWR & Power meter (SWR meter, herein). Here, for convenience, the Bird meter is used to measure the forward RF power while the SWR meter monitors the standing wave ratio (SWR). By adjusting the values of C_{load} and C_{tune}, the SWR can be decreased to ~ 1, i.e. maximum power transmission, meaning that the equivalent impedance of the area contained within dotted square in figure 2.2 is equal to the output impedance of the generator, 50 Ω.

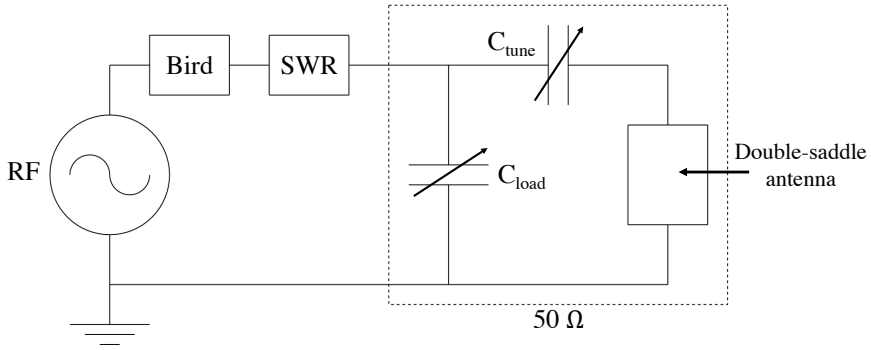

Figure 2.2: Diagram of the RF matching circuit used on the Chi Kung reactor. Shown on the diagram are the RF power supply, the Bird and SWR meters, C_{load} and C_{tune} capacitors, and the double-saddle antenna. When the impedance is appropriately matched, the components inside the dotted square have an equivalent impedance of 50 Ω and the measured SWR is ∼1.

National Instruments (NI) Labview data acquisition (DAQ) software is used to control the diagnostic probes used in Chi Kung. Measurements using the uncompensated Langmuir probe, the emissive probe and the retarding field energy analyser (all described in section 2.4) are acquired using a NI PCIe 6251 Multifunction I/O device in conjunction with a BNC-2110 Shielded Connector Block. Measurements using the RF compensated Langmuir probe are acquired using a NI PXI-5122 card installed in a NI PXI-1031 chassis.

2.3 Echidna

The Echidna plasma reactor is depicted schematically in figure 2.3 and features a 1.5 m long, 9 cm inner diameter, 10 cm outer diameter borosilicate glass tube. The centre of a double-saddle antenna is used as the origin of the coordinate system used in Echidna, as depicted in 2.3, i.e. $(r, z) = (0, 0)$ cm at the centre of the RF antenna.

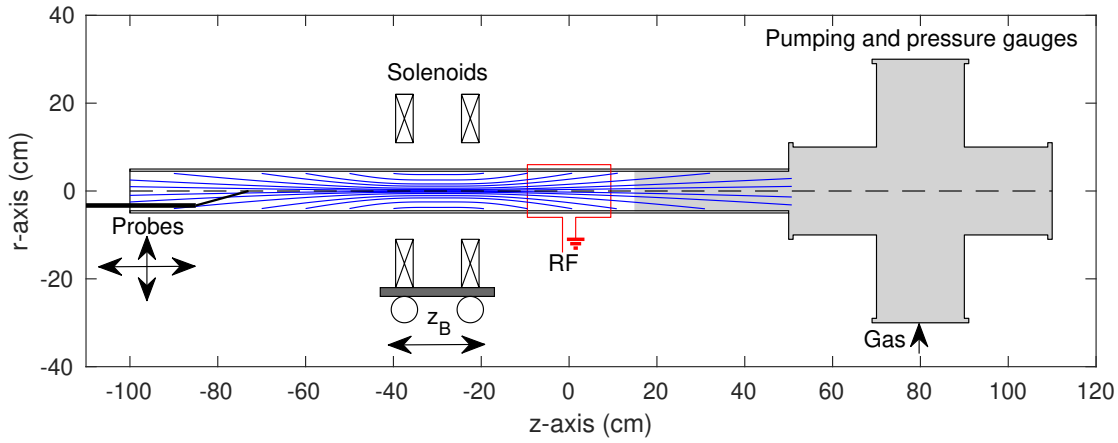

Figure 2.3: 2-D schematic of the Echidna reactor showing the locations of the RF antenna, movable solenoids (shown at $z_B = -30$ cm), gas input, pressure gauges, pumping and diagnostic probes. The magnetic field lines (blue solid lines) are calculated using the BScalc program. Areas shaded in grey represent regions in the experiment where the radial walls are grounded.

Sealing to the external face of the glass tube at $z = -100$ cm is a custom made, electrically grounded aluminium annulus which can either seal to a MDC 24 cm outer diameter claw clamp flange or a Vacuumslide used previously in [93]. The Vacuumslide is very similar in construction and operation to the one used in the Chi Kung reactor. The opposite end of the glass tube at $z = 50$ cm is contiguously attached to a MDC grounded 6-way cross vacuum chamber which is also sealed with MDC 24 cm outer diameter claw clamp flanges. Some of the flanges have been fit with a variety of ports to allow for pumping, pressure gauges, gas injection and diagnostic probes. In this thesis, however, results are only obtained using probes inserted through the Vacuumslide at the $z = -100$ cm end.

The pumping system on Echidna uses a Leybold Turbotronik NT 20 to control a Leybold TURBOVAC 600 C turbomolecular pump connected in series with a VRD-30 Dual Stage rotary pump and can achieve a base pressure below 10^{-6} Torr. The pressure gauges on Echidna consist of a type 274 Granville Phillips Ionization Vacuum Gauge, a type 627B MKS Baratron Absolute Pressure Transducer (0.05 Torr range) and a type 275 Granville Phillips Convectron gauge. The ion gauge and Convectron are both powered through a type 307 Granville Phillips vacuum gauge controller while the Baratron is controlled using an MKS PR4000B digital power supply and readout. Gas is introduced through a port at $z \sim 80$ cm and is regulated by a type 1179A MKS Mass Flow Controller (100 SCCM range) which is

controlled using a type 247 MKS 4 Channel Readout. To ensure that no pressure gradient is present along Echidna's central axis, a second Baratron gauge was placed at $z = -100$ cm and measurements of pressure at each end were taken for argon flow rates from 5 SCCM to 100 SCCM. The measurements of pressure are plotted in figure 2.4. The figure shows that the pressure measurements at each end of the glass tube are very similar, indicating that no strong pressure gradient develops over the length of the experiment.

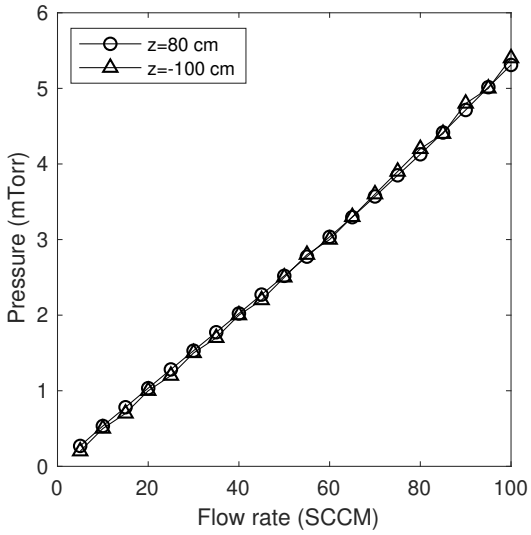

Figure 2.4: Pressure inside Echidna as a function of argon mass flow rate measured at $z = -100$ cm (triangles) and $z = 80$ cm (circles).

The magnetic field in Echidna is generated using a pair of solenoids arranged concentrically with the glass tube, as depicted in figure 2.3. To vary the distance between the solenoidal magnetic field and the RF antenna, the solenoid pair is fixed to an aluminium platform mounted on wheels which roll on a set of aluminium rail tracks parallel with the glass tube. The location of the centre point between the solenoids is referred to as z_B and the position of the solenoids in figure 2.3 is $z_B = -30$ cm. The solenoids are separated by a centre to centre distance of 15 cm and consist of 129 windings of 4 cm wide, 0.5 mm thick copper strap wound from an inner radius of 11 cm. Co-wound with the copper strap is a layer of 0.2 mm thick, 4 cm wide Elephantide flexible insulator to stop adjacent layers of copper strap from short circuiting. The choice to use copper strap was made to increase the packing factor of windings, however this means that much larger currents must be used than in other experiments (e.g. the Chi Kung solenoids) because the number of turns along the z-axis is reduced to one. In essence, the solenoids are made up of 129 single cooper loops stacked on top of each other. The magnetic field produced by the solenoids can be calculated using BScalc,

however as the software computes the field based on an infinitely thin wire wound into a helix, the solenoids are modelled as 129 layers of 10 wire windings, each 4 mm wide. The current in each simulation was reduced by a factor of 10 to account for multiplying the number of turns by 10. The axial magnetic field strength simulated by BScalc for equivalent real solenoid currents of 20, 40 and 80 A are plotted in figure 2.5 for $z_B = -30$ cm. Also plotted in the figure are measurements taken for the 20 A case which are seen to strongly agree with the simulations. The figure shows that the solenoids generate an essentially constant magnetic field on axis over a range of 20 cm centred on z_B. Most of the experiments in chapter 7 are conducted using the 40 A case which shows a peak field of approximately 300 Gauss.

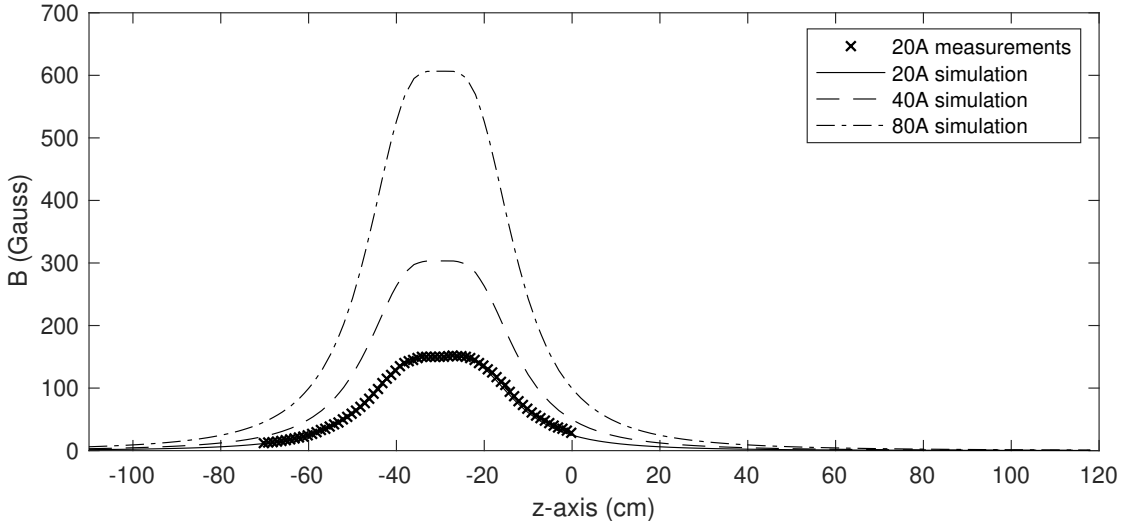

Figure 2.5: Simulated axial magnetic field strength in Echidna created by the solenoid pair positioned at $z_B = -30$ cm for solenoid currents of 20 (solid line), 40 (dashed line) and 80 A (dash-dotted line). Measurements of the axial field strength are also shown (crosses) for a solenoid current of 20 A.

The RF antenna installed on Echidna is a 19 cm long double-saddle antenna and is fed with RF power at 13.56 MHz from an ENI OEM-25 (0-3 kW) through an L-matching network, similar to the Chi Kung reactor. Figure 2.6 is a diagram of the RF circuit used to provide power to the antenna. There are three major differences between the RF circuits on Echidna and Chi Kung. The first is the addition of an Octiv meter installed post-match (between the matching elements and the antenna). The Octiv probe was installed here to measure the RF voltages and currents, as well as the complex impedance of the coupled antenna/plasma system. The second difference is the additional parallel capacitance to ground (C_{coax}) between C_{tune} and the Octiv meter. This is a result of a short length of coaxial cable ($\sim$ 15 cm) is

inserted post match, connecting the output of the matching elements to the antenna. The third difference is the inclusion of a buffer capacitor (C_{buffer}) in parallel with C_{load}. The value of C_{buffer} is a constant 4310 pF, made by combining two 1900 pF and one 510 pF capacitors in parallel. This was included because the range of the C_{load} variable vacuum capacitor (100-2000 pF) was not sufficient to achieve the required $\sim$ 5000 pF, calculated using a Smith chart program, SimSmith. By including the buffer capacitor, the overall range of the C_{buffer} and C_{load} capacitors is 4410-6310 pF. C_{tune} has a range of 50-500 pF. The Bird meter used in this circuit is the same as the one used on Chi Kung and is in series with a CN-801 SWR & power meter.

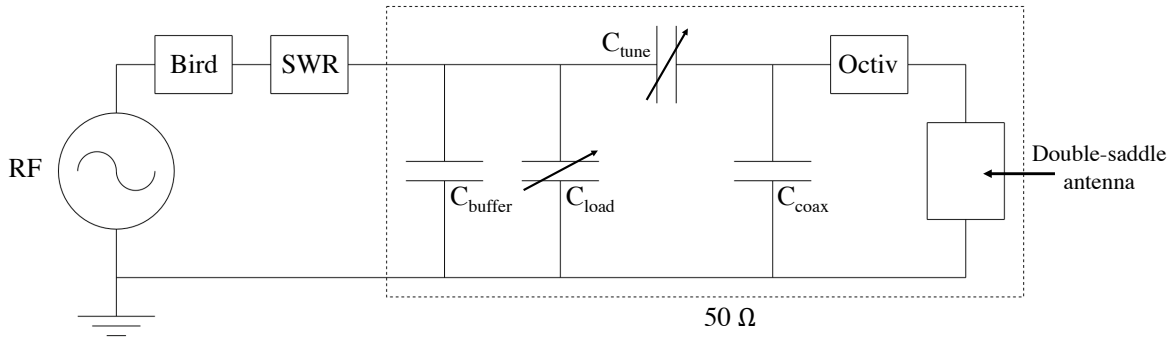

Figure 2.6: Diagram of the RF matching circuit used on Echidna. Shown on the diagram are the RF power supply, the Bird and SWR meters, C_{buffer}, C_{load}, C_{tune} and C_{coax} capacitors, Octiv meter and the double-saddle antenna. When the impedance is appropriately matched, the components inside the dotted square have an equivalent impedance of 50 Ω and the SWR has a value of 1.

MATLAB's Data Acquisition and Instrument Control toolboxes are used to control the diagnostic probes used in Echidna. Measurements using all diagnostic probes are acquired using a NI PCIe 6351 Multifunction I/O device in conjunction with a BNC-2110 Shielded Connector Block.

2.4 Diagnostic probes

A variety of diagnostic probes have been used to measure the fundamental properties of low-pressure plasmas since the 1920's [94]. These diagnostic probes broadly fall into two categories; *in-situ* electrostatic probes that are in physical contact with the plasma, and *ex-situ* techniques which measure some emitted signal from the plasma (e.g. spectroscopy, LIF).

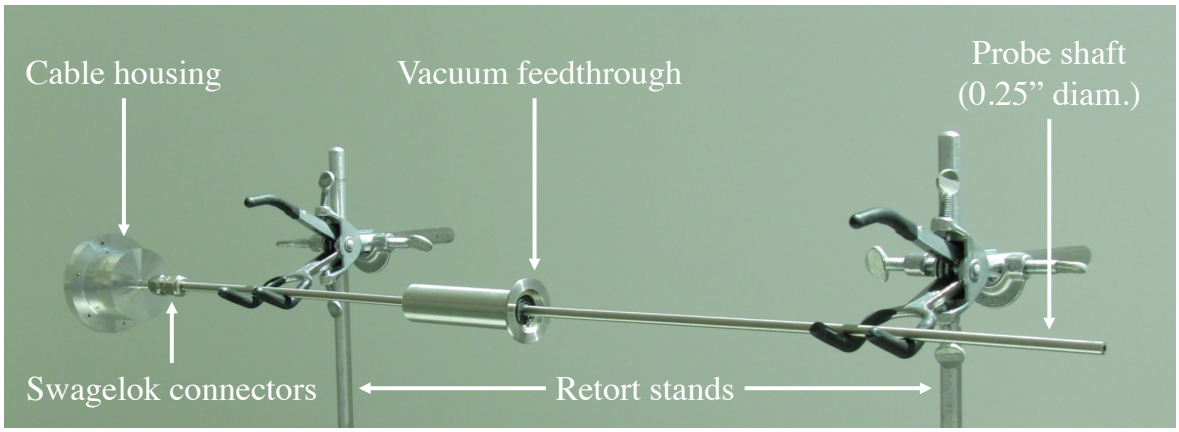

Figure 2.7: Photo of a probe shaft assembly with no probe installed.

While *in-situ* electrostatic probes directly measure various properties of a plasma, they can perturb the overall plasma behaviour due to their size or electrical conductivity, leading to erroneous measurements. *Ex-situ* techniques have their own disadvantages, relying on various assumptions about plasma behaviour and chemistry which can lead to limitations in their use, as well as problems associated with line of sight. As such, careful use of any diagnostic technique along with thorough understanding of their operation and limitations is necessary in order to have confidence in their measurements.

The diagnostic techniques used in this thesis belong to the category of *in-situ* electrostatic probes and the following subsections describe the four types of probes used. These are the Langmuir probe, the RF-compensated Langmuir probe, the emissive probe and the retarding field energy analyser. Of extreme value to the experimentalist is the ability to move a probe and spatially characterise a plasma without breaking vacuum. To do this, all diagnostic probes discussed here can be mounted onto a 0.25” outer diameter aluminium probe shaft which can slide through a “knife-edge” lip seal, holding vacuum while the probe is moved. The lip seal sits inside a custom adaptor which can be connected to a vacuum chamber via a KF-25 port on the chamber walls or Vacuumslide. Stainless steel 316 Swagelok ferrule and nut fittings connect the probe shaft to another custom made aluminium housing that allows for electrical vacuum feedthroughs (not shown in the figure) from data acquisition and control circuits to the probe. Figure 2.7 shows an annotated photo of a probe shaft assembly with no probe installed.

2.4.1 Langmuir probe

The first diagnostic probe used in this thesis is the Langmuir probe (LP). In its simplest form, a LP is nothing but a conducting wire inserted into the electrically conductive plasma. The

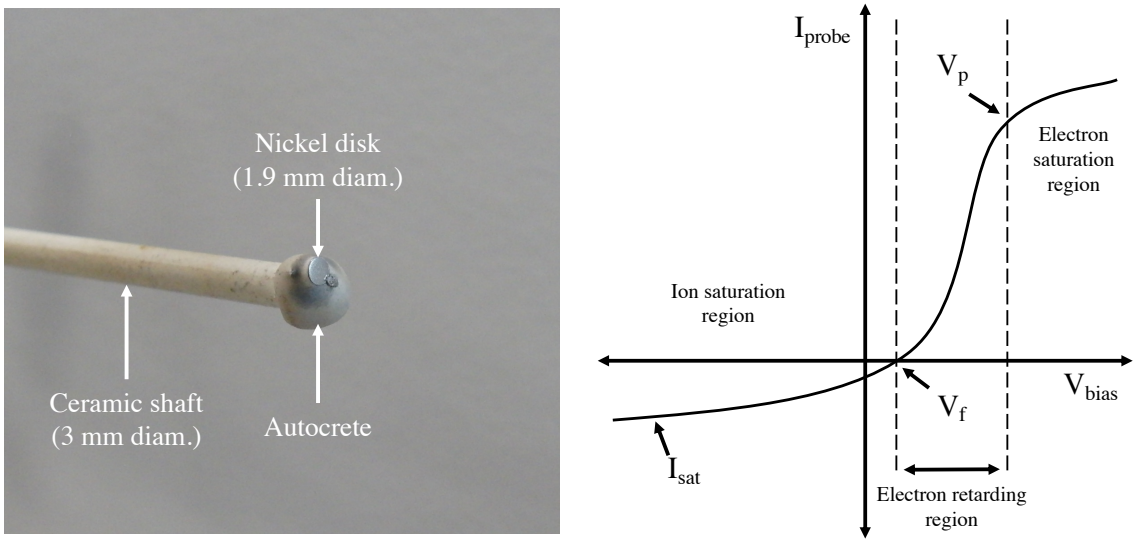

Figure 2.8: (a) Photo of the planar LP tip. (b) Idealised current-voltage (I-V) sweep of a Langmuir probe immersed in a low-pressure plasma illustrating the ion saturation, electron retarding and electron saturation regions.

area of wire exposed to the plasma is typically referred to as the 'probe tip'. The geometry of the probe tip is very important and the operation of a number of probe tip geometries have been studied [94–96]. In this thesis, all LPs other than the RF-compensated Langmuir probes discussed in section 2.4.2 use planar probe tips as pictured in figure 2.8a. The tip is made from a single-sided 1.9 mm diameter nickel disk and is positioned at the end of a 3 mm diameter ceramic tube. The disk is crimped to a teflon coated wire before being attached to the ceramic tube using a ceramic paste called "Autocrete". Dark markings on the Autocrete shown in figure 2.8a are a result of exposure to plasma. The probe assembly shown in figure 2.8a is mounted on a probe shaft like that shown in figure 2.7, allowing for electrical connection of the probe to an external circuit. The rest of the discussion in this section will focus on the operation of planar LPs like those shown here.

Many important physical parameters of a plasma, such as the ion density, electron temperature and plasma potential, can be deduced from measurements of the electric current flowing between the plasma and the probe tip (I_{probe}) as a function of an externally applied bias voltage (V_{bias}). The behaviour of I_{probe} can be broadly categorised into three regions dependent on the value of V_{bias} relative to the floating potential, V_f, and the plasma potential, V_p: The ion saturation region for $V_{bias} < V_f$, the electron retarding region for $V_f < V_{bias} < V_p$, and the electron saturation region for $V_p < V_{bias}$. To illustrate this, an idealised current-voltage (I-V) sweep of a Langmuir probe immersed in a low-pressure plasma is shown in figure 2.8b.

For $V_{bias} < V_f$, electrons are strongly repelled while ions are accelerated towards the probe tip, meaning that I_{probe} can almost purely be attributed to ions. In an ideal probe, the ion current would saturate to a constant value below V_f, hence this region is known as the ion saturation region. This constant value of I_{probe} is called the ion saturation current (I_{sat}) and, in the ideal case, can be used to infer the local ion density of an argon plasma using equation 2.1 [9, 97].

$$I_{sat} \simeq 0.6 q A_p c_s n_i \tag{2.1}$$

where the constant coefficient of 0.6 is an approximate representation of the ratio between the ion density at the sheath-presheath edge and in the bulk plasma, q is the elementary charge, A_p is the area of the probe tip, c_s is the local ion sound speed and n_i is the local ion density. Physically, equation 2.1 essentially shows that the current entering the probe is due to the flux of ions impacting on the probe tip. In practice, however, the ion saturation region does not saturate to a single I_{sat} for $V_{bias} < V_f$. In fact, the magnitude of I_{sat} tends to grow indefinitely with increasingly negative values of V_{bias}. This behaviour is due to the sheath expansion effect which increases the effective collection area of the increasingly high voltage sheath surrounding the probe tip in plasmas where the Debye length becomes comparable to the radius of the probe tip [96].

In cases where the sheath expansion effect is significant, Sheridan's method can be used to calculate the ion density from a value of I_{sat} taken at a V_{bias} sufficiently below V_f [98]. Using Sheridan's method, the n_i is related to I_{sat} by equation 2.2.

$$I_{sat} \simeq 0.55 q A_s c_s n_i \tag{2.2}$$

where the constant coefficient of 0.55 is used to account for the curvature of the sheath in front of the probe and A_s is the area of the sheath. A_s is related to A_p by equation 2.3.

$$\frac{A_s}{A_p} = 1 + a\eta_p^b \tag{2.3}$$

where $\eta = (V_p - V_{bias})/T_e$ is a dimensionless form of the probe bias voltage. The coefficients a and b were derived in [98] and are dependent on a dimensionless form of the probe tip radius ($\rho_p = r_p/\lambda_D$) as in equation 2.4.

$$a = 2.28\rho_p^{-0.749} \qquad b = 0.806\rho_p^{-0.0692} \tag{2.4}$$

Measurements taken in the Chi Kung reactor have previously shown that the ion density calculated by rearranging equation 2.1 can significantly overestimate the plasma density, whereas Sheridan's analysis is required [99].

In an ideal semi-infinite planar probe when V_{bias} is increased to positive values, I_{probe} should saturate to a constant electron saturation current (I_e) at $V_p < V_{bias}$ in a similar way

to the ion saturation region described above. In a real probe with finite size, the electron saturation region (labelled in 2.8b) does not settle to a constant value due to the finite size of the probe. In a planar probe, the current continues to increase with increasing V_{bias} due to contributions from the sheath at the edges of the probe [96]. As such, the planar probe begins to act like a spherical probe which does not saturate in the electron saturation region.

For $V_f < V_{bias} < V_p$, electrons are able to reach the probe but are retarded by the sheath in front of the probe. For non-drifting Maxwellian electrons incident on an ideal planar probe, I_{probe} in this electron retarding region can be described by equation 2.5.

$$I_{probe}(V_{bias}) = I_e \exp\left[\frac{-q(V_p - V_{bias})}{T_e}\right] \tag{2.5}$$

Conveniently, equation 2.5 shows that I_{probe} would be linear on a semilog plot with a slope directly proportional to T_e. In the ideal case, I_{probe} in the electron retarding region and its derivatives with respect to V_{bias} are also proportional to the electron energy distribution function (EEDF), $F(\epsilon)$, where ϵ is the electron energy in eV. For a real probe with finite size, this is not the case for I_{probe} or dI_{probe}/dV_{bias}, but Druyvesteyn showed that this proportionality still holds for d^2I_{probe}/dV_{bias}^2 [100, 101] when the electron population is isotropic (e.g. unmagnetised) and the probe tip is convex. The Druyvesteyn theory [102] shows that the electron energy probability function (EEPF), $f(\epsilon) = \epsilon^{-1/2}F(\epsilon)$, can be calculated from the second derivative of the probe current using equation 2.6.

$$f(\epsilon) = \frac{2(2m_e)^{1/2}}{q^3 A_p}\frac{d^2 I_{probe}}{dV_{bias}^2} \tag{2.6}$$

where m_e is the mass of an electron. Both the electron density, n_e, and an effective electron temperature, T_{eff}, can be calculated using the EEDF using equations 2.7-2.8.

$$n_e = \int_0^\infty F(\epsilon)d\epsilon = \int_0^\infty \epsilon^{1/2} f(\epsilon)d\epsilon \tag{2.7}$$

$$T_{eff} = \frac{2}{3n_e}\int_0^\infty \epsilon F(\epsilon)d\epsilon = \frac{2}{3n_e}\int_0^\infty \epsilon^{3/2} f(\epsilon)d\epsilon \tag{2.8}$$

In an RF plasma like those discussed in this thesis, however, the electron retarding and saturation regions can be subject to large aberrations due to RF modulation of the sheath surrounding the probe tip. As such, the uncompensated LPs are only used to measure the ion saturation current and floating potential in this work. To measure the electron retarding and saturation regions, the RF-compensated Langmuir probes discussed in section 2.4.2 are used.

When a LP is used in a magnetised plasma, the results are known to be perturbed based on the degree of magnetisation [96]. For the plasmas discussed in this thesis, the ion Larmor

radius is always at least 10 times the LP tip radius, whereas the electron Larmor radius is typically on the order of 0.1-1 mm. In this regime, measurements of the ion saturation region are not significantly affected by the magnetic field's presence, however the electron regions of the I-V sweep can be distorted due to depletion of electrons along magnetic field lines that intersect the probe tip. Given that the uncompensated LP is not used to measure this region of the I-V sweep due to the RF perturbations discussed above, the effects and considerations of the magnetic field are discussed in relation to the RF-compensated Langmuir probe in section 2.4.2.

Figure 2.9 illustrates the electrical circuit used to operate the uncompensated LPs. The setup consists of a Hewlett Packard 6827A Bipolar Power Supply used to generate V_{bias}. V_{bias} is typically swept from -100 to 30 V in order to capture the entire ion saturation region. I_{probe} is measured across the resistor R which has a selectable resistance of 1, 10, 100, 1k or 10k Ω. The signal passes through an isolation amplifier in order to protect the DAQ equipment from the high voltages generated by the bipolar power supply. The voltage measured by the DAQ board is therefore RI_{probe}.

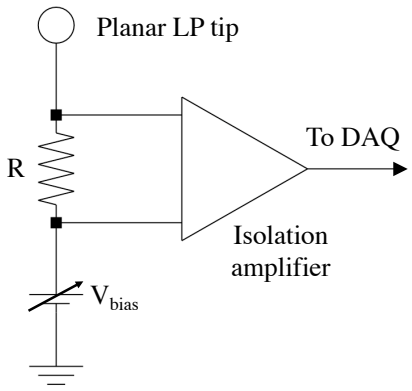

Figure 2.9: Diagram of the electrical circuit used for LP operation.

2.4.2 RF-compensated Langmuir probe

To avoid RF distortions to the electron retarding and saturation regions in the LP sweep, an RF-compensated Langmuir probe (CP) can be used. In order to compensate for the RF modulation of the DC sheath in front of the probe tip, the CP uses a set of passive RF choke coils, specifically tuned to the RF frequency 13.56 MHz and its first harmonic at 27.12 MHz. A photo of a typical CP used in this thesis is shown in figure 2.10a and follows a previously published design [103]. The CP consists of a 5 mm long, 0.5 mm diameter cylindrical tungsten probe tip protruding from a glass pipette sealed with Autocrete. A 4.7 nF capacitor isolates

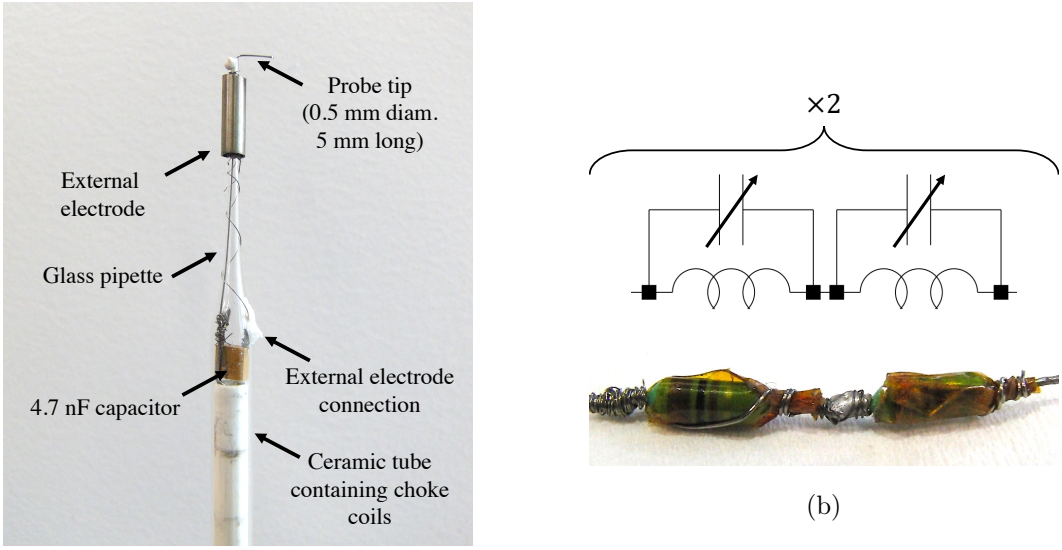

(a) (b)

Figure 2.10: (a) Photo of the CP probe tip. (b) Photo and equivalent electrical circuit diagram of the RF chokes used to suppress RF aberrations in the I-V trace.

the probe tip from an external electrode which tracks oscillations in the local floating potential. The probe tip is directly connected to a chain of four RF choke coils, like those shown in figure 2.10b, which are housed inside a ceramic tube connecting the glass pipette to the probe shaft. Each of the electrical components in the CP are connected using a tungsten wire wrapping technique [93] and a small amount of solder.

The passive RF choke coils exploit the self resonance effect of inductors which causes them to act as band-stop filters centred on their self resonant frequency. The chokes are tuned using parallel variable capacitances which are implemented using nickel wire. The wire is electrically connected to one leg of the inductor while the other is wrapped around a thin layer of insulating tape surrounding the other leg. The number of windings and the separation between the nickel wire and the inductor leg controls the parallel capacitance, allowing for convenient tuning of the choke coils [104]. The nickel wire can be seen in figure 2.10b extending from the left hand side of the inductors to the right hand side where they are wound around a layer of Kapton tape.

The cylindrical probe tip is bent by 90° to the longitudinal axis of the CP such that it is always perpendicular to the magnetic field lines when used in both Chi Kung and Echidna. When a CP is immersed in a magnetised plasma in this orientation, attention must be paid to the size of the electron Larmor radius, r_{Le}, relative to the probe radius, r_p [105, 106]. In the limit that $r_p << r_{Le}$, the second derivative method for finding the EEPF in equation 2.6 can be used. When $r_{Le} << r_p$, the EEPF is found using the first derivative of the I-V trace

and is calculated with equation 2.9.

$$f(\epsilon) = \frac{3m_e^2 \ln(\pi l/4r_p)}{16\pi^2 q^3 V_{bias} r_{Le}} \frac{dI_{probe}}{dV_{bias}}. \tag{2.9}$$

where l is the probe tip length.

In many experiments presented in this thesis $r_{Le} \sim r_p$, which is known as the transition regime from unmagnetised to magnetised electrons. Demidov et al. gave analytical solutions for the probe characteristics in this regime [107] but admitted that solving the generalised equations can be difficult. In this regime, it is expected that the calculated values of n_e and T_{eff} would probably lie somewhere between those calculated using equations 2.6 and 2.9. A comparison between these two regimes is conducted with data obtained in Chi Kung later in section 4.4.

Numerical differentiation of a single I-V trace can amplify noise from the original measurement, making it difficult to accurately calculate the first and second derivatives. In order to avoid this source of additional noise, either one or two analog differentiators are used and allow for direct measurement of the first and second derivatives of I_{probe} with respect to time [66, 108]. Many averages of these differentiated signals are normally required for confidence in the results and repeated measurements are taken by ramping V_{bias} with a stable 20 Hz sawtooth pattern using a signal generator directly connected to the bipolar power supply. An example data set of V_{bias}, I_{probe} and its first and second derivatives with respect to time is plotted in figure 2.11a-d, respectively. To change the derivatives from being with respect to time to being with respect to voltage, the following transformation can be used:

$$\frac{dI_{probe}}{dV_{bias}} = \frac{dI_{probe}}{dt} \frac{dt}{dV_{bias}}$$

Figure 2.11a shows V_{bias} when ramped using the 20 Hz sawtooth signal. The slope of V_{bias} is $dV_{bias}/dt = 2000$ V/s, meaning that $dt/dV_{bias} = 5 \times 10^{-4}$ s/V. Therefore, the derivatives of I_{probe} must be multiplied by 5×10^{-4} each time that the signal is differentiated. Once these derivatives have been found, calculation of the EEPF and EEDF can be done by using the appropriate method described above for either unmagnetised or magnetised plasmas.

Figure 2.12 shows a typical EEPF measured by the CP using the second derivative method. The EEPF is seen to decrease linearly with increasing electron energy on the semilog plot which indicates that the electron population is a single Maxwellian. The gradient of the linear decrease is equal to $-1/T_e$ and the electron temperature is calculated to be 5 eV. This EEPF shows a strong signal to noise ratio for approximately 5 orders of magnitude, allowing for confidence in the CP operation and the T_e measurement.

The electrical circuit used to operate the CP is shown in figure 2.13. The circuit is very

similar to that which is used for the LP and the electrical components contained within the dotted square are housed inside the glass pipette in vacuum. Two RF chokes are used in series for each of the 13.56 and 27.12 MHz frequencies in order to increase the attenuation of the self resonant band-stop filter which is typically -80 dB. The probe current is measured across a resistor R and the isolation amplifier used in the CP circuit has a variable gain, G. Therefore, the voltage measured by the DAQ must be divided by RG to convert to current. The analog differentiators use the same circuit as that shown previously (e.g. in [93]).

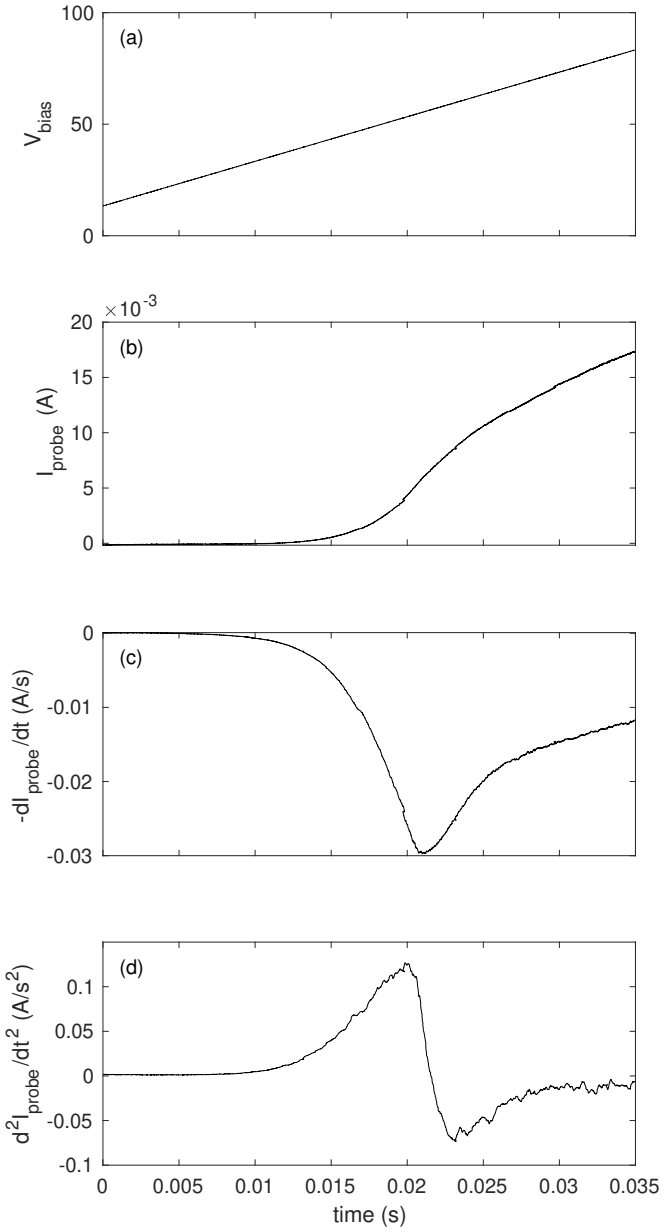

Figure 2.11: An example data set of a typical CP measurement. 100 averages were used to collect the data for (a) V_{bias}, (b) I_{probe}, (c) $-dI_{probe}/dt$ and (d) d^2I_{probe}/dt^2 with respect to time. The first derivative of I_{probe} is measured as negative because the differentiator circuit is operated in an inverting configuration.

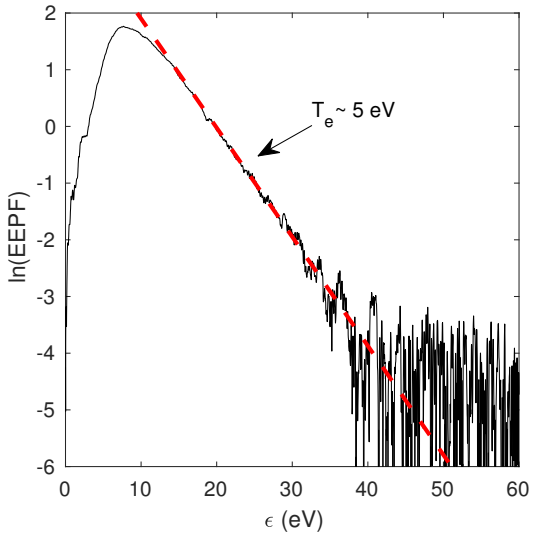

Figure 2.12: Typical EEPF measurement collected using the CP. The EEPF exhibits a Maxwellian electron distribution as it linearly decreases with electron energy on this semilog plot. The observed electron temperature is calculated from the slope of a linear fit to the distribution (red dashed line) and is found to be 5 eV.

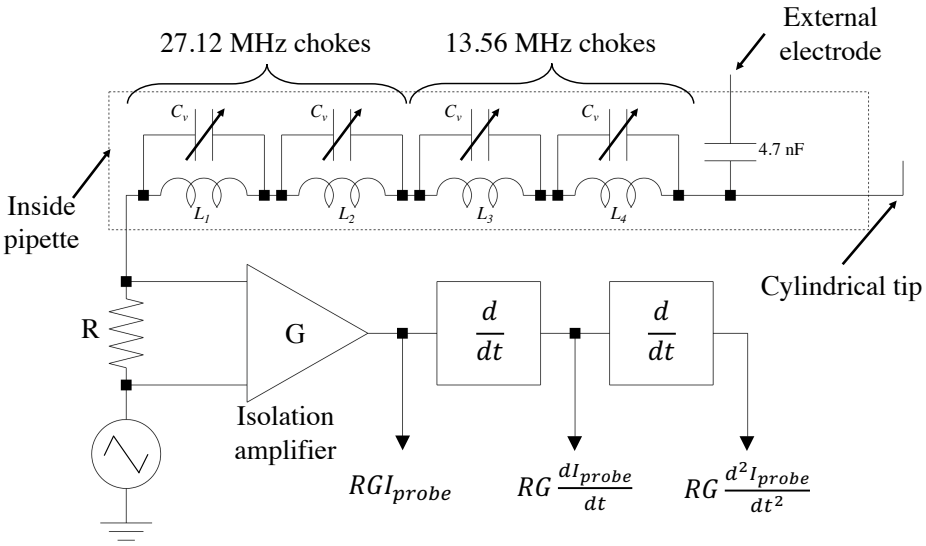

Figure 2.13: Diagram of the electrical circuit used for CP operation, showing the cylindrical probe tip, external electrode, tunable RF choke coils, V_{bias} ramping source and analog differentiators.

2.4.3 Emissive probe

The tip of an emissive probe (EP) is shown in figure 2.14a. The probe tip consists of a thoriated tungsten filament made from a 1 mm diameter coil and press-fit over copper wires that protrude from two separate bores through a 4.5 mm diameter ceramic tube. A layer of Autocrete coats the area where the copper wires exit the tube, ensuring that interactions with the plasma are localised to the tungsten filament. The filament is provided with a heating current, I_{heat}, as shown in the electrical circuit diagram in 2.14b. The two 120 Ω resistors allow for measurement of the floating potential of the probe tip without impacting the heating current.

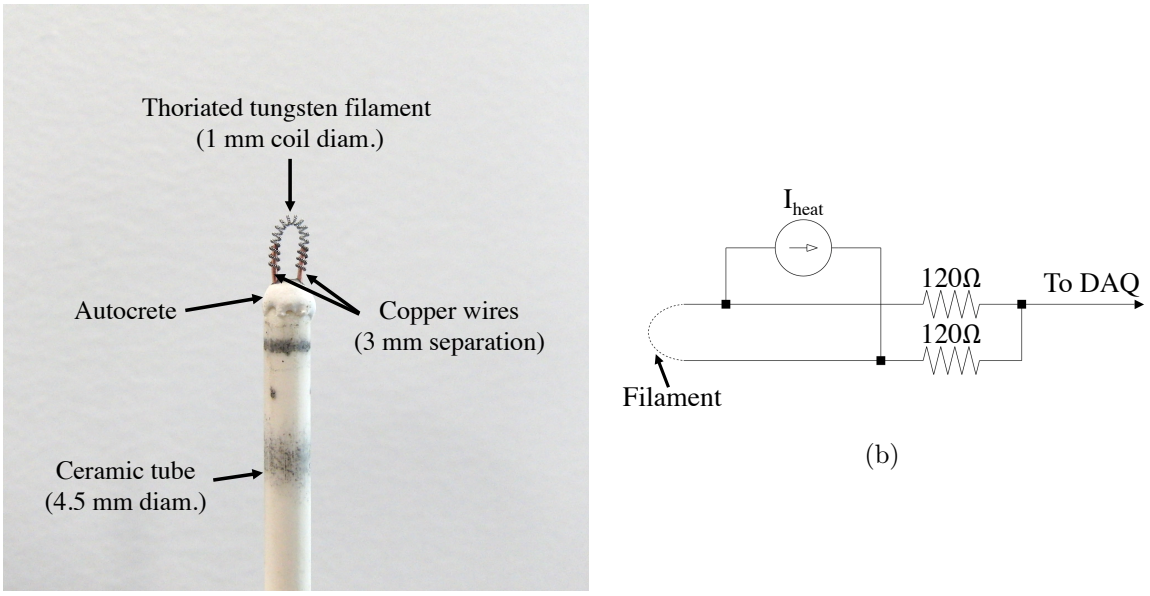

(a) (b)

Figure 2.14: (a) Photo of the EP tip. (b) A diagram of the electrical circuit used for EP operation.

The EP allows for direct measurement of the plasma potential through thermionic emission of electrons from the probe tip [96]. When $I_{heat} = 0$ A, the probe tip will float to the local floating potential. At greater heating currents, thermionic emissions occurs and the probe provides an electron current to the surrounding plasma. At a sufficiently high heating current, the electron current to the plasma becomes high enough to eliminate the sheath in front of the probe, allowing the local floating potential to equal the local plasma potential. This method of measuring the plasma potential is known as the floating potential method [28]. Fruchtman et al. discussed situations in which this method could underestimate the true plasma potential [109], however there was consistently good agreement between the different probes used to

measure the plasma potential in this work so the effects discussed by Fruchtman appear to be insignificant for the plasmas discussed in this thesis.

Figure 2.15 shows a typical measurement of V_f for increasing I_{heat} collected using the EP. The measured V_f when thermionic emission is insignificant is ~ 10 V, which is the local floating potential. As the heating current increases, the measured floating potential is seen to increase linearly before reaching a "knee" at a particular V_f, which is the local plasma potential. For heating currents higher than this, the floating potential continues to increase linearly but with a smaller slope. A good estimate of the knee location is given by the intersection between two lines fit to the two linear segments either side of it. Fits to these segments are shown in figure 2.15 as dashed red lines and intersect at $V_f = V_p = 43$ V, indicated by the dotted horizontal line. This method of determining the plasma potential is used for all EP measurements in this thesis.

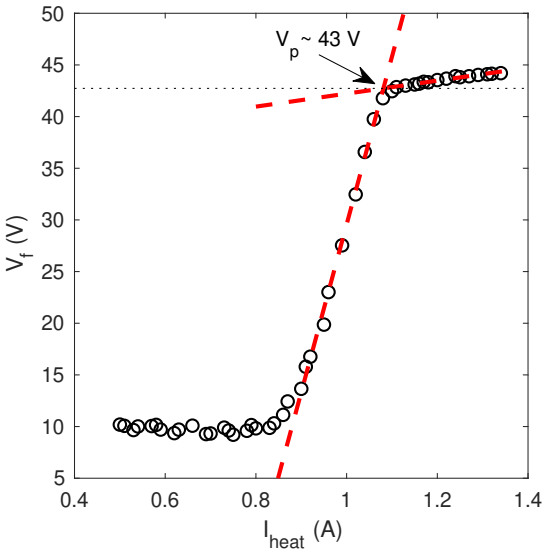

Figure 2.15: Typical measurement of V_f (circles) as a function of the heating current, I_{heat}. The red dashed lines are linear fits to the region just above and below the "knee" and intersect at $V_f = V_p = 43$ V, indicated by the dotted line.

2.4.4 Retarding field energy analyser

Retarding field energy analysers (RFEAs) are very useful for diagnosing low pressure plasmas as they can measure the full ion energy distribution function (IEDF) of ions falling through the grounded sheath in front of the probe orifice in the ion collection mode and the EEDF of electrons with energy greater than the plasma potential in the electron collection mode since

the RFEA is grounded [28, 110]. To do this, the RFEA uses a stack of biased grids to act as a directional energy filter on the flux of charged particles incident on a collector plate. Each grid is made from 500 lines-per-inch nickel mesh which are spot welded to a copper ring with a tab for soldering. The stack of grids is housed inside a grounded stainless steel case, pictured in figure 2.16. The case has dimensions of $3.5 \times 2 \times 1$ cm and is welded to a 0.25" stainless steel tube which is fit with Swagelok connectors. The front face of the RFEA housing features an aperture, behind which the stack of biased grids is positioned in front of a nickel collector plate. The RFEA's operation will only be discussed in relation to the ion collection mode as the electron collection mode is not used in this thesis.

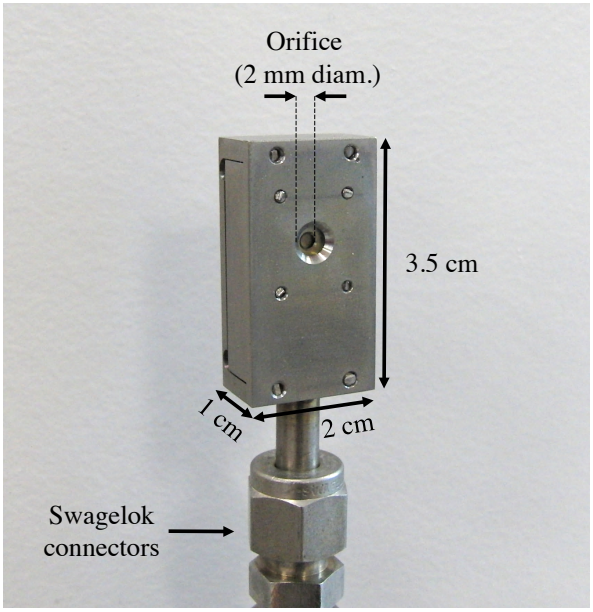

Figure 2.16: Photo of the RFEA housing with dimensions.

A full exploded view of the RFEA has been taken from [92] and is pictured in figure 2.17 while figure 2.18a shows a diagram of the electrical circuit used to operate the RFEA, providing the grid voltages as per figure 2.18b. Behind the front face of the RFEA is a stainless steel plate with a 2 mm orifice which is electrically connected to the grounded housing. The orifice is also connected to the earth grid, which is held at electrical ground in order to provide a spatially uniform sheath in front of the analyser, repelling electrons and accelerating ions into the probe. Sheets of 0.1 mm thickness mica insulator are sandwiched between each grid and feature a 4 mm diameter central hole such that ions can pass through the grids while they are kept electrically isolated. The second grid from the orifice plate is the repeller. The repeller is held at a constant negative voltage, V_R, such that electrons that are able to overcome the grounded sheath are repelled. For theses studies, the repeller voltage is held

at $V_R = -90\ V$ with a DC power supply. This means that all electrons in the plasma with kinetic energy less than $V_p + 90$ V are repelled. In Chi Kung, typical plasma potentials range from approximately 30-60 V. Therefore, only the very few electrons with energy > 120 eV can enter the probe under these conditions. A discriminator grid sits behind the repeller and is used to filter in energy positive ions that are accelerated by the grounded sheath surrounding the probe. When the discriminator voltage $V_D = 0\ V$, ions are not decelerated and all pass through the discriminator grid. As V_D is increased to some arbitrarily large positive voltage, ions begin to be repelled, until $V_D \approx V_p$ when the size of potential barrier of the discriminator grid is equal to the accelerating potential of the grounded sheath and only about half of the ion population can pass the discriminator. For larger discriminator voltages, the potential barrier provided by V_D is too large and no ions can pass the grid. Given the typical values of V_p in Chi Kung, V_D only needs to be swept from 0 V to ~70 V to measure the whole $I_C(V_D)$ characteristic. This is done using an output voltage sweep from the DAQ board into a fixed gain bipolar power supply. The dashed line in figure 2.18b shows the case in which V_D is a maximum and the $V_D = 0$ V case is illustrated by the solid black line. Those ions that pass the discriminator grid then encounter a suppressor grid held at a constant negative voltage, V_S, of -16.7 V before reaching the collector plate which is biased at $V_C = -7.7$ V. Secondary electron emission might occur when ions strike the collector plate and the suppressor grid acts to contain these secondary electrons to the collection area, suppressing spurious increases in the measured ion current due to liberation of electrons.

Measurements of the ion current incident on the collector plate (I_C) are a function of the ion velocity, V_D as given by equation 2.10 [111].

$$I_C(V_D) = \frac{T^4 A_o q}{M_{Ar}} \int_{qV_D}^{\infty} f_i(\epsilon_i) d\epsilon_i \tag{2.10}$$

where T is the transmission factor of the grids, A_o is the cross-sectional area of the orifice, M_{Ar} is the mass of an argon atom/ion, $f_i(\epsilon_i)$ is the IEDF of ions that have fallen through the grounded sheath as a function of ion energy ϵ_i. Differentiating equation 2.10 yields equation 2.11.

$$\frac{dI_C}{dV_D} = -\frac{T^4 A_o q^2}{M_{Ar}} f_i(qV_D) \tag{2.11}$$

Equation 2.11 shows that the IEDF is proportional to dI_C/dV_D, which can be easily calculated from the measured probe currents.

The ion current measured by the RFEA is said to be directional because ions can only enter the probe from one side of its housing (within an acceptance solid angle of $\sim 40^\circ$). Therefore, the measurement of the IEDF is particularly useful in experimental setups like Chi Kung as it can reveal the existence of an ion beam [45]. To demonstrate this, figure 2.19 shows normalised

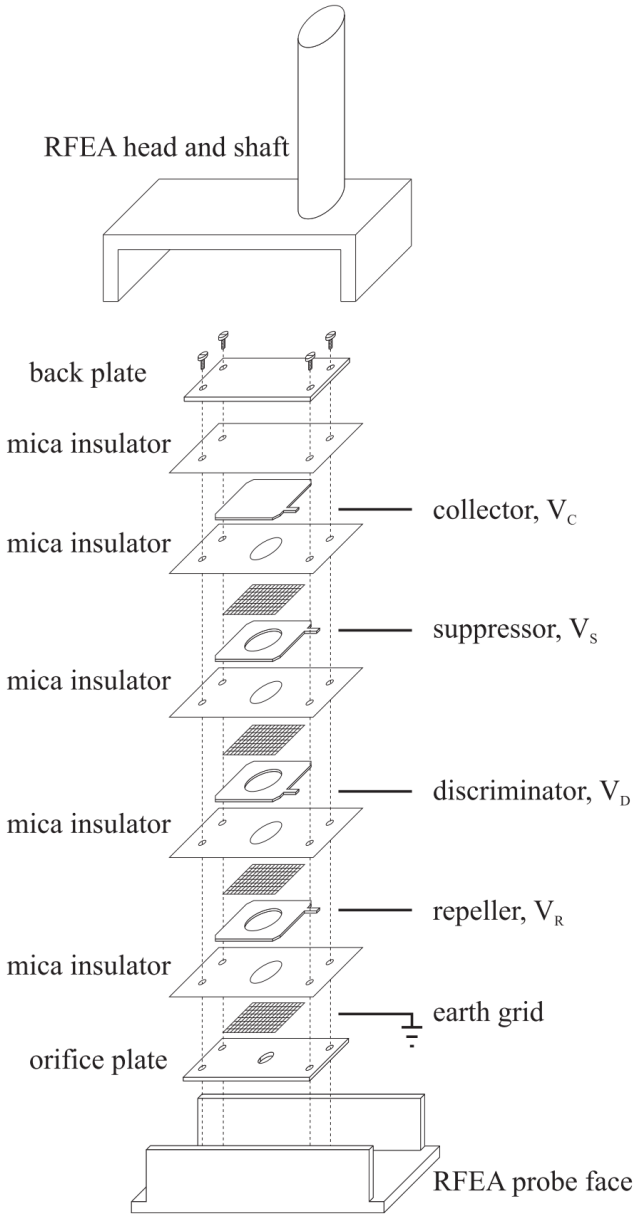

Figure 2.17: Exploded view of the RFEA (taken from [92]) showing the front and back sections of the housing, the orifice plate, mica insulators, nickel grids and copper rings.

plots of the measured $I_C(V_D)$ at the same location in Chi Kung for two different orientations of the RFEA. For the data shown in figure 2.19a, the RFEA was facing the radial wall of the chamber and was therefore perpendicular to any ion beam flowing on axis, meaning that it could not enter the orifice. In this case, the $I_C(V_D)$ data demonstrates a constant value until a sharp decrease centred around $V_D \sim 38$ V. To calculate the derivative of $I_C(V_D)$, a Savitzky-Golay filter [112] is applied to the data before it is numerically differentiated and another Savitzky-Golay filter is applied to the numerical derivative. To check the appropriateness of the filtering, the calculated derivatives can be integrated to recover the original $I_C(V_D)$ curve.

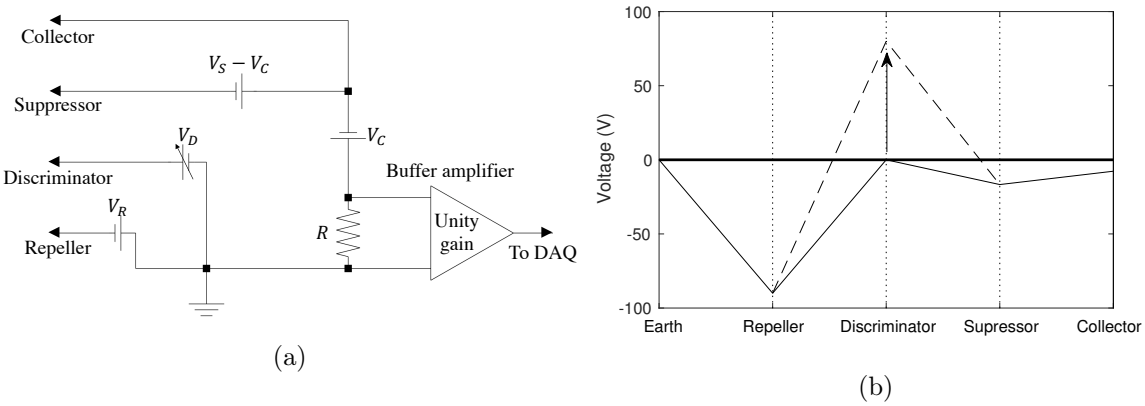

(a) (b)

Figure 2.18: (a) Diagram of the electrical circuit used for RFEA operation in ion collection mode. V_R, V_C and V_S are supplied using constant DC power supplies while V_D is swept by feeding the analog output of the DAQ board into a bipolar power supply. (b) Plot of the grid voltages for RFEA operation in ion collection mode. The solid black line indicates the grid voltages when the discriminator grid is grounded and the dashed line shows the grid voltages when V_D is maximum.

In figure 2.19a, the negative of the derivative demonstrates a single peak centred around the same discriminator voltage of the sharp decrease in the raw I_C data, corresponding to a local plasma potential of 38 V.

When the probe is oriented to face the source region of Chi Kung, a slightly different $I_C(V_D)$ curve is observed in 2.19b. In this figure, the collector current is seen to decrease in two separate steps, which becomes much more clear once differentiated. The derivative here shows the peak at the local plasma potential (38 V), as well as another peak at higher potential which is labelled as the beam potential, $V_b = 54$ V. Given that the peak at V_b was not visible in the radial-facing RFEA data, a directional ion beam flowing away from the source region is identified. The difference between the beam potential and the plasma potential reflects the magnitude of some potential structure upstream which accelerated the ion beam. As such, the beam energy in eV can be calculated as $E_b = V_b - V_p$, and the velocity of the ion beam, v_b, is calculated using equation 2.12.

$$v_b = \sqrt{\frac{2qE_b}{M_{Ar}}} \tag{2.12}$$

For the data presented in figure 2.19b, E_b is found to be 16 eV which yields a beam velocity of $v_b = 8.8$ km/s. In cases where E_b is small and the local and beam peaks overlap, V_p and V_b can still be found by fitting two Gaussian distributions to the dI_C/dV_D data.

Authors rarely publish the absolute density as measured by an RFEA due to difficulties

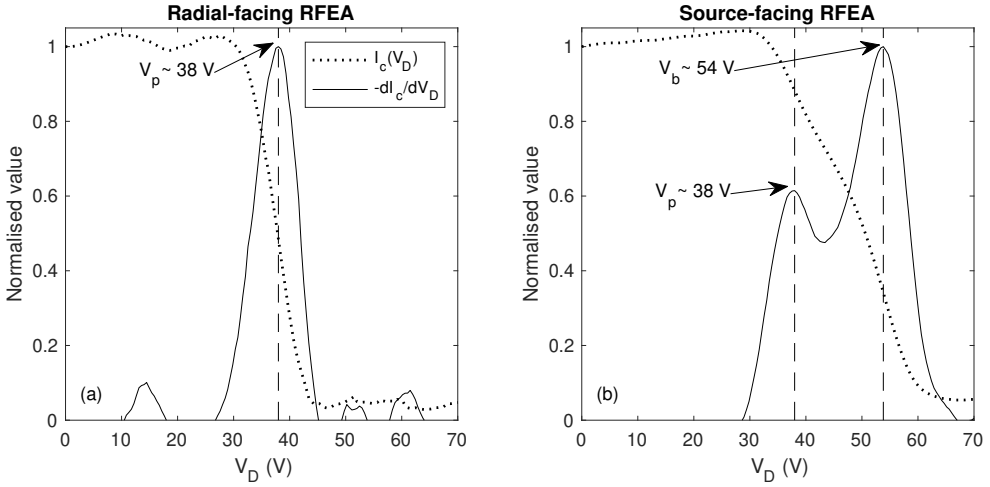

Figure 2.19: Normalised measurements of $I_C(V_D)$ (dotted lines) and dI_C/dV_D (solid lines) measured by the RFEA when it is oriented (a) perpendicular to an ion beam and (b) facing the ion beam. The local ion population demonstrates a peak at $V_D = V_p = 38\ V$ in both (a) and (b), whereas the ion beam population is only detected in (b) with a V_b of 54 V.

associated with the grid transparency and alignment, RF broadening of the measured IEDF, and potential perturbations of the plasma potential around the large grounded probe [113]. Further, the current measured at the collector is particularly sensitive to the ion flow velocity entering the probe as it is a current measurement in energy space. Given that the ion flow speed of the local population into the the RFEA is dependent on the plasma potential, it is not trivial to calibrate these probes for density measurement in experiments like Chi Kung because V_p varies throughout the chamber. Similarly, the high velocity of an ion beam will artificially increase the measured current of a beam population relative to the local population. For these reasons, the ion current associated with the local and beam populations are more commonly reported [114, 115]. With careful treatment of the RFEA data, however, the absolute density of the local and beam populations can be recovered once calibrated with a LP. This has been done previously using two different methods. The first uses Gaussian fits to dI_C/dV_D to determine the ion current associated with local and beam populations before considering the flux of these populations as they enter the RFEA [45]. The second fits the integral of drifting Maxwellian distributions to the raw $I_C(V_D)$ data, allowing for direct extraction of the local and beam densities [116, 117].

Gaussian-flux method

The dI_C/dV_D data for a single ion population, like that shown in figure 2.19a, can be fitted with a simple Gaussian of the form

$$g(V_D) = ae^{-(\frac{V_D - V_p}{d})^2} \tag{2.13}$$

where a and d are fitting parameters. The total ion current, $I(0)$, measured by the RFEA is equivalent to the integral of $f(V_D)$:

$$I(0) = \int_{-\infty}^{\infty} g(V_D)dV_D = ad\sqrt{\pi} \tag{2.14}$$

The measured ion current is a function of both ion density and velocity and can therefore be related to the flux of particles entering the sheath of the RFEA by noting that a stationary plasma at some position z_{stn} will enter the sheath at the local ion sound speed, $c_{s,stn}$:

$$I_{stn}(0) = qA_oT^4n_{z,stn}c_{s,stn} \tag{2.15}$$

Calibration with a Langmuir probe using Sheridan's analysis at a stationary location in the plasma must still be undertaken because the current measurement has not been adjusted for effects like the transmission factor of the biased grids or the acceptance angle of the RFEA, for example, however these effects are assumed to be consistent across measurements with the same RFEA and can be accounted for through calibration. Using a density measurement found with the LP at z_{stn}, the current due to a flux of ions incident on the probe can be calibrated [45]. Using this calibration, the local density can be found at any location z:

$$\begin{aligned} \frac{I_z}{I_{stn}} &= \frac{n_z c_{s,z}}{n_{stn}c_{s,stn}} \\ n_z &= \frac{I_z n_{stn} c_{s,stn}}{I_{stn} c_{s,z}} \end{aligned} \tag{2.16}$$

Equation 2.16 shows that knowledge of the local electron temperature is required through the ion sound speed terms.

For a plasma containing an ion beam measured with a source-facing RFEA, one Gaussian centred on V_p can be fit to the local population and another centred on V_b can be fit to the beam population:

$$f(V_D) = \frac{a_1}{2}e^{-(\frac{V_D - V_p}{c_1})^2} + a_2e^{-(\frac{V_D - V_b}{c_2})^2} \tag{2.17}$$

where the $a_1/2$ term is included for isotropic, stationary plasmas as only half of the the local distribution travelling towards the probe is measured [116]. Following from equation 2.17 the current detected by the RFEA for each population can be found from these fits:

$$I_{loc} = a_1c_1\sqrt{\pi} \qquad I_b = a_2c_2\sqrt{\pi} \tag{2.18}$$

where I_{loc} is the current collected by the RFEA due to the local ion population entering the probe at c_s and I_b is the current due to the beam population entering the probe at v_b. If the local density is known, the ratio I_b/I_{loc} can be related to the population fluxes in a similar manner to the local density calibration method described above:

$$n_b = \frac{I_b n_{loc} c_{s,loc}}{I_{loc} v_b} \tag{2.19}$$

Drifting Maxwellians method

The collector current measured by an RFEA due to a single stationary Maxwellian population that has been accelerated through the surrounding sheath is given by the integral of a drifting Maxwellian (equation 2.20) [116].

$$I_C(V_D) = \sqrt{\frac{(n_i/2)^2 q^2}{2M_{Ar}\pi}}\left[\sqrt{T}e^{-((\sqrt{qV_D}-\sqrt{qV_p})^2/T)} + \sqrt{qV_p\pi}\ \mathrm{erfc}[(\sqrt{eV_D}-\sqrt{qV_p})/\sqrt{T}]\right] \tag{2.20}$$

where T is the temperature of the ion population and qV_p is the energy of the drifting population as it enters the RFEA because the local ion population is accelerated by the sheath surrounding the grounded probe. The $n_i/2$ term is included because the local population is treated in the same manner as in the drifting Gaussian-flux method.

For a bimodal ion population in which a beam and a local population exist, like that shown in figure 2.19b, the ion current can be described by the summing the integral of two drifting Maxwellian populations:

$$\begin{aligned} I_C(V_D) = \sqrt{\frac{q^2}{2M_{Ar}\pi}}\Bigg[& \frac{n_{loc}}{2}\Big(\sqrt{T_{loc}}e^{-((\sqrt{qV_D}-\sqrt{qV_p})^2/T_{loc})} \\ & + \sqrt{qV_p\pi}\ \mathrm{erfc}[(\sqrt{eV_D}-\sqrt{qV_p})/\sqrt{T_{loc}}]\Big) \\ & + n_b\Big(\sqrt{T_b}e^{-((\sqrt{qV_D}-\sqrt{qV_b})^2/T_b)} \\ & + \sqrt{qV_b\pi}\ \mathrm{erfc}[(\sqrt{eV_D}-\sqrt{qV_b})/\sqrt{T_b}]\Big)\Bigg] \end{aligned} \tag{2.21}$$

where the subscripts "loc" and "b" refer to the local and beam populations, respectively. The raw $I_C(V_D)$ from an RFEA facing an ion beam can be fit to the integrated Maxwellians in equation 2.21 and the values of n_{loc} and n_b, the local and beam densities, can be extracted directly from the fitting parameters. When the RFEA is oriented perpendicularly to the beam, or there is no beam present, equation 2.20 can be used similarly. These equations do not take into account the transmission factor of the grid or the collection area of the probe and therefore calibration with a LP used at a location of negligible ion flow is still required.

It should be noted that the ion temperatures calculated from the drifting Maxwellian method have been shown to be overestimated due to RF broadening of the measured IEDF

[116], an effect discussed in [118]. In the drifting Maxwellian method, any RF broadening is largely coupled to the temperature parameter, meaning that the calculated ion density is less affected, however in the Gaussian-flux method, the integral used to determine the ion current associated with each ion population is affected by the RF broadening. Where the RFEA is used in this thesis, the plasma densities are typically on the order of $10^9 - 10^{11}$ cm^{-3} and the RF signal is not expected to cause large ion transit time broadening of the IEDF. Ion transit time broadening occurs when the time taken by ions to cross the grounded sheath in front of the probe is comparable to the RF period [118]. In this case, ions respond to oscillations in the sheath, not the time averaged sheath potential, thereby affecting the velocity distribution of the ions entering the probe and resulting in broadening of the IEDF. A comparison of the Gaussian-flux and drifting Maxwellian methods is presented in section 3.5 when characterising the density of the ion beam exiting the source tube of Chi Kung.

2.5 Chapter summary

In this chapter, the Chi Kung and Echidna reactors were introduced and descriptions of their vacuum, gas injection, solenoid and RF subsystems were provided. Both reactors provide vacuum feedthroughs for diagnostic probe access, allowing for measurement of the main parameters of the low pressure plasmas created within, e.g. plasma density, plasma potential, electron temperature, etc. The theory of operation of four electrostatic probes used in these chambers was described and these are used extensively throughout this thesis to characterise plasmas under different experimental conditions.

Chapter 3

Ion beam characteristics in a diverging magnetic nozzle

3.1 Introduction

Diagnosing the behaviour of ion beams accelerated by the current-free double layer (CFDL) created on axis in expanding plasma devices is important for understanding plasma source operation and improving the design of future helicon thrusters. A number of expanding plasma devices worldwide have demonstrated axial CFDLs [55, 57, 119, 120], allowing for investigation of things like particle transport in the presence of a double layer [68, 70, 121], the thrust generated by a helicon thruster [122–124] and the thermodynamic properties of an expanding plasma [125], as a few examples. In most of these studies, *in-situ* electrostatic diagnostic probes are used in regions of high plasma density and strong RF electric fields to measure key plasma parameters like the ion beam energy, electron temperature and plasma potential. While the use of these probes is common they are known to be perturbative to varying degrees, depending on the size and material of the probe, as well as the experimental conditions. Non-perturbative techniques like laser induced fluorescence spectroscopy (LIF) have also been used to characterise expanding plasmas [42, 49, 53, 126], however these make assumptions about ion metastable states and their ability to represent the entire ion population. Still, LIF studies have previously shown the technique's ability to detect and measure the energy and velocity of the ion beam created by double layers in multiple devices [50, 126].

The measurement of beam energy is particularly important to understand thrusters like the HDLT as the ion beam accounts for one of the main thrust generation mechanisms [127]. As such, it is desirable to understand the limitations and applications of the measurement techniques used to measure the beam characteristics. A number of studies have previously

compared ion velocity distribution functions (IVDFs) measured using LIF and RFEA techniques downstream of plasma sources [116, 117], with [113] presenting a comprehensive analysis in this region. However, it remains unclear if the RFEA can characterise the region in which the axial ion beam is accelerated, i.e. in direct proximity to the CFDL.

This chapter reports on experiments conducted in the Chi Kung reactor using a RFEA to diagnose the axial plasma characteristics when operated over a range of pressures, establishing the standard operating behaviour of the reactor. These measurements are compared to those taken previously using non-perturbative LIF techniques to demonstrate the ability of intrusive, *in-situ* electrostatic probes to measure ion beam velocities and densities in regions of high RF and DC electric fields, i.e. in the source and double-layer regions of expanding plasma devices.

3.2 Previous LIF study

The general theory of LIF measurements has been published extensively. As such, the focus here is on previous experiments in expanding plasma devices and, in particular, the study conducted by A. Keesee et al. in [50]. The experiments in the study used a portable, tunable-diode-laser system to take LIF measurements in the Chi Kung helicon plasma reactor. The laser, tuned to 668.6138 nm and aligned on the central axis of the reactor, was used to pump argon ions in the metastable $3d^4F_{7/2}$ state to the $4p^4D_{5/2}$ state while measuring the fluorescent radiation emitted at 442.7244 nm as ions decay from this state to the $4s^4P_{3/2}$ state. The Doppler shift of the emitted radiation yields the velocity of the $3d^4F_{7/2}$ metastable ion species and assumes this is representative of the total accelerated ion population. The fluorescent radiation was measured with optics supported on a tilting mount outside the vacuum chamber, accessing the radiation via a rectangular window. Major components of the LIF setup used in [50] can be seen in figure 3.1. The tilting mount used limited the range of axial measurements to the region from $z = -5$ cm to $z = 25$ cm and the optics allowed for spatial resolution of approximately 1 cm. The laser used in these experiments was of relatively low power and combining this with low plasma densities required RF powers greater than 400 W and long measurement times (5 minutes per measurement), a factor which limited the RF power to a maximum of about 750 W as heating of the system components became a limitation. In this study, Keesee et al. measured the ion velocities in the region of the double layer-like potential structure and showed how the velocities evolved through the ambipolar electric field for two different pressures of neutral argon gas, 0.37 and 0.55 mTorr. The axial velocity profile showed a region of rapidly increasing ion velocity, relating to the

location and width of the double layer and presheath, followed by a plateau region in the diffusion chamber downstream of the double layer as the region of significant ion acceleration had passed. In the same year, many of the same authors also showed that this technique could be optimised, overcoming the limitations of the Chi Kung test campaign; the axial beam energy throughout the entire HELIX expanding plasma device was mapped to show how the beam energy evolves through the potential drop in [49].

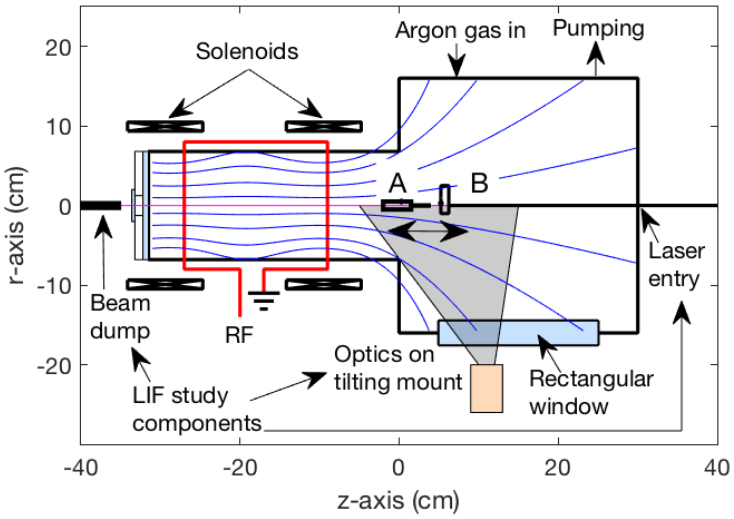

Figure 3.1: Schematic of the Chi Kung reactor showing the components of the LIF study used in [50]. Also pictured is the RFEA mounted in radial-facing (A) and source-facing (B) configurations. In these experiments, the argon gas was inserted through the gas input on the radial wall of the expansion chamber at z=7 cm to match the configuration used in [50].

To compare the measurements taken with the RFEA with those presented in [50], experiments in Chi Kung were conducted with 315 W of RF power supplied to the double-saddle antenna and a current of 6 A was used to power both solenoids. The RF power used here is slightly lower than the power used in the LIF study, however this is not a concern because the ion beam energy is known to be independent of power and far more sensitive to pressure. Argon gas is introduced to the system at pressures ranging from 0.3 mTorr to 0.7 mTorr in increments of 0.1 mTorr. A pressure of 2 mTorr was also investigated as a high pressure limit because previous studies have shown that the population of beam ions disappears at pressures $> 1 - 2$ mTorr as the source potential decreases. For the pressures under investigation, the ion-neutral mean free path is in the range $\lambda_i \sim 1 - 8$ cm, which is comparable to the source

tube diameter for the lower pressures tested.

3.3 Axial ion characteristics

To demonstrate the existence of the ion beam accelerated on axis under these experimental conditions, the RFEA is positioned at $z = 0$ cm, $r = 0$ cm and is used to collect data in both radial-facing and source-facing configurations. Figure 3.2 shows the the normalised first derivatives of ion current detected by the RFEA, dI_C/dV_D. In the radial-facing case, the first derivative exhibits a single peak, representing the local population of ions with a potential of about 38±0.4 V. The data measured by the source-facing RFEA, however, shows two peaks; the first corresponding to the local population as found by the radial-facing RFEA and a higher energy population at about 53.8±0.4 V. The latter is identified as a ∼15.8 eV directional ion beam flowing in the $+z$ direction as it only exists in the source-facing measurements. The beam velocity is found to be 8.7 km/s using equation 2.12.

To fully compare the RFEA results to the previous LIF study, the beam velocity needs to be mapped axially, as opposed to being measured at a single position. Only then can we assess the RFEA's ability to characterise the beam in the acceleration region without significantly perturbing the plasma.

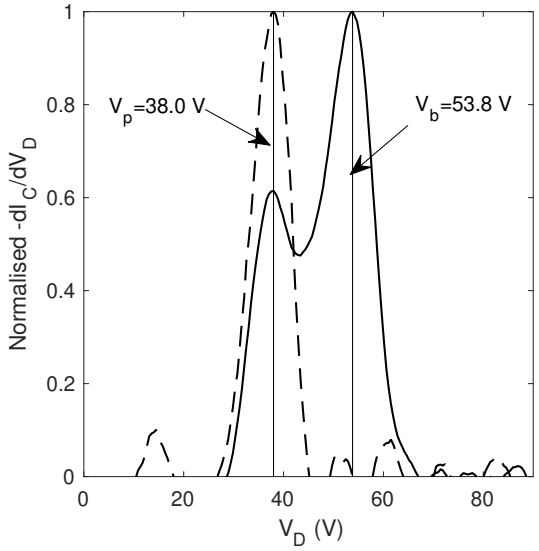

Figure 3.2: Normalised first derivatives of the ion current detected by the RFEA collector plate (I_C) with respect to the discriminator voltage (V_D) for radial-facing (dashed line) and source-facing (solid line) configurations.

Axial plasma potential profiles measured by the radial-facing RFEA for increasing pressures are shown in figure 3.3a. The results show that for 0.3 mTorr, the plasma potential in the source region is significantly higher than in the expansion chamber. Over the axial region from $z = -10$ cm to $z = 0$ cm, the plasma potential decreases rapidly, creating a DC axial electric field accelerating ions into the expansion chamber as the plasma expands through the throat of the diverging magnetic nozzle. With increasing argon pressure, the maximum plasma potential in the source tube decreases, however the potential in the expansion chamber remains much the same. This is illustrated in figure 3.3b which shows that the maximum plasma potential on axis decreases exponentially with pressure, a trend which has been shown analytically and experimentally previously in [128]. In contrast to this, the plasma potential in the expansion chamber is essentially invariant with increasing pressure. These trends imply that, for a constant magnetic field strength, the axial potential drop is mainly dependent on the maximum potential in the source and thereby, the pressure in the system. The location of the potential drop can also be seen to move further downstream as the pressure increases, consistent with the LIF measurements in [50].

The source-facing RFEA was also swept axially and used to identify the existence of an accelerated population of ions in the dI_C/dV_D data for each test pressure. These were found for all pressures but the high pressure case. In measurements at the 'start' of the expansion where the local and beam ion populations overlap, fitting to a double Gaussian can be done to extract the characteristics of each population. The beam potentials in each case are consistent with the maximum plasma potential measured upstream of the potential drop. The beam potentials for the 0.3 mTorr case can be seen in figure 3.3a, however the other pressures were not plotted for clarity.

To illustrate why the position of the potential drop moves downstream, figure 3.4 shows the ion densities measured by the radial-facing RFEA and calculated using both the Gaussian-flux and drifting Maxwellian methods discussed in section 2.4.4 for pressures of 0.3, 0.5 and 0.7 mTorr. The magnitude of the axial magnetic field, B_z, is also plotted in the figure. The figure shows that the Gaussian-flux and drifting Maxwellian methods are in strong agreement. When calculating the local ion sound speed for the Gaussian-flux method, electron temperatures of 8, 6.5 and 6 eV were used for the 0.3, 0.5 and 0.7 mTorr cases, respectively, values which were taken from [129]. The electron temperature is known to vary axially in Chi Kung, however a recent study showed that for the 0.3 mTorr case considered here, T_e dropped from ~ 9 to ~ 7 eV going from the source to the diffusion chamber [125]. As such, by using a T_e of 8 eV, the error in the calculated sound speed would be $< 10\%$. Further, the Langmuir probe used to calibrate the density calculations was used at the stationary location of $z = -25$ cm.

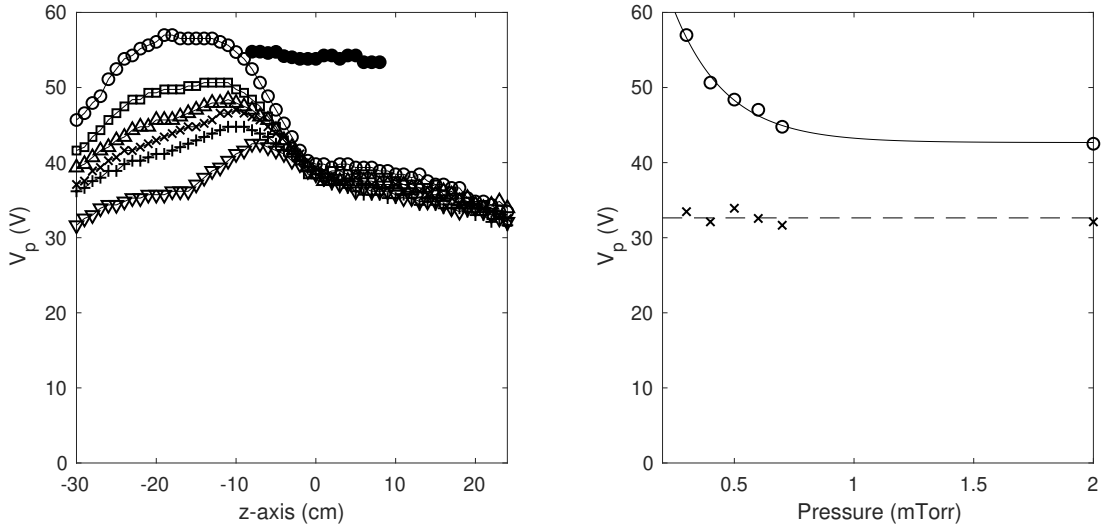

(a) (b)

Figure 3.3: (a) Axial measurements of the local plasma potential using the radial-facing RFEA for pressures of 0.3 mTorr (open circles), 0.4 mTorr (open squares), 0.5 mTorr (open upward pointing triangles), 0.6 mTorr (crosses), 0.7 mTorr (plus signs) and 2 mTorr (open downward pointing triangles). The beam potentials for the 0.3 mTorr case (black filled circles) measured by the source-facing RFEA are also shown. (b) Pressure dependence of the maximum axial plasma potential (circles) and plasma potential at $z = 15$ cm (crosses). The solid line shows the exponential fit to the maximum plasma potentials and the dashed horizontal line shows the average of the plasma potentials at $z = 15$ cm.

For a pressure of 0.3 mTorr, the density profile in figure 3.4 shows a peak density of $\sim 1.5 \times 10^{11}$ cm^{-3} at $z = -24$ cm which then significantly decreases through the source chamber until $z \sim -2$ cm. When the pressure is increased to 0.7 mTorr, the peak density increases to $\sim 2.5 \times 10^{11}$ cm^{-3} and moves 8 cm downstream to $z = -16$ cm. It can be seen that this transition occurs as the density significantly increases in the region between $z = -20$ cm and $z = -10$ cm, immediately upstream of the throat of the magnetic nozzle. For axial positions downstream of the maximum density, the density profile can be seen to decrease with sharper gradients for increasing pressures. This change in density profile brings the maximum density closer to the outlet and moves the location of sharp density decrease downstream. This is reflected in the position of the potential drop shown in figure 3.3a due to the Boltzmann relation.

At the beginning of the potential drop for the 0.3 mTorr case, the Debye length is ~ 0.1 mm and the width of the potential drop is ~ 10 cm, which is approximately 1000 Debye lengths. As such, the potential drops reported here are probably too wide to be considered strictly as

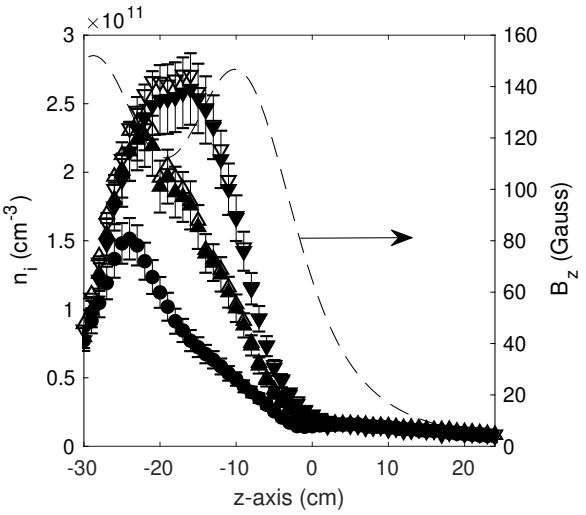

Figure 3.4: Measurements of the axial density profiles using the Gaussian-flux (filled markers) and drifting Maxwellians (unfilled markers) methods for pressures of 0.3 (circles), 0.5 (upward-pointing triangles) and 0.7 mTorr (downward-pointing triangles). The axial magnetic field strength, B_z, (dashed line) is also shown.

double layers and can be thought of as double layer-like structures. With decreasing pressure, these would be expected to approach the classic definition of a double layer as exhibited in the 0.2 mTorr case published in [40].

3.4 Comparison to LIF measurements

The first comparison to the LIF measurements can be made by calculating the maximum beam velocity downstream of the accelerating potential structure using equation 2.12 for increasing pressures. Figure 3.5 shows the maximum beam velocities measured on axis for each pressure tested here. The maximum velocities are seen to decrease exponentially with argon pressure, as illustrated by the fit in the figure. The maximum velocities for the 0.37 mTorr and 0.55 mTorr cases presented in [50] are also plotted in the figure and can be seen to closely follow the same exponential relationship with pressure. As such, the RFEA measurements demonstrate strong agreement with the LIF results in this downstream region.

To fully test the validity of RFEA measurements in the ion acceleration region of Chi Kung, the beam velocities are calculated for the full range of axial positions where a beam is found for each pressure. Figure 3.6 shows the axial beam velocity profiles for each pressure tested here alongside the profiles extracted from the LIF study in [50]. In each pressure case,

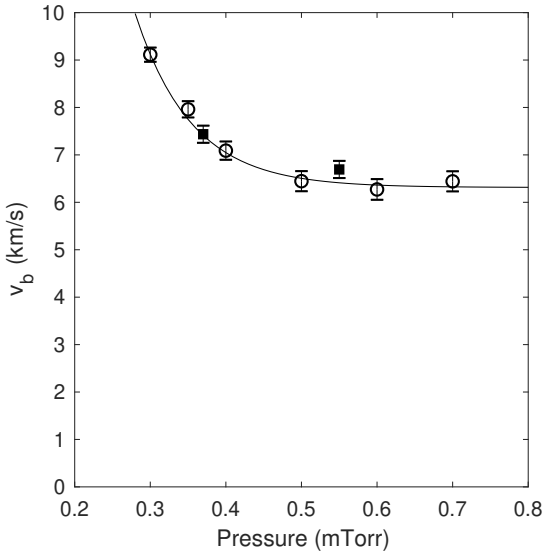

Figure 3.5: Plot of the maximum beam speeds measured for each pressure using the RFEA and equation 2.12 (open circles) fitted to an exponential (solid line). The equivalent LIF data from [50] is also plotted (solid squares) and can be seen to follow a similar trend with pressure.

the axial beam velocity profile can be described by its behaviour in two separate regions; ion acceleration inside the potential drop and relatively constant velocity downstream.

In the region of ion acceleration, the beam velocity is seen to increase sharply due to the DC axial electric field created by the potential drop. For 0.3 mTorr, the beam acceleration was detected in the region from $z = -8$ cm to $z = -2$ cm and an increase in velocity of nearly 4 km/s is observed. In this region, the gradients of the velocity profiles shown in figure 3.6 are related to the square root of the potential drop shown in figure 3.3a for each case. This explains why the gradient of the velocity profile in the higher pressure cases is reduced, i.e. $\sim$2 km/s over a space of 5 cm for 0.6 mTorr. The results in figure 3.3a also showed that the potential profile shifts downstream with increasing pressures, an effect that is also reflected in the locations of ion acceleration in the beam velocity profiles as seen in figure 3.6.

Downstream, the velocity profiles plateau as the sharp potential drop ends. As the pressure increases, the beam velocity plateaus further downstream due to shifting of the potential profile as discussed earlier. Further, for increasing pressures, the transition between the region of ion acceleration and plateau becomes less clear as the end of the potential drop becomes less sharply defined, i.e. the DC axial electric field created by the potential drop nears that of ambipolar diffusion. The magnitudes of the downstream velocity profile also converge with increasing pressure as expected from the exponential relationships between the downstream maximum beam velocity and pressure shown in figure 3.5.

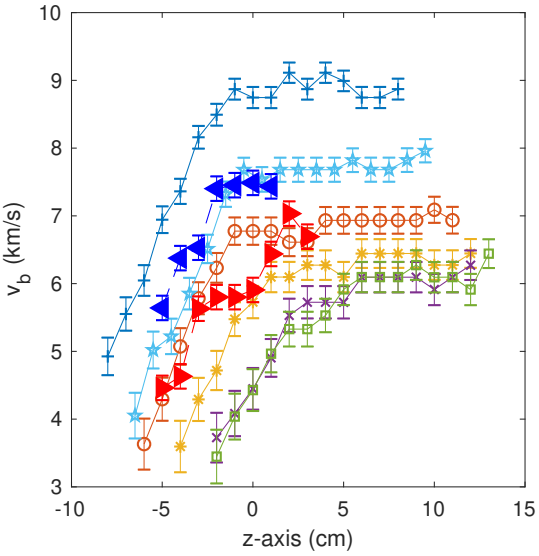

Figure 3.6: Axial profiles of beam velocity derived from the RFEA axial measurements for pressures of 0.3 mTorr (dark blue plus signs), 0.35 mTorr (light blue stars), 0.4 mTorr (orange circles), 0.5 mTorr (yellow asterisks), 0.6 mTorr (purple crosses) and 0.7 mTorr (green squares). The LIF data taken from [50] is also plotted for the 0.37 mTorr (large blue left-pointing filled triangles) and 0.55 mTorr (large red right-pointing filled triangles).

The beam velocity data collected at 0.37 mTorr and 0.55 mTorr in [50] is limited, however based on the limited data, the velocity profiles show good agreement in both profile shape and magnitude between RFEA and LIF results. The 0.37 mTorr LIF case in particular can be seen to match quite closely with an additional set of RFEA data taken at 0.35 mTorr as shown by blue stars in the figure. The error bars of the LIF measurements are quoted as ± 180 m/s and derived from the accuracy of the spectroscopic techniques in measuring the absolute wavelengths of an iodine cell. These error bars are comparable to those used for the RFEA, calculated by using an uncertainty of ± 0.4 V for both local and beam potentials which is carried through equation 2.12, yielding errors that vary between approximately ± 150 and ± 230 m/s in the plateau region for different pressures. These results indicate that even though the RFEA is an *in-situ* technique, operating in regions of high RF and DC electric fields, the ion beam velocity profiles garnered from this technique are comparable to the *ex-situ* non-perturbative LIF technique. This extends the result presented in [113] which showed good agreement between RFEA and LIF techniques in the downstream region but did not explore the region of ion acceleration.

3.5 Pressure dependence of exhaust density

As the RFEA measurements have shown satisfactory agreement with LIF in this region, the RFEA can confidently be used to complete the characterisation of the beam by measuring the beam density. Previously, LIF studies have attempted to measure the beam density in the expansion region [42, 49, 50] but have encountered difficulties due to to rapid metastable quenching that occurs downstream of the double layer. This means that the metastable population used to measure the beam characteristics decays more rapidly than the beam itself in this region, thereby limiting the LIF technique's ability to reliably probe the axial beam density. Using the RFEA, however, assumptions about metastable populations and their ability to represent the entire ion population are avoided because the RFEA collects all ions within the acceptance angle of the probe. Measurements of the ion current incident on the collector plate of the RFEA can therefore be used to calculate the axial beam density profile using the methods described earlier in section 2.4.4. The total ion density, n_{tot}, can also be inferred at each position using: $n_{tot} = n_b + n_{loc}$ [45, 121]. Figure 3.7a shows the calculated parameters for 0.3 mTorr and figure 3.7b shows this data compared to the no-beam reference case of 2 mTorr in the region where a beam is detected (-8≤ z≤8 cm for 0.3 mTorr). The figure shows that both methods of density calculation show satisfactory agreement in this region. An electron temperature of 5 eV was taken from [129] and used when calculating the ion sound speed for the 2 mTorr case. It is worth noting that the Gaussian-flux method results in higher values of density than the drifting Maxwellians method for axial positions further upstream which may be due to ion transit time broadening for the higher pressure, higher plasma density case.

The total ion densities for 0.3 mTorr (lines) and 2 mTorr (downward-pointing triangles) can both be seen to follow the same expansion behaviour, i.e. reducing by a factor of ∼2 over a distance of ∼5 cm, as the magnetic field and geometric expansion are unchanged. At the beginning of the potential drop, all ions in the plasma are accelerated by the DC axial electric field, meaning that n_b and n_{tot} should be equal. As ions are accelerated, some will undergo ion-neutral charge exchange collisions, reducing the fraction of the ion population that exists in the beam. For the 0.3 mTorr case, the location at which the beam population becomes distinguishable from the local population, i.e. at $z = -8$ cm, it exhibits a beam fraction of $\sim 80\%$. This beam fraction at first detection was found to decrease with increasing pressure as the mean free path of ion-neutral collisions subsequently shortens, i.e. $\sim 50\%$ for 0.7 mTorr at $z = -4$ cm, until no beam is detected at sufficiently high pressures, e.g. the 2 mTorr case. As the beam ions travel into the expansion region, ion-neutral collisions deplete the beam population, thereby increasing the population of the local ion population. Figure 3.7a

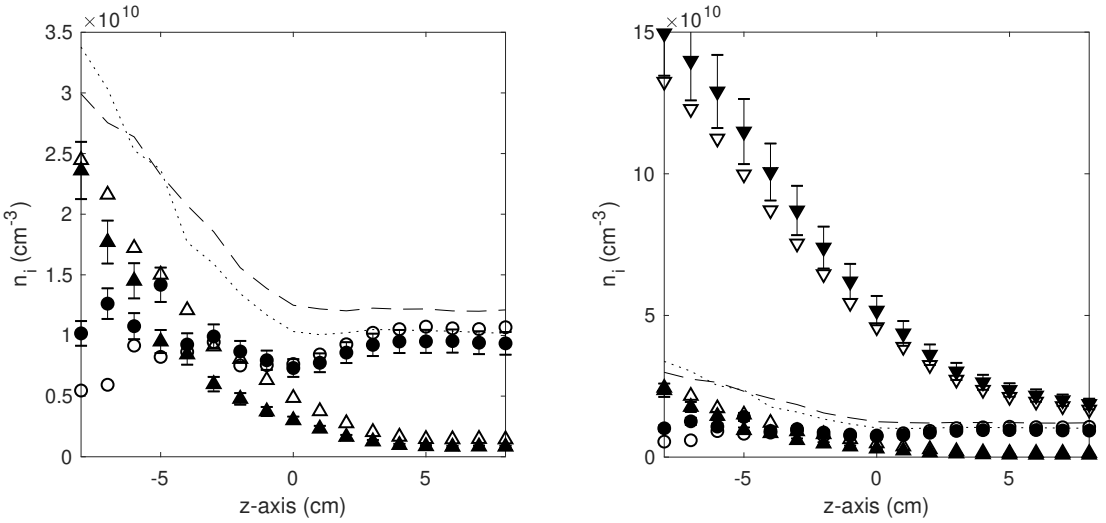

(a) (b)

Figure 3.7: (a) Calculated values of beam density, n_b, (upward-pointing triangles), local ion density, n_{loc}, (circles) and total ion density, n_{tot}, (lines) measured with the source-facing RFEA for 0.3 mTorr using the Gaussian-flux method (filled markers, dotted line) and the drifting Maxwellian method (unfilled markers, dashed line). (b) The same data for the 0.3 mTorr case is plotted alongside the local ion density measured in the high pressure, no beam 2 mTorr case (downward-pointing triangles) in the region of interest.

illustrates this for the 0.3 mTorr case where the data for n_{loc} and n_b intersect at approximately $z = -2$ cm. Further downstream, n_{loc} approaches n_{tot} as the beam becomes undetectable as a separate population in the dI_C/dV_D data and all of the plasma exists as a stationary local population.

The beam densities for each pressure case, calculated using the Gaussian-flux method, are plotted in figure 3.8. The figure shows that for increasing pressure, the decaying beam density profile shifts downstream, as expected from similar shifting of the axial potential, density and beam velocity profiles in figures 3.3a, 3.4 and 3.6, respectively. While the beam densities between pressure cases are of similar magnitude, the higher pressure cases show slightly higher maximum densities with an increase from $n_b = 2.4 \times 10^{10}$ cm^{-3} at 0.3 mTorr to $n_b = 4.4 \times 10^{10}$ cm^{-3} at 0.7 mTorr. The increase in beam density is even more severe when considering the densities at z=0 cm which, for the HDLT, would be considered the exit plane of the thruster. Here, the beam density increases by a factor of about 6 when the pressure is increased from 0.3 to 0.7 mTorr. While the beam velocity for the 0.7 mTorr case is approximately two thirds of the 0.3 mTorr case and it features a smaller beam fraction, as discussed above, the increase in beam density could increase the thrust generated by the

thruster. This might explain why previous studies have shown that maximising the total ion density at the outlet is crucial to maximising thrust [124] (and references therein), sacrificing high beam density fraction and velocity in favour of outlet density, n_{tot}. Further increases in the pressure results in an even smaller beam fractions until, in the 2 mTorr case, there is no beam detected at all but the local density at the outlet is still 3 times higher than the beam density in the 0.7 mTorr case.

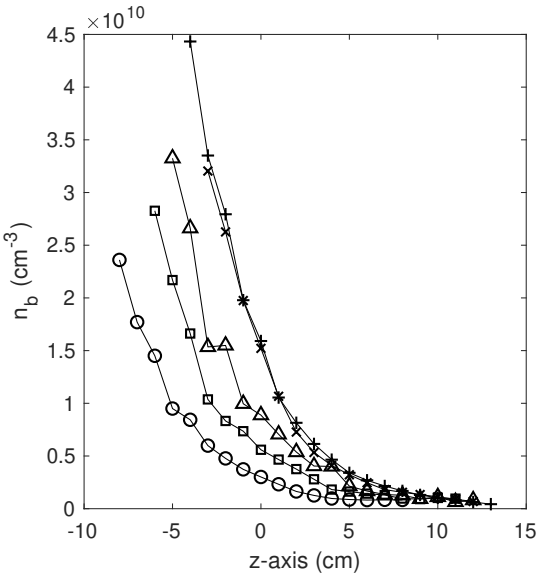

Figure 3.8: Axial profiles of the derived beam densities using the Gaussian-flux method for a constant RF power of 315 W, 6 A in each solenoid and pressure cases of 0.3 mTorr (open circles), 0.4 mTorr (open squares), 0.5 mTorr (open upward pointing triangles), 0.6 mTorr (crosses) and 0.7 mTorr (plus signs).

3.6 Chapter summary

In this chapter, an RFEA mounted in both radial-facing and source-facing configurations was used to measure the axial characteristics of the Chi Kung reactor when operated over a variety of argon fill pressures. At low pressures, the local plasma potential on axis is high in the source region and is shown to decrease rapidly just upstream of the diverging magnetic nozzle, creating a region of high DC electric field which accelerates an ion beam into the expansion chamber. For higher pressures, the source potential decreased, yielding a smaller accelerating potential until at the high pressure case of 2 mTorr, ion acceleration was no longer detectable. With increasing pressure, the location of the potential drop was observed to move axially downstream, an effect which was also seen in the axial density profiles. While

deriving the axial density profiles, the Gaussian-flux and drifting Maxwellian methods of density measurement using an RFEA were shown to strongly agree.

When comparing the RFEA measurements to the LIF data published in [50], the maximum beam velocity in each case was seen to follow the same exponential relationship with pressure. The axial beam velocity profiles in the acceleration region also showed good agreement between the RFEA data collected here and the available LIF data from [50]. The agreement implies that the *in-situ* electrostatic probe does not significantly perturb the plasma when taking measurements in this region where high RF and DC electric fields are present. As such, the RFEA can be used to complete the characterisation of the beam and confidently measure its density. These measurements showed that the beam density was significantly smaller than the local density for locations $z > 0$ cm, giving some insight into why high pressure operation of HDLT-type thrusters has yielded higher thrust values than those run with lower propellant flow rates.

Chapter 4

Shifting the geometric expansion in a diverging magnetic nozzle

4.1 Introduction

All recent lab-based current-free double layer (CFDL) experiments and ensuing ion beam studies in expanding plasmas have taken place in devices where the strongly diverging part of the magnetic nozzle and the geometric expansion are colocated. The Chi Kung reactor is no exception to this and in the last chapter it was seen that a high velocity ion beam is created in this region of colocated geometric and magnetic expansion for a range of pressures. Because most expanding plasma devices feature fixed solenoids and have been primarily used to study the axial ion beam and CFDL, the dependence of plasma behaviour on the relative positioning of the magnetic field and geometric expansion has received little attention. It is also unclear what effect this might have on the generation of high-density conics which form off-axis downstream of the geometric expansion. These are ionised locally by hot electrons transported along the most radial magnetic field lines escaping from the source [66, 68, 70, 72] and have been reported to surround the axial ion beam in a number of devices [70, 71, 73–75]. The effect of hot, radial electron transport to the region where they ionise background neutral in the conics on the axial ion beam and CFDL has yet to be studied.

Only two studies have reported comparisons of the axial characteristics of low pressure expanding plasmas between cases in which the geometric expansion is and is not colocated with the diverging magnetic field [130, 131]. The study by Schröder et al. in [130] used the linear plasma device VINETA to assess the creation and position of double layer potential structures under different magnetic field and geometric conditions. Most relevant to this discussion were the cases studied with and without a tube inserted in the expansion region that extended the

small diameter region of the source tube well past the location of the maximum magnetic field gradient. However, the tube inserted was made out of stainless steel, meaning that the walls would either uniformly charge or be held at a constant electric potential through grounding. As such, the change in material and conductivity could have effects on the plasma behaviour other than just moving the geometric expansion. The study conducted by Ghosh et al. in [131] moved the location of the diverging magnetic field in their HeX device by activating different sets of solenoids mounted concentrically with the cylindrical plasma chamber. They showed that when the maximum gradient of the diminishing magnetic field was ~ 15 cm inside the glass source chamber, the axial potential drop was decreased in magnitude and occurred over a longer axial distance in comparison to when the geometric and magnetic expansions were colocated. However, the study by Ghosh et al. did not investigate the reason for this change or characterise the axial ion flow in the system when the diverging magnetic field and geometric expansion were not colocated.

This chapter reports on experiments aimed at uncovering the effect of moving the geometric expansion away from the location of sharply diverging magnetic field and the importance of hot electron transport and high-density conics formation on the development of double layer-like potential structures in low pressure RF plasmas. To accomplish this, the experiments were conducted in the Chi Kung reactor for cases with and without a 18.5 cm long Pyrex extension tube inserted in the expansion chamber and positioned contiguously with the source tube. The length of the extension tube was chosen to be arbitrarily long enough such that it was greater than two times the ion-neutral mean free path for all pressure cases and intersected all magnetic field lines that led from the source region to the conics, thereby ensuring that when the extension tube is inserted, the diverging magnetic field and geometric expansion are no longer colocated. The details of the source tube were discussed in section 2.2 and is pictured in the schematic of Chi Kung in figure 4.1. Given that the extension tube is made out of the same material as the source tube and is a dielectric, the experiments conducted here are more similar to those presented by Ghosh et al. in [131] than those by Schröder et al. in [130].

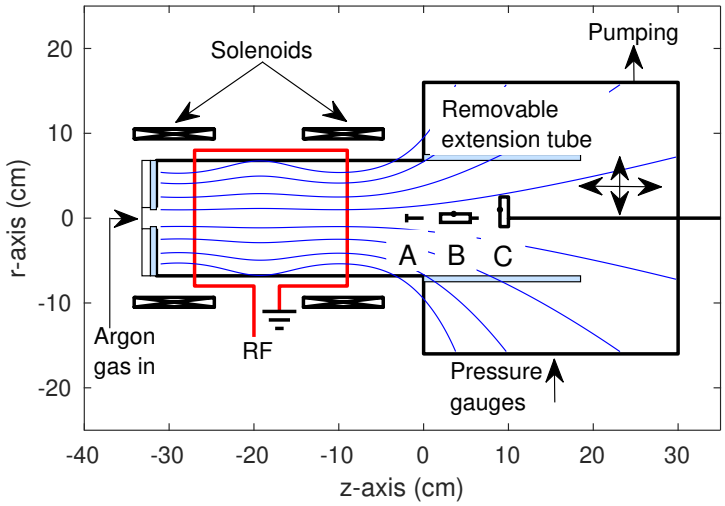

Figure 4.1: Schematic of the Chi Kung plasma reactor showing the removable pyrex extension tube which can be inserted in the expansion chamber, contiguous with the source tube. The diagnostic probes illustrated refer to A) Langmuir probes, B) a radial-facing RFEA, and C) a source-facing RFEA.

4.2 Axial characteristics with an extended source tube

In order to determine the effect of moving the geometric expansion away from the region of high magnetic field gradient, comparisons are made between probe measurements taken with and without the removable extension tube inserted. These cases will be referred to as the "extension" and "standard" cases, respectively. Unless otherwise specified, a neutral gas pressure of 0.3 mTorr, an RF power of 315 W and a solenoid current of 6 A are used to create an inductively coupled plasma in the source region and maintain constant experimental conditions between extension and standard cases. Other than the addition of the extension tube, the only change in the Chi Kung experimental setup between chapter 3 and the present experiments is the location of argon gas injection. In the previous chapter, argon gas was introduced through the radial wall of the expansion chamber at $z = 7$ cm, but in this chapter gas is introduced through the KF-25 port on axis at $z = -33$ cm.

It is interesting to first determine whether an accelerated ion population still exists in the extension case. To measure this, a source-facing RFEA is swept axially in 1 cm increments for both cases and figures 4.2a and 4.2b show the $I_C(V_D)$ data collected at $z = 0$ cm and $z = 10$ cm, respectively, for the extension and standard cases. For the standard case at

z=0 cm, the $I_C(V_D)$ trace is very similar to that shown in the 0.3 mTorr case in the previous chapter, which demonstrates two ion populations at different energies entering the probe. The higher of these two populations, the ion beam, is seen to centre around $V_b \sim 54$ V. When the extension tube is inserted, the $I_C(V_D)$ trace of the source-facing RFEA located at $z = 0$ cm exhibits a single broad population centred around an energy of ∼55 V. Therefore, by inserting the extension tube, the upstream axial potential structure has been altered such that ions are not accelerated to sufficient energies to be measured as a separate ion population at this location and the local plasma potential is increased from that of the standard case.

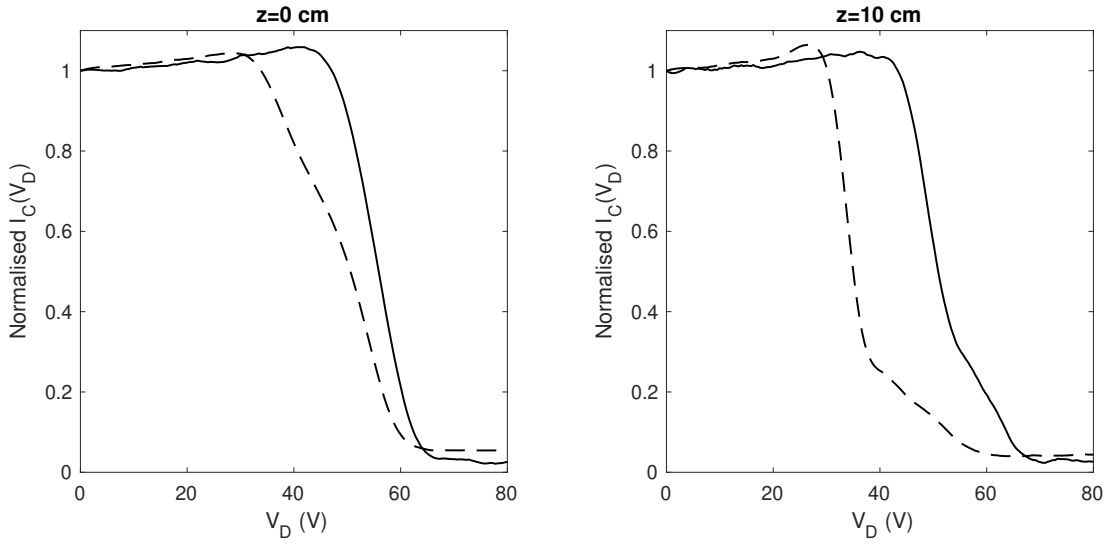

(a) (b)

Figure 4.2: Normalised $I_C(V_D)$ data taken with a source facing RFEA for the standard (dashed lines) and extension (solid lines) cases. The curves in (a) were taken at $z = 0$ cm and those in (b) at $z = 10$ cm. Energetic tails corresponding to accelerated ion populations can be seen in all measurements except for the extension case at $z = 0$ cm.

At $z = 10$ cm, however, the $I_C(V_D)$ characteristics displayed in figure 4.2b demonstrate different plasma behaviour. As expected from previous studies, the standard case demonstrates an accelerated ion population, seen as an energetic tail in the $I_C(V_D)$ data, corresponding to the decayed remnants of the beam measured at $z = 0$ cm. When the extension tube is inserted, the $I_C(V_D)$ trace at this location also demonstrates a bimodal distribution in which one population of ions is centred around ∼49 V and the energetic ions in the tail are centred around ∼62 V. When compared with a radial-facing RFEA at this location it was confirmed that the local plasma potential is ∼49 V, meaning that the energetic tail corresponds to an accelerated ion populated with an energy of ∼13 eV. This shows that when the geometric ex-

pansion is removed from the region of the diverging magnetic nozzle, a directional high energy ion population is still created. However, when comparing the $I_C(V_D)$ data at $z = 0$ cm and $z = 10$ cm, it is clear that the presence of the extension tube has affected the axial potential structure by, firstly, not accelerating an ion population to the same energy (13 eV extension case; 15.8 eV standard case) and, secondly, not accelerating ions at the same axial location.

In order to shed more light on the behaviour of axial ion transport occurring in the reactor, a radial-facing RFEA and an uncompensated Langmuir probe were swept through axial positions from z=-30 cm to z=24 cm for both cases. Figure 4.3 shows the axial ion densities as measured by the Langmuir probe biased to −80 V and analysed using Sheridan's method, as discussed in section 2.4.1. Also plotted in figure 4.3 is the axial magnetic field, B_z, generated by the solenoids. With no extension, the figure shows a maximum density of 1.4×10^{11} cm^{-3} at $z = -25$ cm and decreases axially until $z = 0$ cm where the density is $\sim 1 \times 10^{10}$. Between $z = 0$ cm and $z = 10$ cm there is a slight increase in the ion density resulting from local ionisation due to energetic electrons streaming out of the source region. Beyond this, the density is known to gradually decrease with increasing axial distance from the source through ambipolar diffusion. For the extension case, the maximum ion density increases slightly and its position stays constant to within 1 cm. The axial density profile decreases with increasing z, however in this case, the rate of density decrease is reduced from the standard case. In particular, between $z = -24$ cm and $z = -14$ cm the rate of decreasing density is much smaller, either implying improved containment of ions or additional ionisation compared to the standard case. Downstream of this, the ion density profile decreases sharply before easing gradually to a more constant value at about $z = 10$ cm.

Figure 4.4 shows the local plasma potentials measured by the radial-facing RFEA for both cases. For the standard case, the figure exhibits a sharp potential drop of ∼16 V between z=-13 cm and z=0 cm which was seen in the previous chapter in the 0.3 mTorr case. The DC electric field resulting from this potential structure is responsible for the ion beam detected in figure 4.2a, and shows that the value of maximum potential in the source region is in excellent agreement with the measured ion beam potential discussed earlier. When the extension tube is inserted, the figure shows an overall increase in plasma potential. At z=-30 cm, the potential in the extension case is about 10 V higher than in the standard case which could imply greater charging of the insulating plate terminating the source tube. A similar increase in potential of $\sim 10 - 15$ V is observed downstream of the source tube which could be associated with anisotropic charging of the dielectric extension tube and related changes in the local floating potential, however the direct impact of this is difficult to measure. As such, the measurements reported here probably only reflect the specific case in which the geometric expansion is moved

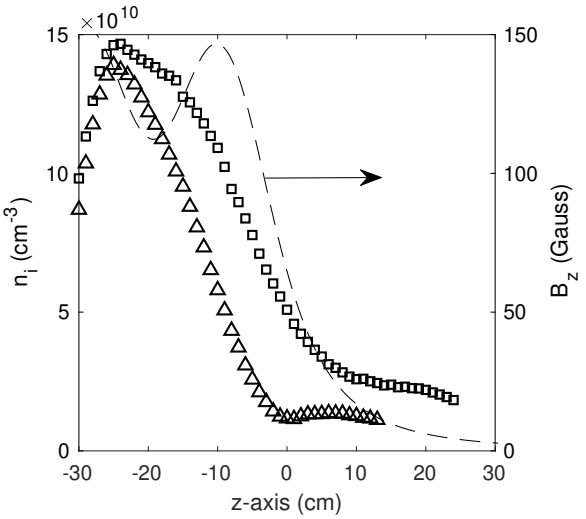

Figure 4.3: Axial ion densities calculated using Sheridan's method on data collected using the uncompensated Langmuir probe for the standard (triangles) and extension (squares) cases. The axial magnetic field is also plotted, showing a maximum of ∼145 Gauss on axis.

with a floating and non-conducting tube. This is a particularly important case as this reflects the dielectric tubes that are often used in the source region of expanding plasma experiments. The effect of tube charging and conductance was, in some ways, shown by the different results presented in Schröder et al. and Ghosh et al. in [130] and [131].

The increase in potential at the back plate and downstream are similar to the measured increase of maximum axial potential in the system from ~ 54 V to ~ 62 V with the inclusion of the extension tube; an increase that is in agreement with the ion beam potentials measured downstream, shown earlier in figure 4.2b. A stark difference between the potential profile in the extension and standard cases is the magnitude of the DC electric field, as measured by the gradient of the potential drop. In the extension case, the potential profile exhibits a potential drop of ~ 13 eV over 18 cm from $z = -12$ cm to $z = 6$ cm, an axial distance 50% larger than the standard case. A similar increase in potential and axial broadening of the potential drop was shown in [131] and can be explained by the Boltzmann relation for potential due to a constant T_e and changing ion density:

$$V_p(z) = V_p(z_0) + T_e ln[\frac{n_i(z)}{n_i(z_0)}] \tag{4.1}$$

Using equation 4.1, $z_0 = -12$ cm and $T_e = T_{eff} = 8$ eV (discussed later) for both cases, the expected potential drop can be calculated and are plotted for each case in figure 4.4. The Boltzmann approximation is in good agreement with the measured potential profiles, demonstrating consistency between the RFEA and Langmuir probe.

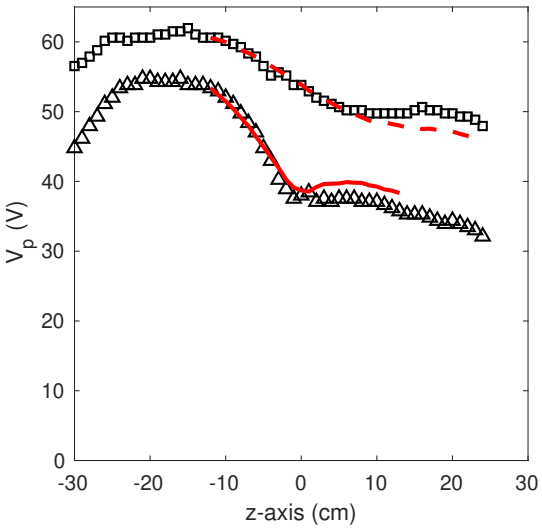

Figure 4.4: Axial plasma potentials measured using the radial-facing RFEA for the standard (triangles) and extension (squares) cases. The red lines show the plasma potentials calculated using the Boltzmann relation and the ion densities from figure 4.3 for the standard (solid lines) and extension (dashed line) cases.

Before analysing the beam behaviour, it is interesting to conduct an investigation of the axial plasma behaviour in the extension case for increasing pressures, similar to the results reported in chapter 3. This was done using the radial-facing RFEA to measure the local plasma potential for pressures ranging from 0.3 mTorr (already discussed) to 0.7 mTorr in 0.1 mTorr increments and a 2 mTorr high pressure case. Figure 4.5a shows the measured values of V_p for increasing pressure. Interestingly, similar effects to those seen in the previous chapter are observed here, e.g. with increasing pressure the source potential decreases and the locations of the maximum plasma potential and the potential drop shift downstream. However, there are also some differences between the behaviour seen here and in figure 3.3a in chapter 3. When the extension tube is inserted, the gradient of the potential drop appears to be largely unchanged by the increase in pressure from 0.3 to 0.7 mTorr. This is reflected in figure 4.5b which shows the maximum plasma potential on axis as well as the value of V_p downstream measured at $z = 20$ cm. The figure shows that the maximum plasma potential on axis follows an exponential trend with pressure, as was the case in chapter 3. However, when the extension tube is inserted, the values of V_p measured at $z = 20$ cm also follow a similar exponential trend with pressure, in contrast to the results of the previous chapter where they were essentially invariant to pressure changes in the standard case. This implies that the downstream behaviour is far more dependent on the source region when the extension tube is inserted. Again, this could be related to the anisotropic charging of the extension tube and

could be explored further in the future.

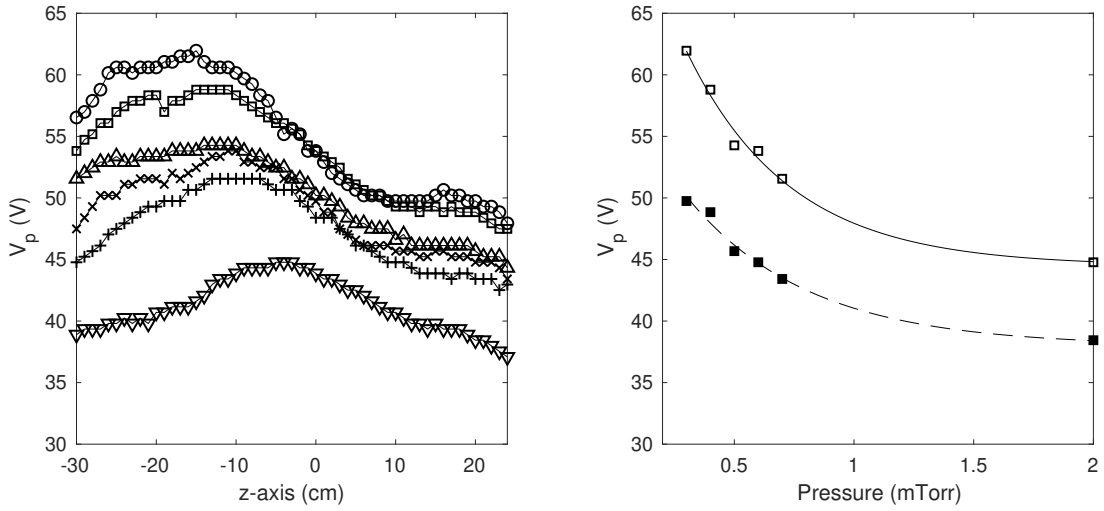

(a) (b)

Figure 4.5: (a) Axial measurements of the local plasma potential using the radial-facing RFEA for pressures of 0.3 mTorr (circles), 0.4 mTorr (squares), 0.5 mTorr (upward pointing triangles), 0.6 mTorr (crosses), 0.7 mTorr (plus signs) and 2 mTorr (downward pointing triangles). (b) Pressure dependence of the maximum axial plasma potential (open squares) and plasma potential at $z = 20$ cm (filled squares). The solid line shows the exponential fit to the maximum plasma potentials and the dashed line shows the exponential fit to the plasma potentials at $z = 20$ cm.

4.3 Effect on the axial ion beam

The axial plasma potential profiles shown in figure 4.4 help to explain the beam measurements in figures 4.2a and 4.2b. For the standard case, the entire potential drop occurs upstream of $z = 0$ cm where a bimodal population was visible in figure 4.2a. In the extension case, however, the potential drop is still occurring at $z = 0$ cm and the RFEA cannot distinguish between the local and accelerated ion populations. As the axial plasma potential decreases, the beam population emerges in the $I_C(V_D)$ data and by $z = 10$ cm, the potential decrease for the extension case has subsided, resulting in a beam with sufficient density and energy to be distinguished by the RFEA, visible as the energetic tail in the $I_C(V_D)$ trace explained earlier.

To determine the characteristics of each ion population entering the source-facing RFEA,

two Gaussians are fit to the dI_C/dV_D distributions, as done in chapter 3. Far downstream, the accelerated ion population becomes non-Gaussian as it decays by ion-neutral collisions and is not treated as a single beam in this study. While directional energetic ions are still measured downstream (e.g. the standard case data at z=10 cm in figure 4.2b), the beam appears as a single gaussian between z=-8 cm and z=8 cm for the standard case and between z=2 cm and z=16 cm for the extension case. Where the beam appears as a single gaussian, the energetic ions are well defined around a central beam potential, meaning they are roughly travelling at the same beam velocity and the beam density can be calculated.

The beam velocity at each position is calculated from the local plasma potential measured using the radial-facing RFEA, the beam potential found with the source-facing RFEA and equation 2.12. Figure 4.6 shows the calculated ion beam velocities and the axial beam velocity profiles exhibit two key behaviours. Firstly, the magnitude of the beam speed in the downstream region for the extenstion case is ∼2 km/s lower than in the standard case, resulting from the total potential drop reduction. Secondly, the rate of axial ion velocity increase is reduced for the extension case, due to the shallower gradient of the potential profile.

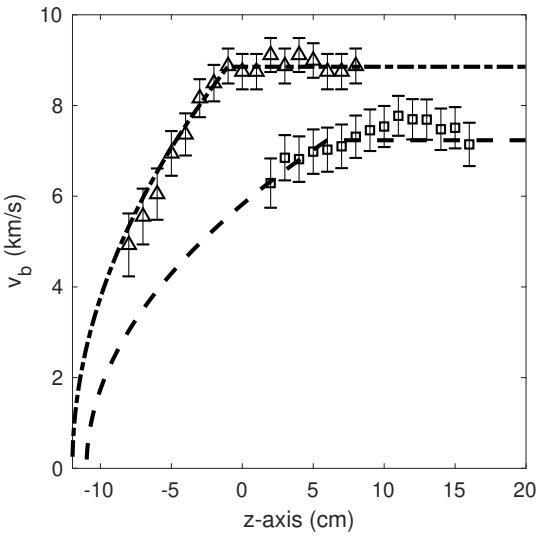

Figure 4.6: Calculated values of the axial beam velocity from the RFEA measurements in the standard (triangles) and extension (squares) cases. The expected beam velocity profiles due to a constant DC axial electric field calculated using equations 4.2 and 4.3 are also shown for the standard (dash-dotted line) and extension cases (dashed line).

To understand the shape of the beam velocity profiles displayed in figure 4.6, modelling of the ion acceleration through the DC axial electric field can be done. The model developed here assumes a zero electric field everywhere except for the region through which there is a

potential drop. In this region, the electric field is set as a finite positive value as determined from the slope of the potential drop, i.e. defined as:

$$E_z(z) = \begin{cases} 0 & z < z_{start} \\ \frac{V_{drop}}{z_{end} - z_{start}} & z_{start} \leq z \leq z_{end} \\ 0 & z > z_{end} \end{cases} \tag{4.2}$$

Where $E_z(z)$ is the electric field in the z direction at the axial position z, V_{drop} is the magnitude of the potential drop in volts, z_{start} is the axial location of the beginning of the potential drop and z_{end} is the axial location of the end of the significant potential drop. Given the force, F, on a singly ionised argon atom due to the influence of an electric field of magnitude E in 1D is given by $F = qE$ then the acceleration experienced is given by $a_z = \frac{qE}{M_{Ar}}$. Given that the acceleration is known as a function of axial position, we can find the velocity via integration and assuming that v_b is zero at the beginning of the potential drop:

$$v_b(z) = \sqrt{\frac{2q}{M_{Ar}} \int_{z_{start}}^{z} E_z(z) dz} \tag{4.3}$$

Figure 4.6 shows the expected beam velocities for the standard and extension cases calculated using equation 4.2, equation 4.3 and the potential results shown in figure 4.4. The figure shows that the axial velocity profile calculated by the simple model can accurately reflect both the shape and magnitude of the measured beam velocity throughout the chamber.

To complete the characterisation of the axial ion transport, the beam density can be determined using the Gaussian-flux method and compared between the two cases. Figure 4.7 shows the calculated values of beam density and total density ($n_{tot} = n_{beam} + n_{loc}$) for the standard and extension cases. In the standard case, the beam density accounts for ~70% of the total density at first detection before decaying downstream. When the extension tube is present, however, the measured beam density is much lower than the total density, accounting for ~13% of the ions present at this location. The absolute value of beam density, however, is of similar order at the end of the potential drop in each case (mid 10^9s cm^{-3}).

As shown by the potential profiles in figure 4.4, the DC axial electric field present in the standard case is larger and acts over a shorter distance than the extension case. In the case with no extension tube, the ions are accelerated more rapidly as shown in figure 4.6 and this accelerated population becomes distinguishable from the background population within one half of a mean free path of ion-neutral charge exchange collisions downstream of the beginning of the potential drop. When the extension is inserted, the magnitude of axial ion acceleration is reduced and the accelerated population only becomes distinguishable ~2 mean

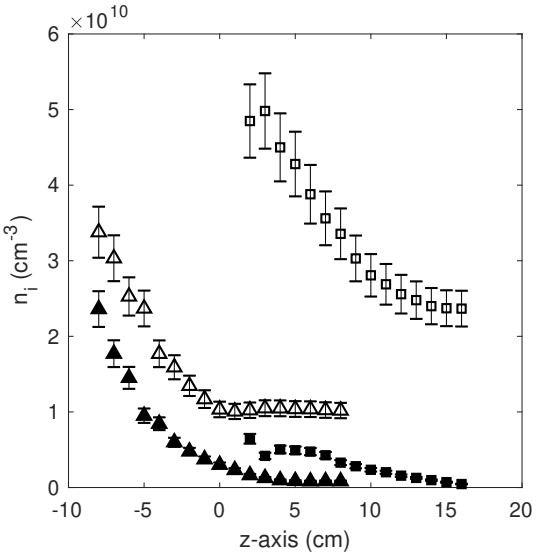

Figure 4.7: Measured values of the beam density, n_{beam} (filled markers), and the total density, n_{tot} (unfilled markers), at locations where a beam is detected for the standard (triangles) and extension (squares) cases.

free paths downstream of the beginning of the potential drop. Therefore, for the extension case, the accelerated ions are more likely to be involved in collisions by a factor of $e^{1.5}(\sim 4.5)$ before being distinguishable by the RFEA, thus reducing their population and adding to the background plasma. This is reflected in the ratio of n_{beam} to n_{tot} between the cases as $70\%/e^{1.5} = 15\%$ which is close to the value of 13% found for the extension case at first detection. These values indicate that the ion beam population is decaying similarly with and without the extension tube present.

4.4 Electron transport

In the previous sections, the axial ion transport behaviour showed that the major differences between the standard and extension cases could be explained by the change in the axial potential profile resulting from the different plasma density profiles. To understand why the density profile has been affected in this way, the electron transport throughout the chamber can be studied. To begin, the RF-compensated Langmuir probe was swept radially just above the beginning of the potential drop at $z = -15$ cm in 1 cm increments to assess any changes in electron heating in the source region. Figure 4.8a shows the EEPFs measured by the RF-compensated probe using the second derivative method (equation 2.6) at $z = -15$ cm, $r = 0$ cm for both cases. The EEPFs shown in figure 4.8a are plotted relative to their local plasma potential, however it should be noted that the plasma potentials measured by

the compensated probe demonstrated the same increase as shown earlier in figure 4.4 at $z = -15$ cm. The EEPFs in the figure demonstrate very similar behaviour, however in the extension case, there is a larger population of electrons in the distribution, which is in agreement with the slightly higher density at this location shown in figure 4.3.

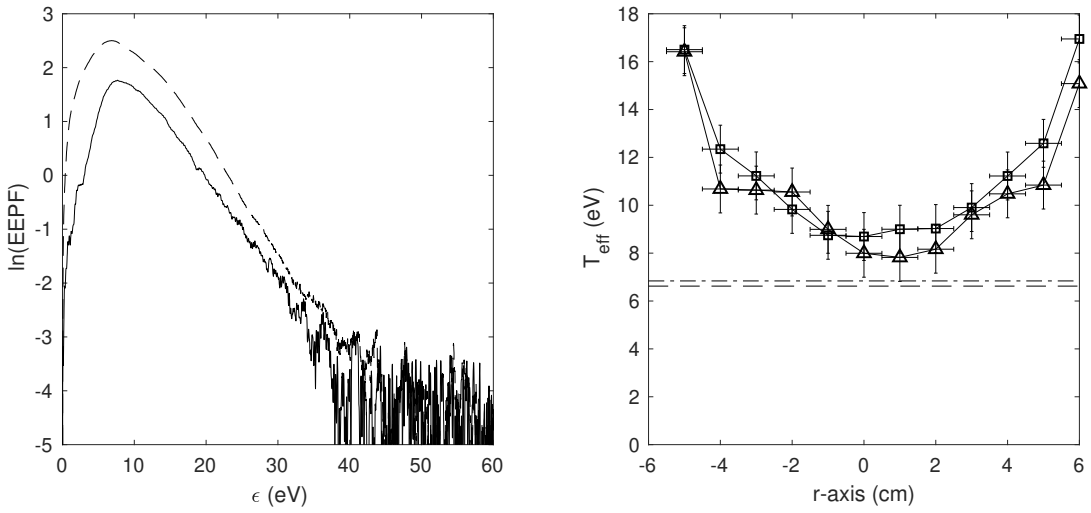

(a) (b)

Figure 4.8: Measurements of the electron behaviour at $z = -15$ cm. (a) The EEPFs measured on axis for the standard (solid line) and extension (dashed line) using the second derivative method for finding the EEPF. (b) The calculated values of T_{eff} as a function of the radial position.

Figure 4.8b shows the radial profile of the effective electron temperature, T_{eff}, calculated using equation 2.8. From the profiles, it can be determined that the radial electron temperature is not significantly affected by the addition of the extension tube even though there is a higher density plasma on axis. The values of electron temperature also match those presented previously in the Chi Kung reactor under similar experimental conditions [67].

At $z = -15$ cm, the magnetic field strength is around 130 Gauss, which means that the electron Larmor radii, r_{Le}, for electron temperatures of 8 and 16 eV are 0.5 and 0.7 mm, respectively. These values are of the order of the RF-compensated Langmuir probe tip radius, i.e. $r_{Le} \sim r_p$. It is therefore unclear if the values of T_{eff} found here using the second derivative method for measuring the EEPF are accurate given that this method is only strictly valid for unmagnetised plasmas, i.e. for $r_p << r_{Le}$. On the other hand, the first derivative method is only strictly valid for $r_{Le} << r_p$, showing that neither method is explicitly valid, however the true value of T_{eff} probably lies somewhere between the two calculated values found using each

method. Figure 4.9 shows the values of T_{eff} calculated using the first and second derivative methods for the standard and extension cases. In each of the standard and extension cases, the calculated values of T_{eff} using the first derivative method are within the ± 1 eV error bars of the second derivative method. This comparison allows for use of the second derivative method throughout the chamber.

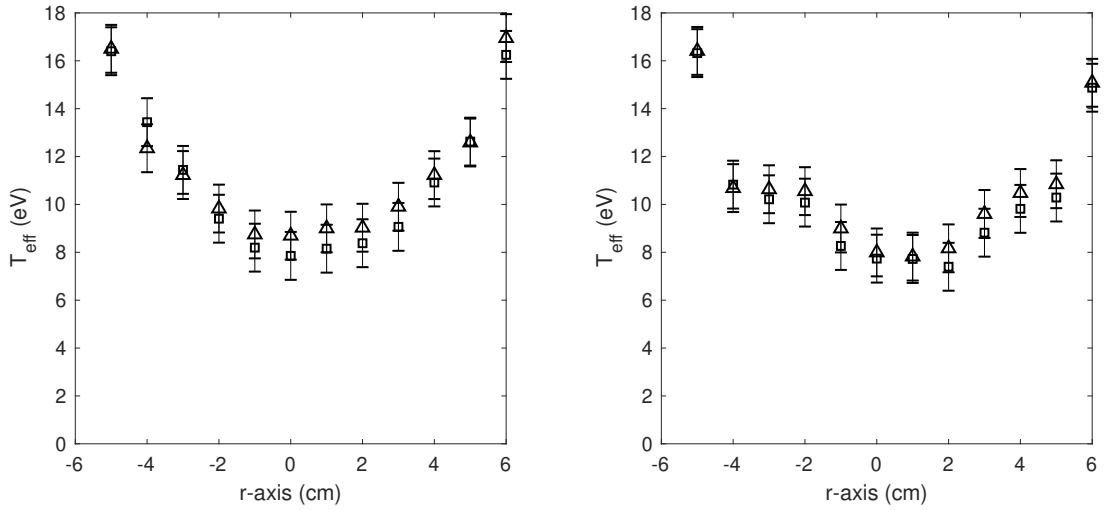

(a) Standard case. (b) Extension case.

Figure 4.9: The effective electron temperature calculated when using the first (squares) and second (triangles) derivative methods for calculating the EEPF in a magnetised plasma.

It is now important to determine if a change in the effective electron temperature would be expected with the addition of the extension tube. As a quick guide, a particle balance for a low pressure, unmagnetised, cylindrical plasma can be undertaken to see if a change in electron temperature should be expected with an increase in source tube length. The particle balance here follows the standard method presented in [3], equating the rates of ion loss to the walls and ion creation in plasma chamber, i.e.

$$A_{loss} c_s = n_g V K_{iz} \tag{4.4}$$

where A_{loss} is the effective loss area of the walls of the chamber, n_g is the neutral gas density, V is the volume of the cylindrical plasma chamber and K_{iz} is the ionisation rate as a function of T_e given by $K_{iz} = 2.34 \times 10^{-14}\, T_e^{0.59}\, e^{-17.44/Te}$. The effective loss area is given by the physical area of the radial and end walls of the cylindrical volume, each scaled by the centre-to-edge ratio for low pressure cylindrical plasmas:

$$A_{loss} = h_L \times 2\pi R^2 + h_R \times 2\pi RL \tag{4.5}$$

where L and R are the length and radius of the cylinder, respectively, and h_L and h_R are the axial and radial centre-to-edge ratios, respectively, given by

$$h_L = 0.86\left(3 + \frac{L}{2\lambda_i}\right)^{-1/2} \tag{4.6}$$

$$h_R = 0.80\left(4 + \frac{R}{\lambda_i}\right)^{-1/2} \tag{4.7}$$

where $\lambda_i = \frac{1}{\sigma_i n_g}$ is the ion neutral mean free path and σ_i is the ion collision cross section.

Solving equations 4.4 - 4.7 for 0.3 mTorr, $\sigma_i = 1 \times 10^{-18}$ m^2 and R=6.8 cm for cases of L=31 cm and L=49.5 cm, corresponding to the lengths of the standard and extension cases, respectively, the electron temperature is found. The results of the particle balance give electron temperatures of 6.8 eV and 6.6 eV for the standard and extension cases, respectively, showing that the electron temperature is only expected to change by less than 3% with the addition of the extension tube. These calculated electron temperatures are displayed by horizontal lines on figure 4.8b and, on axis, are not too dissimilar from the measured values.

4.5 Role of high-density conics formation

Given that the electron heating in the source is unchanged by the addition of the extension tube, there must be another explanation for the different behaviour of the axial ion characteristics presented earlier in figures 4.3 and 4.4. To investigate this, the transport of electrons along field lines connecting the source to locations downstream that would intersect with the extension tube are explored. In this region, it has been reported in a number of experiments that a hollow radial ion density profile forms due to the transport of hot electrons along the first escaping magnetic field lines exiting the source chamber. This is explored in the Chi Kung reactor under the current experimental conditions with the radial facing RFEA which was used to make a 2-D map of total ion current in the region between axial locations $z = -2$ cm and $z = 10$ cm, and radial locations from $r = 0$ cm to $r = 15$ cm for the standard case. The map is shown in figure 4.10a and is reflected about the horizontal axis for clarity, as the system is assumed to be cylindrically symmetric. The figure shows an area of high density forming in this region, aligned with the first escaping magnetic field line (illustrated as the black line). The vertical dashed black line in the figure at $z = 4$ cm indicates a radial slice through the maximum density, the measurements along which are shown in figure 4.10b. The radial measurements at $z = 4$ cm show a flat ion current profile on axis which then increases for positions $r > 4$ cm before diminishing beyond $r \sim 10$ cm. The two dashed lines indicate the beginning of the increased density at $r = 4$ cm and the location of first magnetic field line escaping from the source at $r = 10$ cm. The field line that connects with the location

$(z, r) = (4, 4)$ cm is also plotted on figure 4.10a as a solid black line. Therefore, the hot electrons transported from the source region that ionise the conics must flow along field lines sandwiched between the two field lines shown in the figure. For the extension case, however, these field lines are terminated at the extension tube wall, meaning that they cannot escape to the same region and ionise the conics in the same way. Tracing these field lines back into the source region at the position of maximum density can illustrate the effect of the extension tube and the importance of electron transport along these magnetic field lines.

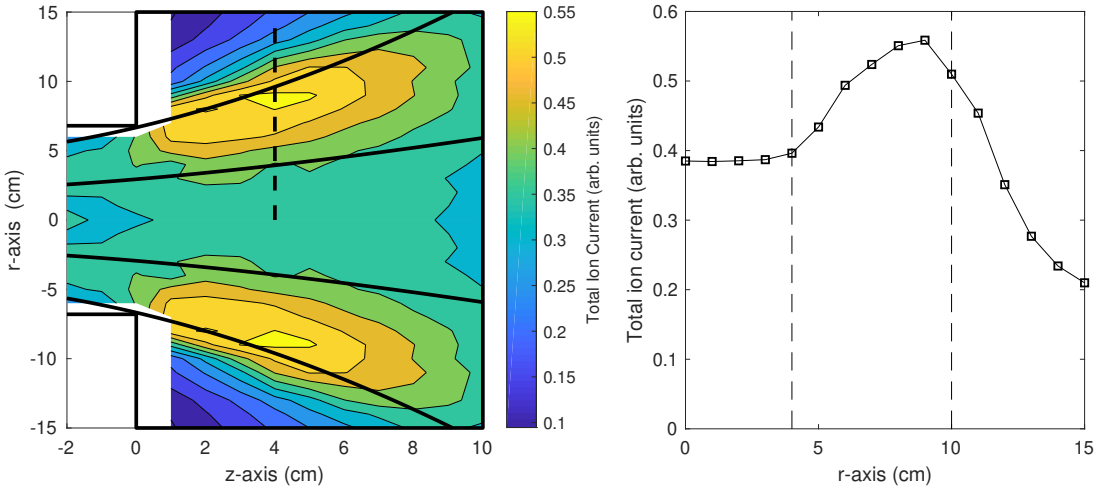

(a) (b)

Figure 4.10: (a) A 2-D map of the total ion current measured by a radial-facing RFEA in the expanding region of the magnetic nozzle. The solid black lines illustrate the most radial magnetic field line to escape the source and the magnetic field line bounding the inner edge of the high-density conics. (b) Radial slice of the total ion current through the location of maximum conics density indicated as the vertical dashed black line in (a).

Figure 4.11 shows the radial ion saturation profiles in the source tube at $z = -25$ cm, i.e. the location of peak density for both standard and extension cases, measured with the uncompensated Langmuir probe. The figure exhibits a radial profile that changes in shape with the addition of the extension tube. On axis, the radial profiles reflect the relative ion densities shown earlier in figure 4.3, however the extension case appears to have increased ionisation off axis. These profiles are also skewed slightly to the negative radial side due to the proximity of a strap of the double-saddle RF antenna. By subtracting the radial profile of the standard case from that of the extension case, the difference in density can be found which is also plotted in the figure. The difference between the two cases demonstrates the increased ion density which appears to be relatively symmetric about the axis. The vertical dashed lines

in the figure are the locations of the same magnetic field lines shown in figure 4.10a, traced back into the source tube. The location of these field lines corresponds well with the increase in ion density, showing that there has been additional ionisation in the region sandwiched between these two field lines. When the extension tube is inserted into the diffusion chamber, the electrons on field lines that would normally ionise the conics can no longer do so. Those that do not have sufficient energy to escape the plasma at the terminating wall of the extension tube are trapped in the source tube, increasing their residence time there. This increase in residence time of hot electrons in the source tube would enhance the rate of impact ionisation along these field lines, as illustrated in figure 4.11. This additional ionisation and subsequent diffusion of ions through the source region also explains the change in axial ion density shown earlier in figure 4.3.

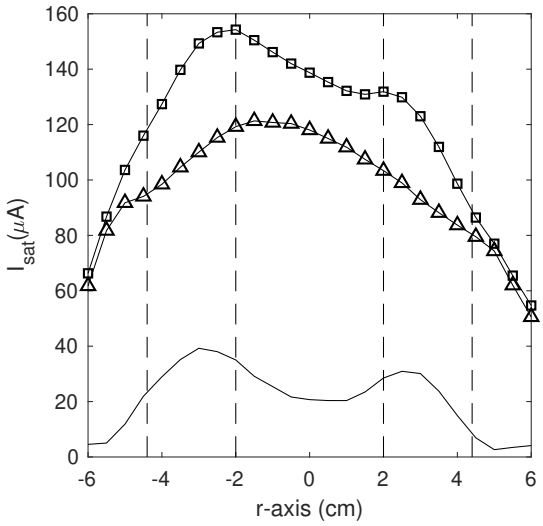

Figure 4.11: Measurements of the radial ion saturation current profiles at $z = -25$ cm measured using a Langmuir probe biased to -80 V for standard (triangles) and extension cases (squares). The difference between these two profiles is shown as a solid line. The vertical dashed lines indicate the radial positions of the magnetic field lines that completely encompass the conics, traced back to $z = -25$ cm.

These results show that the electron transport along the field lines associated with the high-density conics in the downstream region of expanding plasma devices are critical to the characteristics of ion beams formed by the generated DC axial potential structures. When these electrons are not permitted to exit the source region, the resulting increase in ionisation affects the axial density profile such that it has a decreased gradient. This affects the axial potential structure via the Boltzmann relationship, the flow on effects of which are reduced

beam energy and slower ion acceleration which cause smaller beam density at first detection with an RFEA.

The results shown here are, in a way, somewhat counterintuitive in that typically when a loss surface is brought closer to the plasma, the density will decrease. However, in the case where electrons are permitted to escape the heating region along an expanding magnetic field, the reduced residence time of hot electrons in the source will decrease the ionisation rate. By introducing a physical barrier, these populations of hot electrons are contained to the source region, leading to increased ionisation. The radial density profile shown in figure 4.11 for the extension case has a shape typical of the inductive (H) mode heating, whereas in the standard case, the radial density is depleted due to reduced ionisation along the corresponding field lines. This effect might affect the effectiveness of the H mode in expanding plasma devices like Chi Kung where hot electrons escape along these field lines and ionise downstream. Furthermore, the results shown in this study agree with and help to explain the results reported in chapter 3 which showed that increasing the neutral gas pressure decreases the energy of the ion beam and is associated with a changing axial density profile shape. With increasing pressure, the mean free path for collisions in the source region is decreased, leading to higher ionisation rates, effecting the density profile similarly to the effect shown in this study. As such, the effectiveness of the transport of electrons to the conics region downstream would be subsequently reduced.

Now that the electron transport to the conics has been identified as an important factor governing the axial potential behaviour, this hypothesis can be tested by varying the length of the extension tube. Two separate Pyrex glass tubes with the same radial dimensions as the extension tube used throughout this chapter and lengths of 6 cm and 12 cm can be inserted into the expansion chamber, representing cases where the extension tube is shortened to one and two thirds of its original length, respectively. When inserted into the expansion chamber, the 2/3 length extension tube would be expected to block electron transport along essentially all of the magnetic field lines encompassing the conics. However, while the 1/3 length extension tube would block transport to the position of maximum density measured in the conics for the standard case, it would still allow electrons to escape the source along some of the field lines closer to the axis, sandwiched between those plotted in figure 4.10a.

The radial-facing RFEA is again used to measure the local plasma potential on axis and a comparison between the results garnered in the standard, extension, 1/3 extension and 2/3 extension cases are plotted in figure 4.12. While the magnitude of V_p in the 1/3 and 2/3 extension cases is similar to the standard case, the gradient of the potential drop is much more comparable to the extension case. This implies that the extension tubes all have a

similar effect on the axial potential profile because they are blocking the full formation of the conics and the change in the magnitude of the plasma potential could be due to different charging of each extension tube. Interestingly, at the downstream end of the potential drop in the 1/3 extension case, the potential gradient is seen to increase slightly before V_p plateaus which could be indicative of the tube not blocking electron transport along all of the magnetic field lines identified earlier. From these results, it seems that blocking the electron transport to the conics is having a similar and now predictable impact on the axial behaviour of the source.

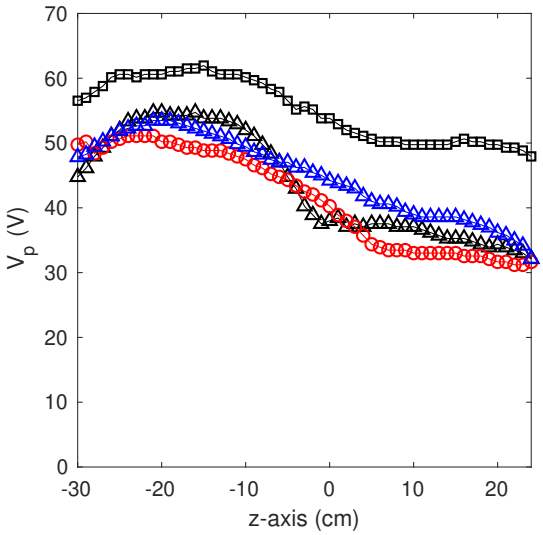

Figure 4.12: Axial plasma potentials measured using the radial-facing RFEA for the standard (black triangles), extension (black squares), 1/3 extension (red circles) and 2/3 extension (blue triangles) cases.

4.6 Chapter summary

In this chapter, the impacts of the geometric expansion's location relative to the diverging magnetic nozzle in Chi Kung were assessed by inserting a dielectric extension tube into the expansion chamber. Data from a source-facing RFEA showed that an axial ion beam was still accelerated, however the beam energy decreased and the location where it was detectable moved downstream. With the addition of the extension tube, the axial ion density profiles, as measured by an uncompensated Langmuir probe, showed an increase in density on axis and a reduction in the gradient of the density decrease in the magnetic nozzle, implying either improved ionisation or containment. The axial plasma potential changed similarly with an

increase in the overall plasma potential, most likely due to charging of the dielectric source and extension tubes, and a decrease in the axial DC electric field which accelerates the ion beam. With increasing pressure, the maximum V_p on axis followed a similar trend to that seen in chapter 3, however the downstream potential was far more dependent on pressure with the addition of the extension tube.

Measurements of the source electron temperature showed little variation between cases with and without the extension tube, showing that higher electron temperatures were not the cause of the increased source density. By investigating the electron transport that would normally occur without the extension tube, the increase of source density can be explained. With the extension tube present, electrons that would normally ionise neutrals in the conics region can no longer access this region and are reflected back into the source region along the magnetic field lines to which they are tightly bound. The increased residence time of these electrons in the source causes the higher plasma densities measured on axis. This behaviour holds true when shorter extension tubes that still block full formation of the conics are inserted in place of the original extension tube.

Chapter 5

Release of select electron populations to high density conics

5.1 Introduction

Many expanding RF plasma devices have shown the existence of the high-density conics that form downstream of current-free double layers (CFDLs) [70, 71, 73–75]. In the previous chapter, it was shown that the axial potential profiles, and thereby the axial ion beam characteristics, in the Chi Kung reactor are quite sensitive to the nature of electron transport along magnetic field lines that would normally pass through the conics region. By blocking this transport with a dielectric extension tube, hot electrons were contained within the source region, increasing their residence time and leading to higher degrees of ionisation off-axis. The resulting increased plasma density affected the DC axial potential profile, yielding a smaller potential drop stretched over a longer axial distance. An ion beam was still detected downstream of the magnetic expansion, however at a larger axial distance from the source than in the case where the geometric and magnetic expansions were colocated. With the extension tube inserted, the beam velocity was shown to decrease, demonstrating that the electron transport along escaping magnetic field lines has a large impact on the beam behaviour.

While enhanced ionisation was shown along the field lines that intersect the region of high density conics formation, the extension tube also intersected many more field lines downstream and therefore did not only just impact the conics region. To overcome this limitation, shorter extension tubes were also tested and the same effects on the axial potential profiles were observed when these essentially only blocked transport to the conics. Another limitation of the experiments described in the previous chapter was that it could not be determined if transport along any particular field lines was more important than transport along others. The

present chapter addresses this limitation and further investigates the critical field lines along which electron transport significantly effects the axial potential and ion beam characteristics. To study this, a variable gap between the source region and the extension tube is used as a geometric window, allowing for the selective release of hot electron populations to the location where high density conics would normally form. By selectively allowing the transport of electrons to the conics region and concurrently measuring the conics density and ion beam characteristics, the critical field lines can be identified.

Figure 5.1 shows the configuration of the Chi Kung reactor used in these experiments. The figure shows the movable extension tube positioned a distance z_{ext} from the source tube, providing a window through which electrons can be transported along magnetic field lines to the region where high density conics normally form. Through knowledge of the magnetic field geometry and by varying z_{ext}, the electron populations that can reach the conics region can therefore be selected precisely. Those that do not pass through the window between the source and extension tube would be contained in the source region as discussed in the previous chapter. To maintain consistency with the previous chapter, the experiments were run with the same experimental conditions of 0.3 mTorr argon gas, 315 W RF power and 6 A in each solenoid.

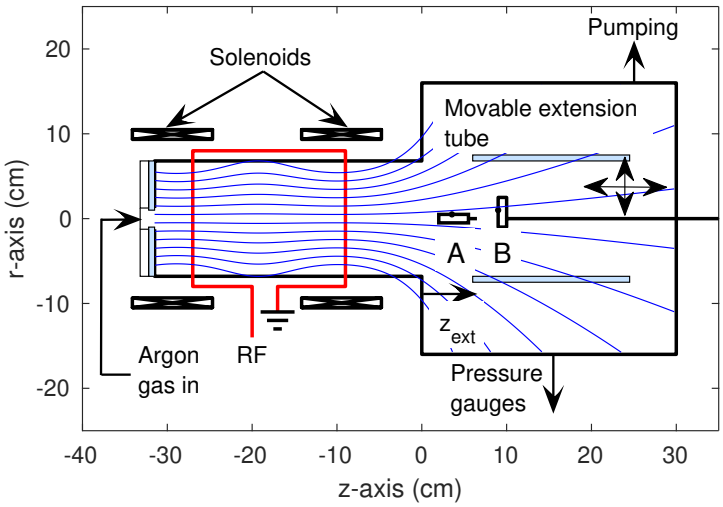

Figure 5.1: Schematic of the Chi Kung plasma reactor showing the movable pyrex extension tube which can be positioned a distance z_{ext} from the source tube. The diagnostic probes illustrated refer to A) a radial-facing RFEA, and B) a source-facing RFEA.

5.2 Exhaust density mapping

To assess the critical magnetic field lines escaping radially to the region where high density conics are normally formed, a radial-facing RFEA (shown as A in figure 5.1) was used to map the density in the region downstream of the magnetic nozzle. The RFEA was swept through axial positions from $z = 0$ cm to $z = 10$ cm and radial positions from $r = 0$ cm to $r = 15$ cm in 1 cm increments. The resulting array combines over 150 measurements, forming a 2-D map of the total ion current measured by the RFEA collecting electrode. The measurements were repeated for values of z_{ext} from 0 cm to 5 cm. The collecting orifice of the RFEA was aligned such that it was kept perpendicular to the measurement plane (i.e. facing out of the page in figure 5.2) which stopped the orifice from directly facing a chamber wall or the extension tube. Figure 5.2 shows the maps of total ion current measured for $z_{ext} = 0, 2, 4$ cm and the no extension case (herein referred to as the "standard" case to maintain consistency with the nomenclature used in the previous chapter). For the $z_{ext} = 0$ cm case, the plasma density outside the extension tube ($r = 8$ to 15 cm) between $z = 1 - 3$ cm was so low that the RFEA could not accurately measure an $I_C(V_D)$ curve.

When the extension tube is contiguous with the source ($z_{ext} = 0$ cm, figure 5.2 (a)) the total ion current can be seen to decrease both axially and radially with increasing z. As z_{ext} increases (figure 5.2 (a)-(c)), a number of changes occur. Firstly, the conics can be seen to form as hot electrons are permitted to escape radially through the geometric window. Secondly, the density profile can be seen to retreat upstream into the source as the distance between the extension and source tubes increases. As the electrons are now permitted to reach the region of the high density conics and ionise there, their residence time in the source decreases yielding less ionisation upstream and the topography of the density throughout the system approaches that of the standard case. In cases where the extension tube is included (figure 5.2 (a)-(c)), the maximum total ion current in the mapped region is measured on axis, however the density of the conics is shown to increase with increasing z_{ext}. In the standard case (figure 5.2 (d)), the maximum total ion current is measured in the conics and this configuration reflects the case in which $z_{ext} \to \infty$. This shows that the electron transport to the conics region begins to dominate the behaviour in the mapped region as the extension tube is situated at increasing values of z_{ext}. The reduction in total ion current on axis is in agreement with the axial density measurements presented in the previous chapter (figure 4.3), in which the density profile in the standard case was seen to decrease further upstream than when the extension tube was placed at $z_{ext} = 0$ cm. Here, the total ion current maps show the downstream density profile transitioning between those shown in figure 4.3 as the geometric window increases and the conics reform.

While the maps presented in figure 5.2 illustrate the emergence of the conics and the retreat of the density profile into the source tube, they do not clearly indicate the shape of the conics density relative to the standard case. Figure 5.3 shows the total ion current measurements along an axial slice at $r = 9$ cm for values of $z_{ext} = 0 - 5$ cm and the standard case. The standard case data (filled triangles) shows an initial increase in total ion current from $z = 1$ cm to $z = 3$ cm before achieving its maximum and decaying with a convex profile to $z = 10$ cm. These characteristics set the benchmark for determining how similar to the standard case the other cases may be.

When $z_{ext} = 0$ cm and the extension tube is contiguous with the source tube (unfilled triangles), no electrons are permitted to escape to the region where high density conics normally form and the figure shows that the total ion current tends to zero for $z \to 0$ cm, indicating why a reliable RFEA measurement was not attainable for $z = 1 - 3$ cm. The ion current can be seen to increase downstream as it gets closer to the end of the extension tube at $z = 18.5$ cm, where plasma is released and is able to diffuse to the locations shown in figure 5.3 . When $z_{ext} = 1$ cm (diamonds), the total ion current has increased but does not reflect any of the characteristics of the standard case. This is because the electrons following the first escaping radial magnetic field line from the source collide with the front face of the extension tube due to its thickness. However, as there is still a 1 cm window available for the plasma to escape through radially via cross-field diffusion, there is a small increase in the plasma density outside the extension tube resulting in the flat profile shown in figure 5.3. When z_{ext} further increases to 2 cm (crosses), the density can be seen to increase dramatically, particularly at locations close to $z = 0$ cm, showing the effect of releasing the electron populations transported along the first magnetic field lines escaping through the geometric window. While the maximum total ion current of the $z_{ext} = 2$ cm case is comparable to that of the extension case, the profile shows different behaviour. The data shows that the peak occurs much closer to $z = 0$ cm than the standard case and the profile decays with a concave shape. These traits are shared with the $z_{ext} = 3$ cm case (squares), however the peak moves downstream by 1 cm with the corresponding 1 cm increase in the geometric window. This behaviour changes when z_{ext} increases to 4 cm (circles) and 5 cm (plus signs). Between these two cases, there is very little change in the total ion current axial profile at $r = 9$ cm. While these profiles do not exactly correspond to the standard case, they have a similar peak value and decay with a convex profile. Given the similarity of the $z_{ext} = 4,5$ cm profiles to the standard case and that there is very little change between these cases, these measurements suggest that the most critical electron populations for formation of the conics have been released. This transition is deemed to have occurred when z_{ext} increased from 3 cm to 4 cm and, as such, the critical

size of the geometric window is 4 cm. For windows smaller than this size, e.g. $z_{ext} = 3$ cm, some critical electrons for conics formation must still be incident on the sheath surrounding the extension tube and do not reach the region where high density conics form. This explains why the density profile at $r = 9$ cm is concave, or depleted when compared to the standard case, for values of $z < 3$ cm.

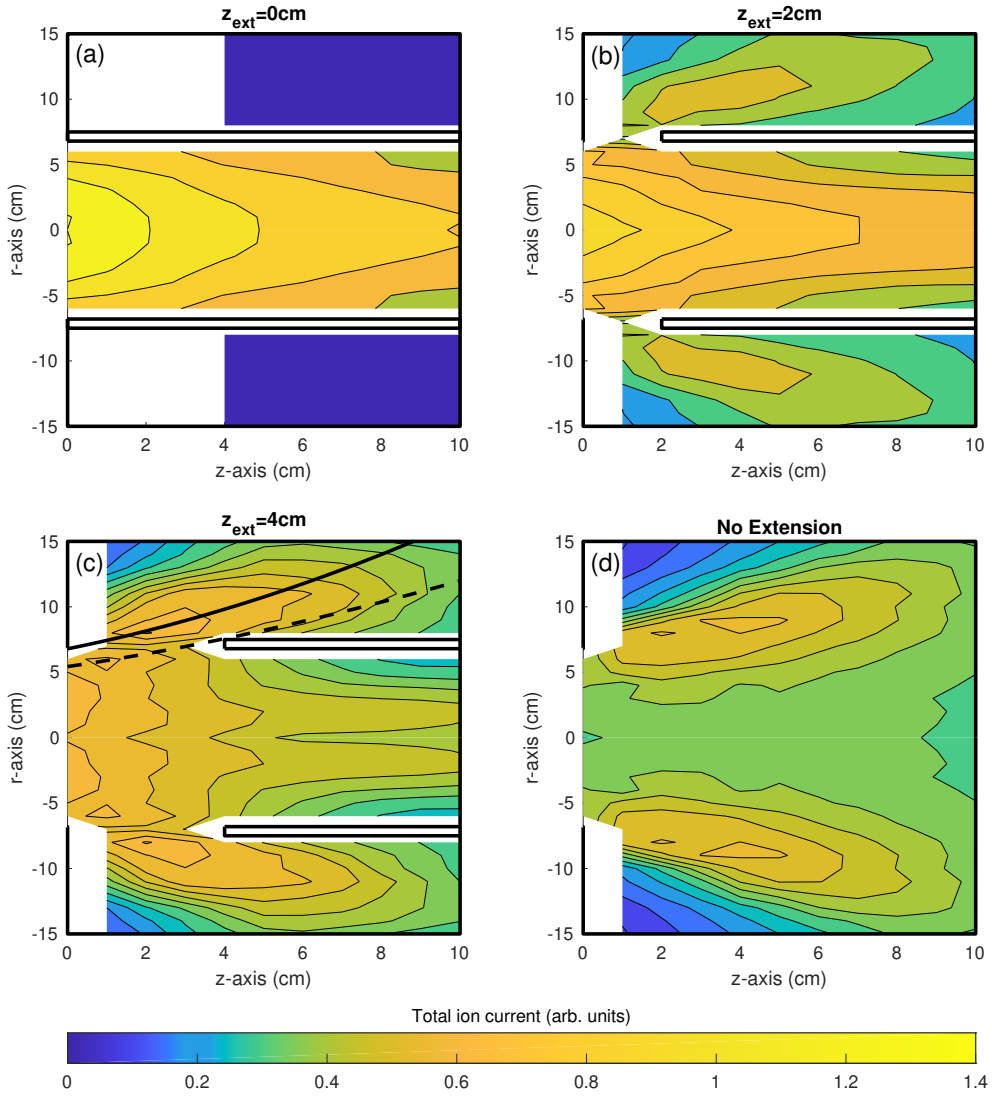

Figure 5.2: 2-D maps of the total ion current collected using the radial-facing RFEA for $z_{ext} = 0, 2, 4$ cm and standard cases. Data was not available for $z_{ext} \leq 3$ cm in the $z_{ext} = 0$ cm case outside the extension tube as the local ion density was too low and the RFEA is unable to measure reliable $I_C(V_D)$ data. The lines illustrated in the $z_{ext} = 4$ cm case are FL1, the first radial magnetic field line escaping from the source (solid black line), and FL2, the magnetic field line that just passes the outer corner of the extension tube (dashed black line).

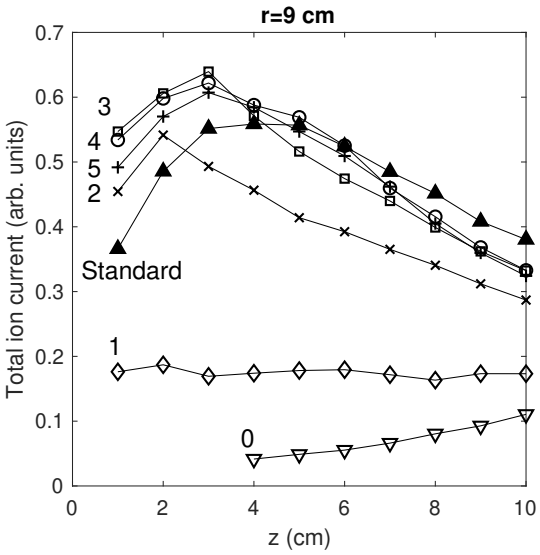

Figure 5.3: Profiles of the total ion current taken along an axial slice at $r = 9$ cm (i.e. in the conics region) for cases of $z_{ext} = 0$ cm (downward pointing triangles), $z_{ext} = 1$ cm (diamonds), $z_{ext} = 2$ cm (crosses), $z_{ext} = 3$ cm (squares), $z_{ext} = 4$ cm (circles), $z_{ext} = 5$ cm (plus signs) and the standard case (filled triangles).

5.3 Effect on the axial ion beam

Given that electron transport along magnetic field lines escaping the source to ionise in the conics is linked to axial ion transport, as shown in the previous chapter, it is interesting to determine if a transition in the beam characteristics also occurs by releasing the electron populations identified in the previous section. To determine this, a source-facing RFEA is used to measure the axial ion beam behaviour in the downstream region for increasing values of z_{ext}. Figure 5.4 shows the beam velocities, v_b, for values of z_{ext} from 0 to 7 cm, calculated using equation 2.12 from measurements taken using the source-facing RFEA positioned on axis at $z = 7$ cm. The axial region of ion acceleration is expected to transition between those in the standard and $z_{ext} = 0$ cm shown in chapter 4 and therefore negligible ion acceleration is expected at $z = 7$ cm for all z_{ext}. The figure also shows the beam velocity for the standard case (black line) with the error bar of ±0.39 km/s (dashed lines) as was shown in chapters 3 and 4.

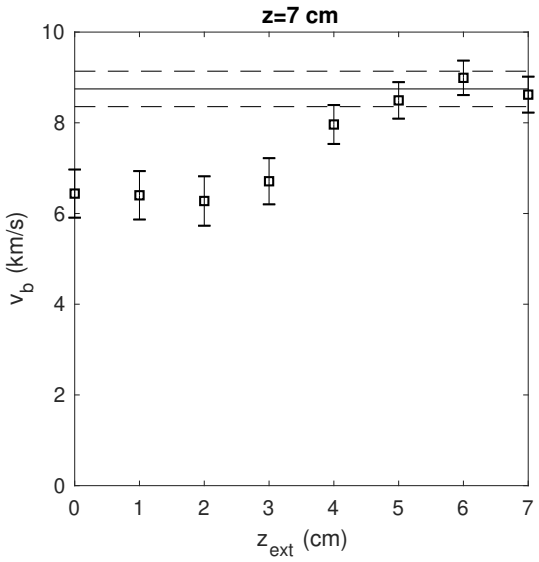

Figure 5.4: Calculated values of the beam velocity at $z = 7$ cm found using the source-facing RFEA measurements. The measured v_b in the standard case is indicated by the solid black line at ∼8.75 km/s with an error bar of ±0.39 km/s given by the dashed lines.

When $z_{ext} \leq 3$ cm, i.e. values for which the conics were shown to have not yet fully formed in figures 5.2 and 5.3, figure 5.4 shows that the beam velocity is relatively constant at the value of the $z_{ext} = 0$ cm case. When $z_{ext} \geq 4$ cm and the major transition in the conics formation discussed earlier has occurred, the beam velocity goes through a step change to the value found in the standard case. As such, figure 5.4 demonstrates a transition in the

beam characteristics at the same critical size of the geometric window as that found earlier in relation to electron transport to the conics. As the ion beam is accelerated by potential structures upstream in all cases, the transition in beam velocity here must be reflected in the magnitude of the potential drop in the double layer-like potential structure. Therefore, by releasing the hot radial electrons through a geometric window 4−5 cm from the interface of the source tube and diffusion chamber, the axial plasma potential characteristics of the standard case have been retrieved.

The source-facing RFEA data used to calculate the beam velocities in figure 5.4 can also be used to calculate the beam density, n_b using the Gaussian-flux method. Figure 5.5 shows the calculated beam densities for $z_{ext} = 0 - 7$ cm at $z = 7$ cm. Also shown is the value of n_b for the standard case (black line). The data shows that the beam density on axis at $z = 7$ cm decreases sharply by a factor of $\sim 2 - 2.5$ when z_{ext} is increased from 0 to 2 cm. This sharp decrease in n_b aligns closely with the values of z_{ext} for which the beam velocities in figure 5.4 have not yet undergone the step change to the velocity of the standard case. From the density maps in figure 5.2, this coincides with the axial density profile retreating upstream into the source region before the conics are fully formed. For $z_{ext} = 3 - 7$ cm, the figure demonstrates a density gradient which is much less severe, reducing by a factor of ~ 2 again until reach the beam density of the standard case.

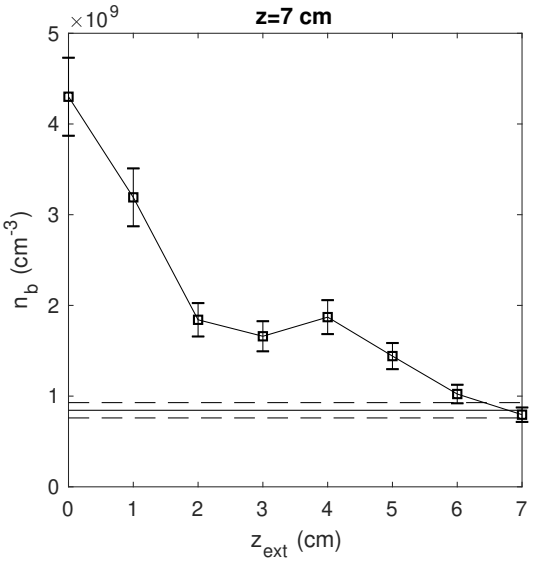

Figure 5.5: Measurements of the beam density at $z = 7$ cm using the source-facing RFEA and the Gaussian-flux method. n_b for the standard case is indicated by the solid black line at $\sim 8.45 \times 10^8$ cm^{-3} with an error bar of $\pm 10\%$ given by the dashed lines.

While it is pleasing to see that the ion beam density in figure 5.5 approaches that of the

standard case with increasing z_{ext}, the trend in n_b is much less striking than that observed in v_b in figure 5.4. While the beam velocity is just a function of the upstream and downstream plasma potential, the beam density is dependent on many more parameters. These include the location and magnitude of the maximum upstream density, the location of the potential structure which accelerates the ion beam and the mean free path for ion-neutral collisions. For example, as z_{ext} increases, the results in figure 5.2 showed that the density contours retreat upstream, an effect which would be reflected in the axial potential profile via the Boltzmann relation. This means that the beam would be accelerated further upstream and would therefore undergo more collisions with background neutral before being detected at $z = 7$ cm. As such, it is difficult to assess the source behaviour and the effect of conics formation from the measured beam densities in the same way that was possible with the measured v_b.

5.4 Analysing the critical magnetic field lines

From the results presented in this chapter, a transition in both conics formation and beam behaviour seems to occur when the gap between the source and extension tubes exceeds ~4 cm. For values of $z_{ext} \geq 4$ cm, the conics density profile shown in figure 5.3 and the magnitude of the beam velocity closely resemble the behaviour of the standard case. This indicates that the field lines that can pass through the geometric window when z_{ext}=4 cm are critical to the axial potential structure that accelerates the beam in the standard case and electron transport along these lines dominates the behaviour of the downstream plasma. At this critical value of z_{ext}, the gap between the extension tube is approximately half of the mean free path of ion-neutral charge exchange collisions at 0.3 mTorr, meaning that it is unlikely that ion transport is influencing these effects. Now that the critical field lines for high density conics formation have been identified and their impact on the beam behaviour elucidated, it is instructive to investigate why it is these field lines that have the biggest impact on the system behaviour.

Plotted in figure 5.2 for the $z_{ext} = 4$ cm case are the first escaping magnetic field line from the source region (solid black line), referred to as FL1 for the rest of this chapter, and the magnetic field line which just grazes the outer corner of the extension tube at $z = 4$ cm (dashed black line), referred to as FL2. Electrons transported along field lines sandwiched between FL1 and FL2 are therefore those that appear to dominate the system behaviour. To understand what makes these field lines important, they can be traced back to the region of maximum density in the source: at $z = -25$ cm, the radial position of FL1 is ~ 4.4 cm and

FL2 is ~ 3.6 cm. The RF skin depth, δ_{RF}, can be calculated using equation 5.1.

$$\delta_{RF} = \frac{c}{2\pi 9000\sqrt{n}} \tag{5.1}$$

where c is the speed of light in cm/s and n is the plasma density in cm^{-3}. Figure 5.6 shows the calculated RF skin depth for the standard and $z_{ext} = 0$ cm cases found using equation 5.1 and the radial plasma density obtained using an uncompensated Langmuir probe. The figure shows that the RF skin depth is very similar between the two cases and has a minimum closer to the centre of the source, increasing radially with decreasing plasma density. At this location, FL2 is $\sim$3 cm from the source tube wall which is $\sim 2 \times \delta_{RF}$, while FL1 is somewhere between $1 - 1.5$ skin depths from the wall. The source of ambiguity in this number is due to the varying value of δ_{RF}, i.e. RF heating is less effective close to the source tube wall because the skin depth is larger, meaning it can penetrate further into the plasma where the skin depth is smaller. As such, this simple analysis shows that approximately $(1 - e^{-2}) \times 100 = 86\%$ of the RF power is delivered to electrons constrained to field lines radially outwards of FL2. Hence, the critical field lines associated with the conics and beam behaviour are those that pass within $\sim$2 skin depths of the source tube wall. Of those electron populations that escape the source tube, those that are magnetised between FL1 and FL2 are the most efficiently heated by the antenna, while the heating experienced by those radially inwards of FL2 is exponentially less effective.

The present results strengthen the conclusions made in chapter 4 which showed a reduction in the beam velocity between the standard case and the $z_{ext} = 0$ cm case. In chapter 4, the potential drop was seen to reduce with the addition of the extension tube and increased ionisation along magnetic field lines that would normally pass through the conics was detected in the source. It was concluded that the extension tube blocked electron transport to the conics and the increased residence time of these electrons in the source region was the mechanism for increased ionisation. The resulting axial density and potential structures followed the Boltzmann relation, and the increased source ionisation resulted in a smaller potential drop over a longer axial distance. In this chapter, it has been shown that when electron transport is permitted through a radial geometric window of a critical size (approximately 4 cm in length), the conics are able to fully reform and the beam velocity returns to that of the standard case. For geometric window sizes greater than or equal to the critical size, the electrons that are most effectively heated by the RF antenna are permitted to escape to the region where high density conics form. As such, their residence time in the source is reduced, decreasing the rate of electron impact ionisation upstream of $z = 0$ cm and a potential structure that accelerates ions to the same velocity as the standard case is recovered. Therefore, the results here demonstrate that beam behaviour is very sensitive to electron transport along the first

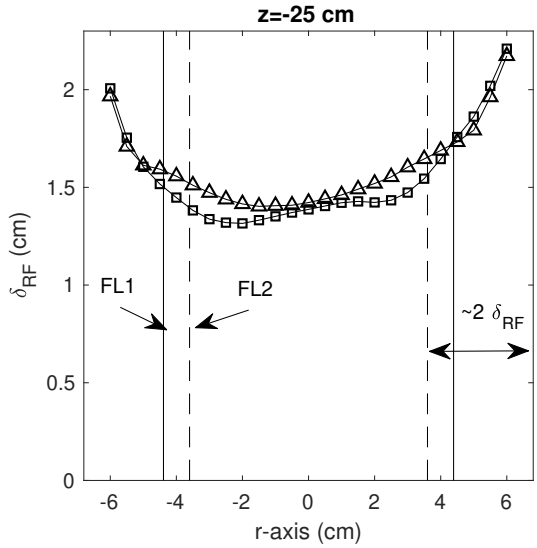

Figure 5.6: RF skin depth radial profiles at the location of maximum axial density, $z = -25$ cm, calculated using equation 5.1 and densities found using an uncompensated Langmuir probe for the standard and $z_{ext} = 0$ cm cases (triangles and squares, respectively). The location of FL1 and FL2 from figure 5.2 are shown as vertical solid and dashed lines, respectively. The location of FL2 is identified to be $\sim 2 \times \delta_{RF}$ from the source tube wall.

escaping magnetic field lines (i.e. those between FL1 and FL2) as these correspond to the electron populations that are most effectively heated by the antenna.

The beam behaviour is much less sensitive to the transport of electrons along field lines radially inwards of FL2 because the RF heating cannot effectively penetrate to these regions due to the radial RF skin depth. This can be concluded because the field lines radially inwards of FL2 still intersect the extension tube when z_{ext}=4 cm, yet the beam velocity shows the behaviour of the standard case. Given that 10-15% of the RF power is transmitted to these electron populations, this might explain why the beam density slowly approaches that of the standard case in figure 5.5 as opposed to the abrupt change seen in the beam velocity. As the extension tube moves further away, it interacts with electron populations that have been heated by exponentially decreasing RF power and the plasma behaviour approaches that of the standard case. The results here also agree quite well with those presented in section 4.5 where the axial plasma potential was studied with shorter extension tubes positioned at $z_{ext} = 0$ cm. As the most critical field lines for conics formation and ion beam velocity can escape the geometric window when $z_{ext} = 4$ cm, it is unsurprising that experiments using the 6 cm extension tube yielded similar axial behaviour to those which used the 18.5 cm extension tube because both would block electron transport along these critical field lines.

The results discussed in this chapter imply that if the geometric expansion in the standard Chi Kung case could be moved slightly upstream relative to the solenoids, the magnetic field lines that currently impact the source tube wall at locations of z just upstream of the outlet would no longer intersect a physical barrier and electrons travelling along them would reach the region of high density conics. As these electrons would be closer to the antenna than those that can currently escape, it may yield an increase in the conics density and beam velocity. Due to the nature of the Chi Kung experiment, shifting the relative location of geometric expansion and the solenoids is not possible, however this hypothesis could be tested using future expanding plasma devices with movable magnetic fields. Further validation of the present study has somewhat been seen in the experiment of Takahashi et al. in [72], in which the RF antenna was moved relative to the magnetic field lines created by a single solenoid and showed that antenna location controlled the topography of T_e throughout the system.

5.5 Chapter summary

In this chapter, the findings of chapter 4 were extended by introducing a gap between the pyrex extension tube and the source region of Chi Kung, creating a geometric window of length z_{ext} through which electrons could be transported along magnetic field lines to the region of high-density conics. Maps of the local ion density collected with a radial-facing RFEA in the downstream region showed the high-density conics reforming as the size of the window increased. The magnitude and spatial structure of the conics density was seen to essentially match the behaviour observed in the standard case when the extension tube was positioned at $z_{ext} \geq 4$ cm. For the same value of z_{ext} at which the conics reform, the axial ion beam velocity, as measured by a source-facing RFEA, was shown to undergo a step change from the velocity found for the $z_{ext} = 0$ cm case to that of the standard case, indicating that the electron transport responsible for the creation of the conics also has a great effect on the axial ion beam characteristics. Similarly, for increasing values of z_{ext} the ion beam density was shown to approach the measured value of the standard case. All of the described effects appear to be dependent on the electron populations streaming along magnetic field lines that can escape to the conics when $z_{ext} = 4$ cm. To understand why these electrons populations are special, the magnetic field lines were traced back to the position of maximum density and were shown to be those that are within 2 RF skin depths from the radial wall. Therefore, the power absorbed by these electrons accounts for $\sim 86\%$ of the power supplied by the RF antenna, potentially explaining why they dominate the system behaviour.

Chapter 6

Field-aligned structures in the throat of a diverging magnetic nozzle

6.1 Introduction

The results of chapters 4 and 5 indicate that the axial beam characteristics in the Chi Kung plasma reactor are heavily dependent on the electron transport to the region of high-density conics formation. By allowing hot electrons to escape the source region of Chi Kung along magnetic field lines that passed through the conics, the axial potential profile was seen to revert back to the standard Chi Kung case. This is linked to a reduction in ionisation in the source region. In the standard Chi Kung configuration, the electron transport to the conics has only previously been described qualitatively. That is, previous authors have written that the electrons are transported from the source along magnetic field lines to the conics [70, 73, 75], but have not described certain aspects of this transport. For example, the previous work has not investigated if or how these electrons interact with the axial double layer (DL) or what determines the observed break energies in the upstream and downstream EEPFs.

Since the conics were first reported, there have been a number of studies published attempting to better explain their role in expanding plasma devices and their ionisation mechanism. Ghosh et al. described that the additional ionisation in the conics is a result of grad-B drift of electrons with energies between 50 and 100 eV [74]. They claim that the grad-B drift results in these electrons rotating azimuthally at velocities of $\sim 1 - 2 \times 10^6$ cm s^{-1}, however the kinetic energy of a rotation of this magnitude is $<$1 meV which is orders of magnitude less than the ionisation energy of argon (15.76 eV). Further, the density of these $50 - 100$ eV electrons is orders of magnitude lower than those with energies closer to the ionisation energy. For these reasons, it appears unlikely that grad-B drift is responsible for the ionisation in the

conics. In fact, Takahashi et al. showed that the electron temperature topography throughout an expanding plasma device was directly linked to the position of the antenna [72]. When their loop antenna was situated on field lines that escape the source, hot electrons were found in the conics region and feature significant electron densities with energies greater than the ionisation energy of argon. When the antenna was placed on field lines that terminated on the source tube wall upstream of the outlet, the hot electrons that would normally ionise in the conics were not found outside the source. Therefore, the hollow density structure downstream is purely related to the electrons heated near the RF antenna and transported downstream, however, the nature of this transport is yet to be fully explored.

2-D mapping of the ion density in Chi Kung has shown that the conics are spatially separated from the source plasma [132]. The source density does not smoothly decrease to the conics and the conics appear as separated islands of ion density. An example of this is shown in figure 6.1 which shows the schematic of the Chi Kung plasma reactor and the 2-D contour of ion density in the conics region for 0.3 mTorr argon gas, 315 W RF power and 6 A in each solenoid. Along the most radial magnetic field line escaping the source, the ion density must decrease from a maximum in the source before increasing again in the conics region. If hot electrons from the source were able to transport freely to the conics, along some iso-potential for example, this would not be observed. Interestingly, previous EEPFs measured on the field line connecting source to conics have demonstrated two-temperature Maxwellians [67, 68, 70]. Upstream in the source region, the EEPFs demonstrate a depleted tail, implying that the source is losing electrons with energy above the break energy. In the conics region, the EEPFs show a hot tail above some break energy and could imply that the hottest electrons could have been accelerated by some potential structure upstream as there are no other heating regions away from the antenna. This chapter aims to clarify the nature of electron transport from source to conics and demonstrate that a field-aligned potential structure can explain the previous break energy and 2-D density measurements.

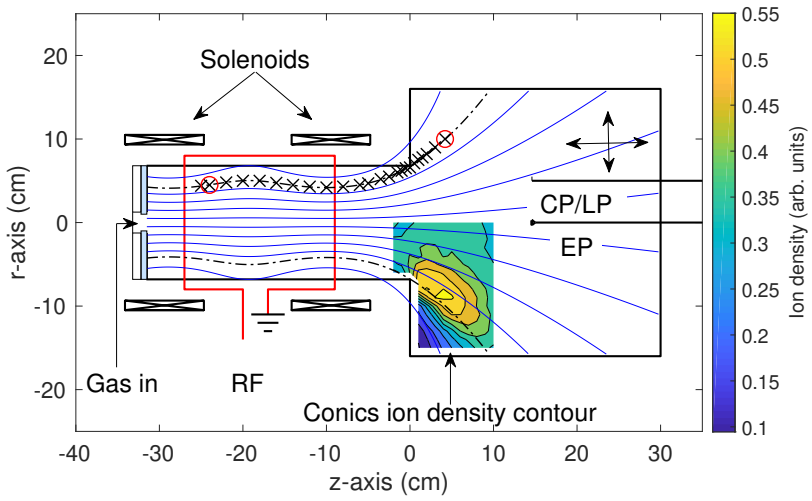

Figure 6.1: Configuration of the Chi Kung reactor used in this chapter. The positions where Langmuir and emissive probes were used along the most radial magnetic field line to escape the source are shown as black crosses while locations where the RF-compensated Langmuir probe were used are shown as red circles. Shown in the lower half plane in the diffusion chamber is the map of the total ion current for the low pressure case, as measured by an RFEA and shown earlier in figure 4.10a.

6.2 Characterising the most radial magnetic field line to escape the source

To investigate the potential structures encountered by the electron population travelling along the most radial magnetic field line to escape the source, the ion density, n_i, and plasma potential, V_p, are measured along that field line using an uncompensated Langmuir probe (LP) and an emissive probe (EP), respectively. The experiments were run under similar experimental conditions as the previous chapters with 315 W RF power, 6 A in each solenoid and for pressures of 0.3 mTorr and 2 mTorr. At 0.3 mTorr, a Boltzmann double layer-like plasma potential structure was shown to exist on axis in chapter 4, whereas chapter 3 showed that the axial structure does not form at 2 mTorr. These pressures are tested here as 'low' and 'high' pressure cases, respectively. The n_i and V_p were measured at positions shown in figure 6.1 as black crosses and are plotted in figure 6.2 against their z-axis locations for each pressure case. Plotting the measurements as a function of z is approximately equal to plotting against the chord length along the magnetic field line in the source region where the field is approximately parallel to the axis. However, near the outlet the field line is at an angle of $\sim 30°$ to the z-axis, meaning the distance along the field line is underestimated by a factor of $1/\cos(30°) = 1.15$.

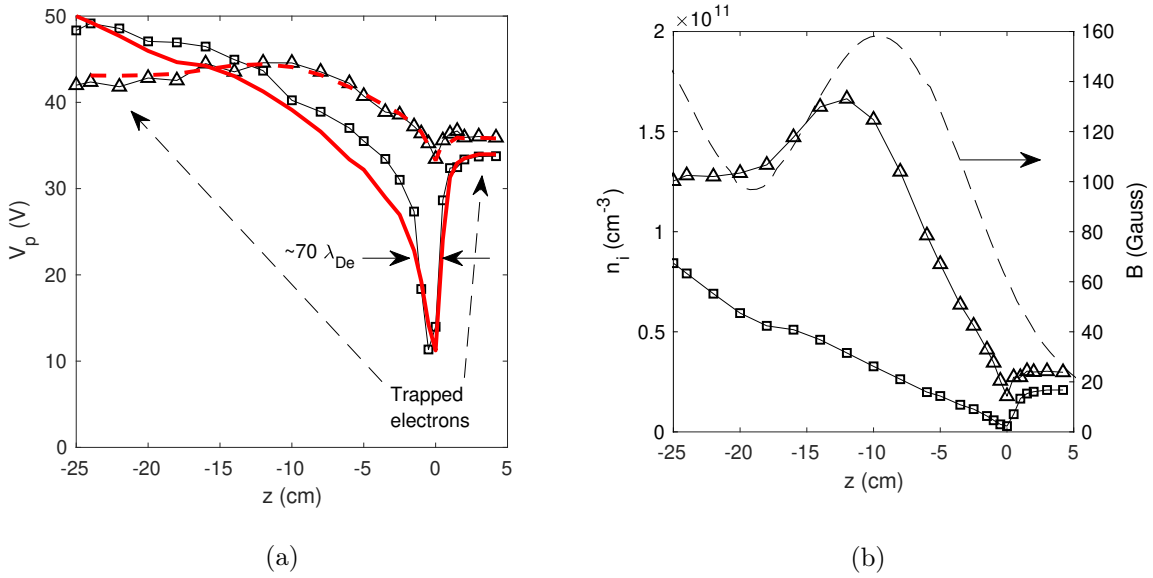

(a) (b)

Figure 6.2: Measurements of the local (a) plasma potential and (b) plasma density along the most radial magnetic field line escaping the source region of Chi Kung at the positions shown as crosses in figure 6.1 for pressures of 0.3 mTorr (squares) and 2 mTorr (triangles). The magnetic field strength along the field line is also shown in (b) as a dashed line. The potentials calculated from the Boltzmann equation are shown for the 0.3 mTorr (solid red line) and 2 mTorr (dotted red line) cases. Electrons can be trapped upstream and downstream of the TL as indicated in (a).

For the 0.3 mTorr case, figure 6.2a shows V_p decreasing with increasing z from a maximum value of ∼50 V at $z = -25$ cm to 34 V at $z = -3.5$ cm, followed by a 6 cm wide sharp potential dip at positions just upstream of the outlet at $z = 0$ cm. Measurements of the EEPF with the CP upstream of the potential dip reveal a bulk electron temperature of 11.5 eV on this field line (discussed later in section 6.3). The Debye length at these locations can be approximated with equation 1.1, using $n_i \sim 10^{10}$ cm^{-3}, and is about 0.25 mm. Therefore, the potential dip structure is ∼250 Debye lengths wide with a full-width half maximum (FWHM) of ∼70 Debye lengths. The depth of the potential dip is approximately 25 V and is therefore about double the electron temperature. Given this potential structure's small width compared to the Debye length and magnitude compared to T_e, it shares many similarities with electric double layers that have been measured in various plasmas [29]. Downstream of the outlet, the plasma potential plateaus to a constant value in the conics region. At 2 mTorr, V_p in the source region is reasonably constant until a small decrease just prior to the outlet. A hint of the sharp potential structure seen in the 0.3 mTorr case is visible in the 2 mTorr case at the same location, however it is much less pronounced.

Figure 6.2b shows the calculated values of n_i from the measured LP data along the field line. For the 0.3 mTorr case, n_i decreases from $\sim 0.8\times10^{11}$ cm^{-3} at z=-25 cm to $\sim 3\times10^{9}$ cm^{-3} at z=0 cm before increasing to $\sim 0.2\times10^{11}$ cm^{-3} in the conics. Again, the 2 mTorr case shows a similar but weaker trend near the outlet. The main differences between these profiles can be described by the behaviour close to and far away from the potential dip at z=0 cm. Far from z=0 cm, the density profiles differ in magnitude and the location of peak density moves closer to the outlet at higher pressure. These characteristics are consistent with those discussed in chapter 3 and the locations of maximum density on the field line for each pressure correspond to the locations of maximum axial density shown in figure 3.4. Near z=0 cm, the profiles in figure 6.2 show a far more significant dip in density and potential at lower pressures. This is addressed later when the effects of wall charging are discussed.

The increase in n_i along the field line found at $z = 0$ cm is directly related to the potential structure and the plasma potential can be calculated using the Boltzmann equation. Figure 6.2a shows the calculated values of the plasma potential profiles using the density data in figure 6.2b, $z_0 = -24$ cm and measured bulk T_e values of 5 eV and 11.5 eV for high (red dotted line) and low (red solid line) pressure cases, respectively. The Boltzmann approximation is in good agreement with the probe data for both high and low pressures, implying that the electron transport is strongly field-aligned in each case. However, it should be noted here that the Boltzmann equation inherently assumes a constant electron temperature, which is not the case in expanding plasma devices like Chi Kung [68].

While its magnitude and width are very similar to a double layer, the potential dip found at 0.3 mTorr is distinctly different from that of a DL (like that found on axis) because the defining feature of a DL is an ion sheath contiguous to an electron sheath which curves the potential down and then up. This means that ions are accelerated towards the DL from one direction while electrons are attracted from the other. Particles in a 1D system containing a DL fit into one of four categories (trapped or free ions or electrons) depending on their energy and which side of the DL they are on [39]. The dip measured along the most radial field line escaping the source of Chi Kung curves down, up and then down again which requires an ion sheath, an electron sheath and then an ion sheath again, i.e. the structure of a triple layer (TL). Such a structure attracts ions and allows for two separate regions of trapped electrons, one upstream (in the source region) and one downstream (in the conics). Ions incident on the potential dip would hit the radial wall and recombine because they are not as tightly confined to the magnetic field line as the electrons.

The TL identified here also acts as an energy barrier for electrons travelling along the field line from source to conics. As electrons climb the potential hill of the TL's upstream ion

sheath they lose energy resulting in less ion-neutral impact ionisation, explaining the depletion of n_i in this region. Electrons with high enough energy to overcome the potential barrier are reaccelerated at the downstream ion sheath, gaining energy useful for ionisation. As opposed to a monotonic field-aligned decrease in density from the source to the conics, the TL creates a region of decreased plasma density followed by an increase in the conics. Electrons can then be trapped in the regions between the TL and the upstream and downstream sheath where the magnetic field line intersects the chamber walls (indicated in figure 6.2a) thereby explaining the spatial isolation of the conics presented previously in [132] and in figure 6.1.

6.3 Electron measurements

Given the magnitude of the potential dip, an electron travelling in the $+z$ direction on the field line at $z = -24$ cm would see a potential barrier of $\sim$40 V. Similarly, an electron travelling from the source that overcomes the potential barrier would then be accelerated by $\sim$22 V into the conics. To test this, the CP was positioned at $(z, r) = (-24, 4.5)$ cm and $(z, r) = (4.2, 10)$ cm (red circles in figure 6.1) to measure the EEPF upstream and downstream of the TL, respectively. The EEPFs are shown in figure 6.3 and demonstrate ε_{break} values of 41.5V and 22V in the upstream and downstream cases, respectively. These values of ε_{break} are in very good agreement with measured V_p profiles and confirm that the TL is affecting the electron transport. The observation of the potential dip also explains where the shape of the EEPFs would transition from demonstrating a hot bulk ($0 < \varepsilon < \varepsilon_{break}$) of electrons to a hot tail ($\varepsilon \geq \varepsilon_{break}$). Hence, the TL acts as a high-pass energy filter on electrons travelling along this field line as those without energy high enough to overcome the 41.5 V potential barrier are not permitted to leave the source region while those that can leave the source are reaccelerated by 22 V, manifesting as the hot population above $\varepsilon \geq 22$ eV in figure 6.3b.

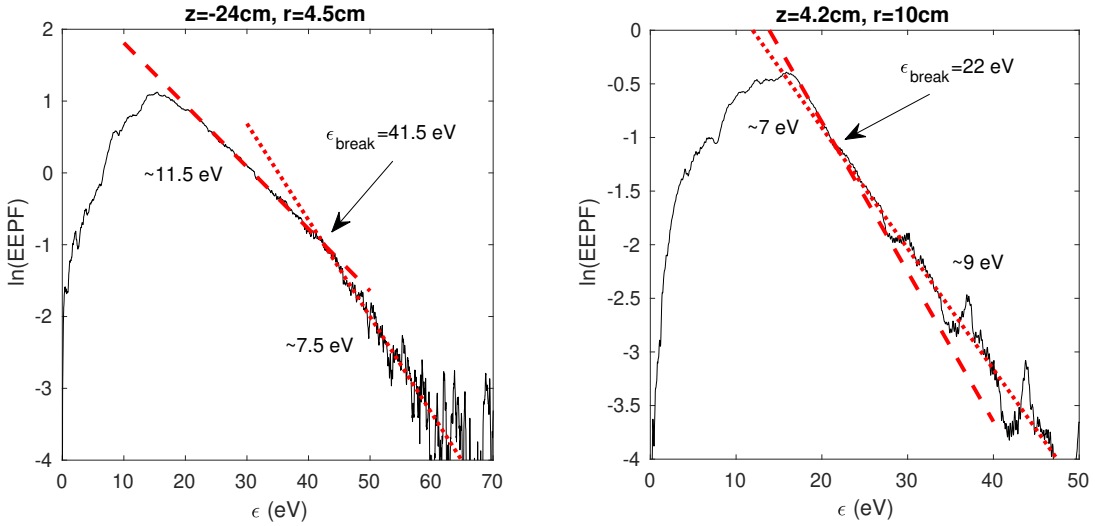

(a) (b)

Figure 6.3: EEPFs measured using the RF-compensated Langmuir probe at positions (a) upstream ($z = -24$ cm, $r = 4.5$ cm) and (b) downstream ($z = 4.2$ cm, $r = 10$ cm) of the TL for the low pressure, 0.3 mTorr case.

6.4 Radial characteristics and wall charging

To determine the radial width of the triple layer, V_p and n_i were measured radially at $z = -0.5$ cm, the z-axis location of the bottom of the potential dip. Here, the measurements at $r = 6.5$ cm correspond to those taken at the bottom of the potential dip in figure 6.2a. Figure 6.4 shows the measured V_p and n_i for the 0.3 mTorr (squares) and 2 mTorr (triangles) cases as well as the predicted potentials found using equation 4.1. The V_p data in figure 6.4a shows very different behaviour between the measured and calculated potentials, with a stark difference at 0.3 mTorr. The observed differences appear to be due to the radial measurements cutting across field lines. As such, it is predicted that each of the radial measurements would lie along their own field-aligned potential profiles conforming to the Boltzmann relation. Figure 6.4b also shows very different behaviour between the two pressure cases. For 0.3 mTorr, the density is much lower than that in the 2 mTorr case, as expected from the results in chapter 3, and the peak density is detected off the axis at $r = 5$ cm. This radial profile is most likely a result of the radial electron temperature profiles which peak at the radial walls of Chi Kung for $z \leq 0$ cm. On the other hand, the 2 mTorr data shows that the radial density profile peaks closer to the axis and decreases towards the edge.

It is interesting to note that the width of the strongly decreasing section of the radial potential profile shown in figure 6.4a for the 0.3 mTorr case is localised to within about 1 cm

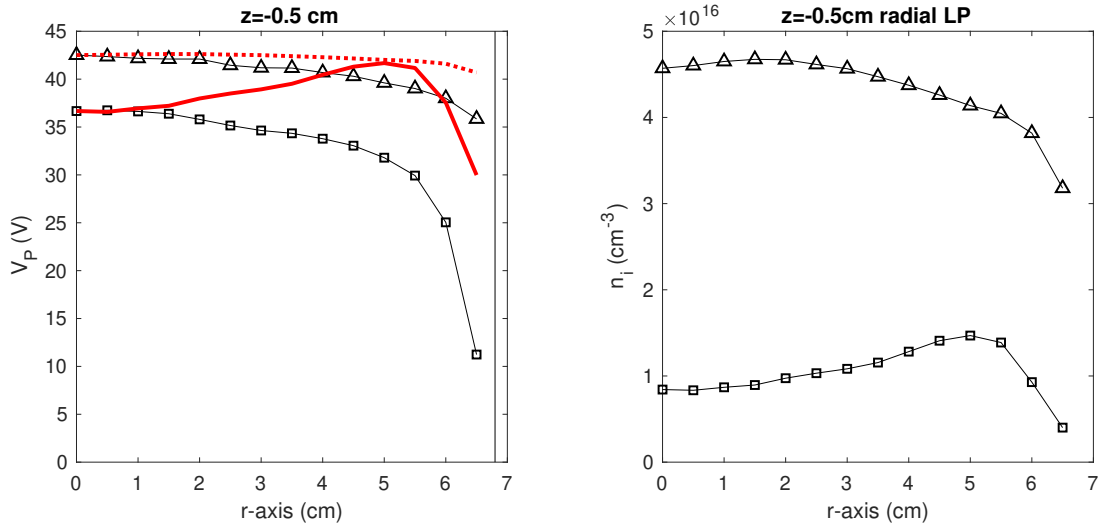

(a) (b)

Figure 6.4: Emissive probe measurements of the radial plasma potential profile at $z = -0.5$ cm for pressures of 0.3 mTorr and 2 mTorr. The potentials calculated from the Boltzmann equation are shown for the 0.3 mTorr (solid red line) and 2 mTorr (dotted red line) cases. The vertical solid line at r=6.8 cm shows the location of the source tube wall.

of the source tube wall (vertical solid line in figure 6.4a). Previous experiments have shown that the source tube wall near $z = 0$ cm becomes significantly negatively charged (∼-40 V) under similar conditions [92]. Hence, particles bound to the magnetic field line must pass by a region of built up negative charges as the field line approaches the wall. Because the electrons are more highly magnetised than ions, their transport along the field line is more affected by the negatively charged wall and information about this boundary condition would be communicated along the entire magnetic field line due to the large mean free paths for electron-neutral collisions which exceed the dimensions of Chi Kung.

Wall charging in Chi Kung is thought to be due to a combination of self-biasing near the RF antenna [133] and charging during plasma breakdown due to the flux of fast electrons inherent to a hot electron population created on field lines that terminate on the wall. Indeed, radial profiles of T_e in the source region of expanding plasma devices have previously shown that the electron temperature increases away from the central axis. This means that increasingly higher temperature electrons will be bound to field lines that intersect the dielectric source wall and cause it to charge negatively as per equation 6.1 [9].

$$V_f - V_p = \frac{kT_e}{2q} \ln\left(\frac{2\pi m_e}{M_{Ar}}\right) \tag{6.1}$$

In equation 6.1, V_f is the floating potential. As $m_e << M_{Ar}$, $V_f - V_p$ is always negative and

the value of T_e determines the magnitude. Equation 6.1 can be evaluated for the 0.3 mTorr (T_e=11.5 eV) and 2 mTorr (T_e=5 eV) cases giving values of $V_f - V_p$ of −53 V and −23 V, respectively. Measurements of V_f at the bottom of the TL (position closest to the source tube wall) can be found from the difference between the measured floating (LP) and plasma potentials (EP). This analysis yields $V_f - V_p$ values of −47 V and −28 V, respectively, which are in reasonable agreement with the values found using equation 6.1. This implies that the source wall charging at the outlet is consistent with the measured values of T_e. It is no surprise then that the field aligned V_p profile of the 2 mTorr case exhibits a less severe potential structure in figure 6.2 given that the temperature of electrons bound to field lines that terminate on the source wall is lower than the 0.3 mTorr case, resulting in less significant wall charging.

Figures 6.1 and 6.2 show that the potential structure is located near $z = 0$ cm, the intersection between the insulating plasma source wall and the grounded wall of the expansion chamber. Given that the TL itself is characterised by a sharp decrease of 25 V towards zero potential it is possible that the potential structure arises to match the boundary conditions imposed by the grounded chamber wall. To ensure that this was not the case, a thin film of insulating tape was used to cover the first few centimetres of the grounded aluminium chamber wall adjacent to this intersection and the experiments repeated. The repeat experiments gave the same results, confirming that this phenomenon is in fact due to wall charging, not due to wall grounding.

6.5 Magnetic presheath

In the discussion above, equation 6.1 was used to justify the negative charging of the source tube walls in Chi Kung and was found to be in quite good agreement with the available probe data. However, equation 6.1 is derived from a 1-D model and only describes the magnitude of the floating potential at a surface surrounded by a Debye sheath. As such, the analysis of wall charging above does not explain the shape of the field-aligned plasma potential or density profiles shown earlier in figure 6.2. A more rigorous analysis of the plasma dynamics along the most radial field line to escape the source tube in Chi Kung as it approaches $z = 0$ cm can be undertaken. In particular, the impact of gyrokinetic effects, i.e. the motion of ions and electrons in the presence of the diverging magnetic field, is explored. For example, consider the Larmor radii of ions and electrons at the bottom of the potential well in the TL. The Larmor radius for ions with a thermal velocity of 400 m/s [134] is approximately 2.5 cm. Based on the thermal velocity of an electron population with $T_e = 11.5$ eV, the electron Larmor

radius, $r_{L,e}$, here is ∼1 mm, meaning that electrons are bound much more tightly to the magnetic field line than ions. Therefore, thermal ions in the region r>4.5 cm at $z = -0.5$ cm will collide with the thin sheath at the source wall, while electrons will not. Ions will be stripped off the magnetic field line while electrons will be transported to the conics. This is a similar situation to the Simon short-circuit effect, where a magnetic field line runs parallel to a conducting boundary [135] and ions can undergo cross-field diffusion to the wall while electrons continue to follow the field line. In Simon's work, the boundaries are conducting and the ion and electron currents to the walls can short-circuit meaning an equipotential can be maintained along the field line. However, the walls in the source region of Chi Kung are insulated and charge negatively due to the hot electron populations which stream along field lines that intersect the source tube wall.

At $z = 0$ cm, the first escaping magnetic field line is at an angle of $\sim 30°$ with the z-axis and the wall. Assessing the field-aligned potential dip in relation to the previous work done on the oblique incidence of magnetic field lines with a boundary could be more pertinent than the case of the Simon short-circuit effect. Chodura was the first to directly address the topic in a 1-D, collision-less model and developed the concept of a quasineutral "magnetic presheath", sometimes referred to as the Chodura layer [136]. Chodura found that there are two conditions of sonic flow along the field lines and these are pictured diagrammatically in figure 6.5. The first is the Bohm criterion where ions must enter the Debye sheath at a velocity perpendicular to the wall of $v \geq c_s$, where c_s is the ion sound speed. Secondly, ions entering the magnetic presheath must be travelling parallel to the magnetic field line at the sound speed, meaning that an additional presheath condition is required upstream of the Chodura layer. As such, the magnetic presheath serves as a region where the direction of ions changes from parallel to the magnetic field to perpendicular to the wall. Riemann showed that the two presheath conditions merge together by extending the work to include collisions [137] and Ahedo was able to recover the particular cases of Chodura and Riemann by generalising the model for different field strengths [138].

In the 1-D collisionless case, Chodura showed that the scale width of the magnetic presheath is given by equation 6.2.

$$\lambda_m = \sqrt{6}\frac{c_s}{\omega_{ci}}\cos(\Psi) \tag{6.2}$$

While there is an inherent dependence on the angle between the magnetic field line and the wall in equation 6.2, the width is also inversely proportional to the field strength due to the dependence on ω_{ci}. Beilis et al. [139] found that when the model used the Boltzmann relation, as is the case here, the predicted presheath thickness (measured along the field line) was incorrect but V_p was always decreasing in the magnetic presheath. Experimentally, Kim

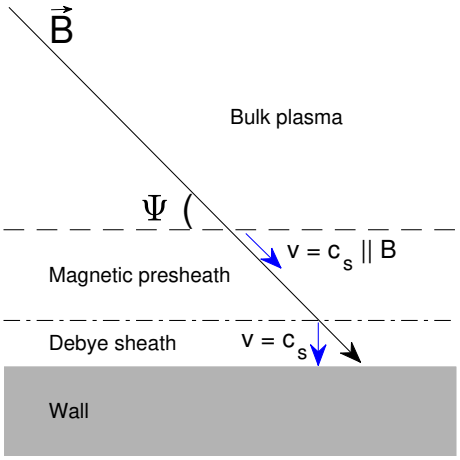

Figure 6.5: Simple diagram of the magnetic presheath as described by Chodura for a magnetic field line, B, incident on a wall at an angle Ψ. At the bulk plasma-magnetic presheath interface, Chodura showed that the ion velocity, here labelled simply as v, is equal to or greater than the local ion sound speed and is parallel to B. A the magnetic presheath-Debye sheath interface, the ions are now travelling at or above the local ion sound speed perpendicularly to the wall.

et al. [140] also showed that the presheath thickness, λ_m, deviated from those predicted from Chodura's theory, i.e. smaller than that in equation 6.2, and could be calculated using equation 6.3.

$$\lambda_m = \frac{c_s}{\omega_{ci}} \cos(\Psi) \tag{6.3}$$

For T_e=11.5 eV, applying equation 6.3 at $(z, r) = (-0.5, 6.5)$ cm, where the magnetic field strength is 60 Gauss, yields a magnetic presheath thickness of ∼31 cm for the 0.3 mTorr case which is approximately equal to the length of the source tube. The descriptions of the magnetic presheath given by Beilis and Kim appear to describe the monotonically decreasing density and potential profiles of the 0.3 mTorr case in the source region seen in figure 6.2 as well as the length scale over which they occur. At higher pressures, the magnetic presheath thickness is expected to decrease with decreasing T_e and the ion-neutral mean free path, which might explain why the V_p measurements along the field line are only seen to decrease from $z = -10$ cm to $z = 0$ cm for the 2 mTorr case, i.e. the spatial width of the magnetic presheath has decreased and this is measured as a shortening of the monotonically decreasing section of the potential profile.

It is difficult to directly compare the current experiment with the previous work as the magnetic field lines in Chi Kung do not maintain a constant angle with the chamber walls,

the magnitude of the B-field is not constant (changing by a factor of ∼2.5 in the source region along this field line) and does not terminate in a normal sheath given that electron transport to the conics occurs. However, the general properties of magnetic presheaths presented in the literature appear to describe the measured behaviour well.

Given that magnetic presheath behaviour is expected to be dependent on the magnetic field strength, the Langmuir probe was used to measure the ion saturation current ($V_{bias} = -80$ V) and the floating potential along the magnetic field line in the vicinity of the TL with increasing solenoid current. Figure 6.6a shows the ion saturation current data for a currents 6, 8, 10 and 12 A in each solenoid. In each case, the data displays a density dip near $z = 0$ cm, indicative of the TL. However, the width of the density dip appears to be decreasing with increasing magnetic field strength. Here, the total width of the potential dip is defined as the distance along the z-axis between $z = 2$ cm and the location upstream where $I_{sat}(z) = I_{sat}(z = 2\text{ cm})$, i.e. where the source and conics densities are equal along the field line. For the the solenoid currents shown in the figure, the width of the density dip appears to decrease linearly by ∼0.5 cm/A from ∼ 10 cm in the 6 A case to 5 cm in the 12 A case. It is difficult to test higher currents as heating could damage the solenoids, however if the linear trend continues, the width would approach zero at ∼22 A. This linear behaviour is mirrored in the floating potential data displayed in figure 6.6b, which shows that the absolute floating potential at the bottom of the TL increases approximately linearly with magnetic field. Given that the floating potential is a measure of the relative fluxes of ions and electrons, it appears that the increasing floating potential would be due to an increase in the ion flux to this position. Indeed, this should be the case given that the increased magnetic field strength would reduce the Larmor radius of ions. As such, they would not collide with the wall as freely and could transport more efficiently to the TL location along the field line, neutralising the electrons also streaming along the same field line.

The linear increase in the floating potential at $(z, r) = (-0.5, 6.5)$ cm is further shown in figure 6.7 for solenoid currents of 6 A to 15 A. By fitting a line to this data, the solenoid current at which V_f would equal 0 V if a linear increase were to continue yields is approximately 20 A. This is a very similar result to that discussed above when considering the width of the density drop in the TL. It seems that interesting behaviour could be observed when the solenoid current is approximately 20 A to 22 A. While these do not prove that the observed density and potential structures are definitely the result of a magnetic presheath, the scale length appears to decrease linearly with increasing magnetic field strength, as expected from equation 6.3 and the flux of ions also increases linearly with a decreasing Larmor radius. Therefore, there is some evidence to suggest that a magnetic presheath could be influencing the plasma transport

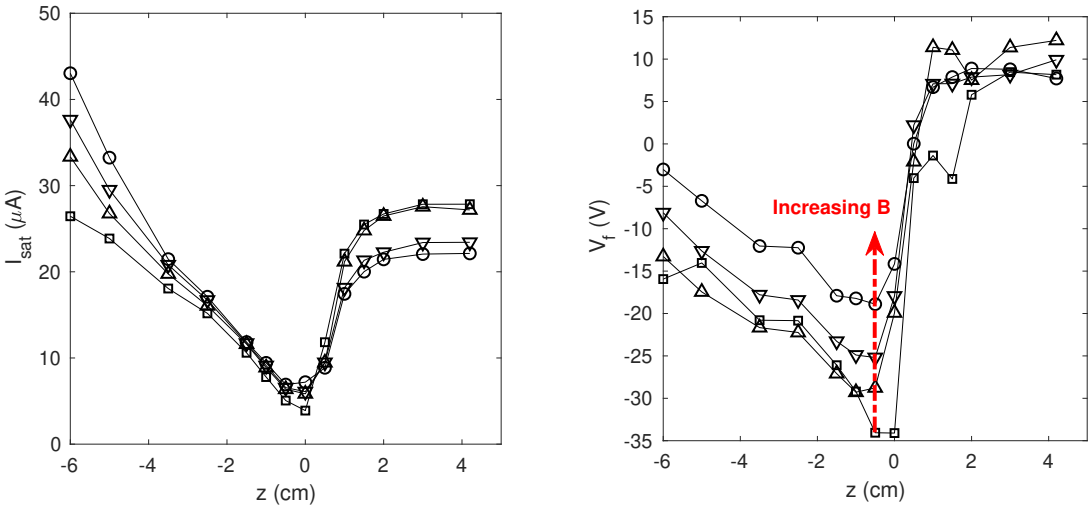

(a) (b)

Figure 6.6: Langmuir probe measurements along the field line in the vicinity of the TL for solenoid currents of 6 A (squares), 8 A (upward pointing triangles), 10 A (downward pointing triangles) and 12 A (circles). (a) shows the ion saturation current a constant probe bias of -80 V and (b) shows the measured floating potentials.

along this field line, however future experiments would have to investigate this further.

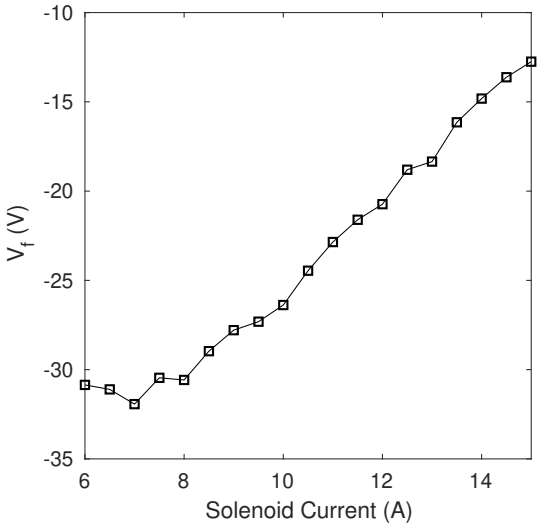

Figure 6.7: Floating potential at the bottom of the TL, i.e. at $(z, r) = (-0.5, 6.5)$ cm as measured by the Langmuir probe.

6.6 Chapter summary

In this chapter, measurements of an electric triple layer situated along the most radial field line escaping an expanding plasma device have been presented. Electron transport was found to be strongly field-aligned and the TL explains a number of previously published measurements. The TL appears to be caused by negative charging of the dielectric source tube by hot electron populations bound to magnetic field lines that terminate on the wall. Electrons travelling along the magnetic field are repelled by the build up of negative charge on the wall, forming a potential barrier for these electrons to escape the plasma source. Those electrons with sufficient energy to overcome the upstream ion sheath of the TL are then accelerated by the downstream ion sheath ($\sim$22 V) and ionise background neutral gas that is present in the conics region. The present experiments show new insight into the nature of the field-aligned electron transport from the source region to the conics in the Chi Kung reactor and other expanding plasma devices where the focus to date has been largely on the axial characteristics of these systems. The diagnostics used in this study were required to be less bulky in order to measure along the field line close to the chamber walls. It is for this reason that the study of the ion dynamics in the TL is difficult as typical ion energy analysers are quite large. Future studies with a specially designed energy analyser could investigate these effects. Further, while it is widely believed that wall charging effects play an important role in the creation of the axial current-free DL [43, 141, 142], how the field-aligned TL affects the creation of the axial DL is not obvious and requires further investigation.

From the findings in this chapter, it is possible that the plasma transport properties along the most radial magnetic field line to escape the source region in Chi Kung are influenced by the presence of a magnetic presheath created due to ions being stripped off the magnetic field line through collisions with the radial source wall. Electrons are not stripped off and those energetic enough to overcome the potential barrier of the TL continue to the conics. There is little to no literature relating to the possibility of magnetic presheath formation in a helicon source, most likely due to the complexity in analysing such a system. However, in expanding plasma devices, both past and present, almost all off-axis magnetic field lines intersect a chamber wall at an an angle and the effects of a magnetic presheath may be measurable and impact on the entire source operation. For example, in Chi Kung, the width of the magnetic presheath might explain why there is a pressure dependence on the location of the maximum axial density. With decreasing pressure, the maximum density on axis was shown to move further upstream from the outlet in chapter 3 which might correspond to the increasing thickness of an off-axis magnetic presheath. The effects of the magnetic presheath might also be important in other plasma devices where magnetic field lines pass close to geometric boundaries, e.g. in the diverter region of tokamaks or in Hall effect thrusters featuring "magnetic shielding" B-field configurations.

Chapter 7

Non-local ionisation in a converging magnetic field

7.1 Introduction

The experiments reported in chapters 3 to 6 were conducted in the Chi Kung plasma reactor. In that reactor, the plasma is created in the region of high magnetic field strength and is allowed to expand through the diverging part of a magnetic nozzle, coincident with a geometric expansion, into a region of lower magnetic field strength. This is analogous to electric propulsion devices, where a plasma exits a thruster into the vacuum of space, and is akin to some astrophysical processes like the origin of the solar wind where a plasma is created in the throat of a magnetic nozzle and is accelerated into regions of much weaker magnetic field [143] (and references therein). This chapter, however, focuses on the opposing situation in which a plasma is created in the weak region of the magnetic field and is incident on a converging magnetic field. This is also analogous to situations encountered in astrophysics like the plasmas observed in the polar regions of the Earth, Jupiter and compact objects such as neutron stars [29, 144, 145]. In these cases, the plasma source is in the weak regions of the magnetic field expansion, far from the dipole, and is incident on a converging magnetic field with increasing strength.

Many linear devices use converging magnetic fields to axially contain plasmas via adiabatic reflection. However, when a plasma source is located on the axis but somewhat distant from a magnetic nozzle, in certain cases, the plasma density has been shown to increase substantially up the magnetic field gradient [79]. This observation has led to some debate on the forces in play and whether simple fluid concepts like the Boltzmann equation can be usefully employed in trying to understand the system. As most of the experiments were not designed to expressly

study this behaviour, this chapter reports the first plasma measurements taken in the newly purpose built plasma reactor named Echidna which, as discussed in chapter 2, features a 1.5 m long glass tube where a solenoidal magnetic field and a radio-frequency (RF) generated plasma source can be progressively separated. Therefore, the work presented in this chapter is exploratory and focuses on the behaviour of a low pressure RF plasma incident on a remote, converging-diverging magnetic nozzle.

7.2 Axial density measurements

To characterise the plasma behaviour when the solenoidal magnetic field is moved away from the RF antenna by the amount $|z_B|$, the experiment was run with an argon fill pressure of 1 mTorr, a relatively low RF power of 200 W and a solenoid current of 40 A, producing a magnetic field with a maximum axial strength of around 300 Gauss (figure 2.3). By sweeping the RF power in the range of 200 W to 500 W and holding the other experimental conditions constant, basic plasma density data at $z = 0$ cm was seen to increase approximately linearly with increasing RF power which implies that the system is operating in an inductively coupled mode [14]. Axial profiles of the local ion density were collected from $z = -80$ cm to $z = 10$ cm in 2 cm increments with the LP for varying positions of the solenoids. Figure 7.1 shows the density profiles calculated using the relation in equation 2.1 for values of z_B varying from $z_B = 0$ to $z_B = -60$ cm in 10 cm increments. Also shown in figure 7.1 is the region directly under the antenna shaded in grey and the location of z_B as a vertical dashed line. The axial magnetic field strength is also shown by the dashed curve in the $z_B = -20$ cm case. When calculating the ion densities, a measured T_e of 5 eV is used to determine the local ion sound speed for the 1 mTorr case (discussed later). For $z_B = 0$ cm, the solenoids are positioned directly over the antenna and the axial density profile exhibits a single peak value of $\sim 4.5 \times 10^{11}$ cm^{-3} aligning with the centre of both the solenoids and the antenna. The density decreases away from this peak as the magnitude of the magnetic field decreases in a manner closely proportional to the strength of the magnetic field as can be seen in the $z_B = -20$ cm case.

Interestingly, the position of peak density follows the movement of the solenoids as they are moved from $z_B = 0$ cm to $z_B = -30$ cm. As can be seen in figure 7.1, the singly peaked axial density profile centred around the value of z_B also increases as the solenoids and antenna are separated and is a maximum at $z = z_B = -30$ cm where $n_i \sim 9 \times 10^{11}$ cm^{-3}. However, this behaviour changes when the solenoids are moved further away from the antenna region. The figure shows that for values of $z_B = -40, -50, -60$ cm the density profiles appear to have

split into two local density maxima; one which is centred on z_B and one that is localised to the antenna region. Both density maxima decrease in magnitude with increasing separation between the solenoids and antenna.

Figure 7.1 indicates that the axial density behaviour can be described by two separate regimes. In the first regime, when the solenoids are positioned within 30 cm of the antenna, the density profile is entirely centred on z_B. In the second regime, the solenoids are positioned further away from the antenna and the plasma is characterised by two local maxima centred on z_B and the antenna. It is interesting to examine the transition between these two regimes, exploring the mechanism behind the large increase in plasma density on axis exhibited in the $z_B = -30$ cm case and attempting to understand why the density decreases beyond this point.

First, the plasma transport in the $z_B = -30$ cm case is investigated to better understand why the plasma density is a maximum at the remote solenoids. Also shown in the $z_B = -30$ cm plot in figure 7.1 is the axial plasma potential measured using the EP. The plasma potential demonstrates a peak value of 60 V in the region of the solenoids. Under the antenna, $V_p \sim 53$ V, yielding an increase in plasma potential of about 7 V from antenna to solenoid. This would generate an axial electric field that would act to accelerate electrons towards the solenoids while repelling ions which could be a possible mechanism of how electrons might be transported to the solenoids as the electric field would tend to balance the effect of adiabatic reflections caused by the strong magnetic mirror ratio present in the system when the solenoids are far from the antenna. An analysis of the relative strength of the ambipolar electric field compared to the magnetic mirror force can be undertaken to determine if either is dominating the plasma dynamics. The magnetic mirror force, F_B, acting to oppose the velocity of an electron moving towards the magnetic field from the $+z$ direction is given by equation 7.1 [2] while the electrostatic force in the $-z$ direction due to the ambipolar electric field is simply $F_E = qE$, where E is the magnitude of the ambipolar electric field in the $-z$ direction.

$$F_B = \frac{1}{2}\frac{mv_\perp^2}{B}\left|\frac{\partial B}{\partial z}\right| \tag{7.1}$$

where $v_\perp$ is the electron velocity perpendicular to the magnetic field lines and B is the magnetic field strength. By setting $v_\perp = v_{th}$ where v_{th} is the thermal velocity of electrons, the maximum mirror force on axis can be found for the case where $I_{sol} = 40$ A and is $F_B \sim 3.7 \times 10^{-18}$ N in the $+z$ direction. The measured potential profile indicates an increase of 7 V from antenna to solenoids for the $z_B = -30$ cm case. This represents an average electric field of 23 V/m and the average force on an electron is $F_E \sim 3.7 \times 10^{-18}$ N in the $-z$ direction. Given that $F_E \sim F_B$, it appears that the ambipolar electric field is set up to balance the maximum magnetic mirror force on the electrons in this case.

For the $z_B = -30$ cm case, the magnitude of the potential variation along the axis is on the order of T_e and the structure would drive ion diffusion away from the solenoids in both axial directions. On the far side of the solenoids from the antenna, the plasma potential decreases to less than 50 V by $z = -65$ cm and would therefore repel electrons. Applying the Boltzmann equation directly to axial profiles here is difficult given that there is probably local ionisation occurring between the antenna and solenoids, however the close coincidence of the maximum density and potential appears to be acting in a Boltzmann-like way. Figure 7.1 also shows the axial plasma potential profile for the $z_B = -60$ cm case, i.e. a case which is seen to operate in the regime with two density peaks. Again, the potential profile is peaked under the solenoids, showing a maximum potential of $\sim$ 100 V which decreases axially to about 75 V near the RF antenna. Interestingly, the maximum plasma potential aligns with the density peak located under the solenoids meaning that the Boltzmann relation appears to apply in the solenoid region but not close to the antenna. Further investigation of the particle transport in this second operating regime will be conducted in future studies and the rest of this chapter will focus on the high density regime and why there is a regime transition.

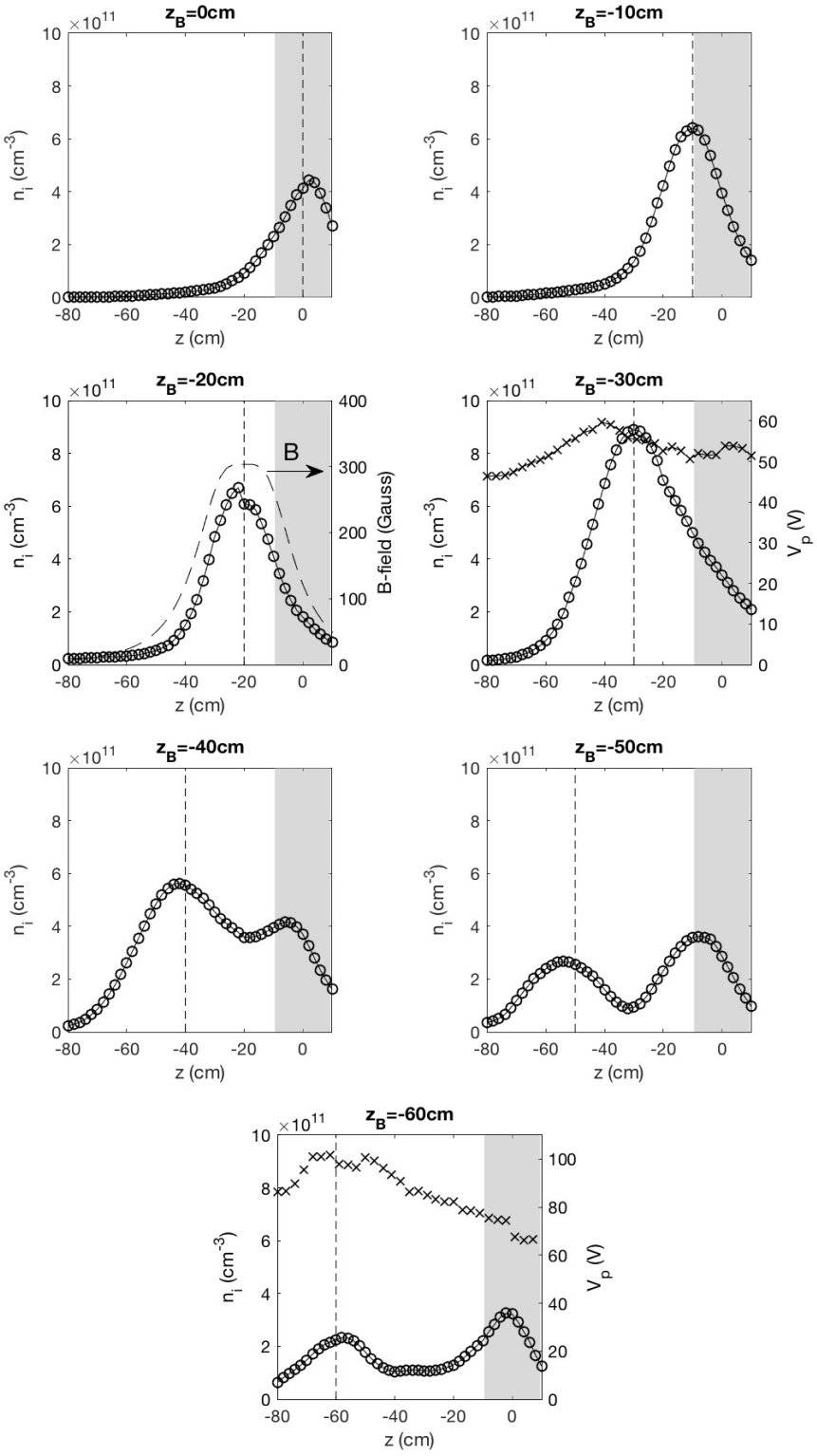

Figure 7.1: Axial density profiles as measured by the LP on axis for different values of z_B and experimental conditions of 1 mTorr, 200W RF power and $I_{sol} = 40$ A. Axial V_p profiles measured by the EP are shown as crosses in the $z_B = -30$ cm and $z_B = -60$ cm cases. The region directly under the RF antenna is shaded grey and the location of z_B is indicated by the vertical dashed line.

7.3 Radial measurements

To further investigate the behaviour of the $z_B = -30$ cm case, the LP and CP are used to measure the radial profiles of n_i, T_e and V_p at $z = z_B$ in radial increments of 0.5 cm. The radial data for $z = z_B = -30$ cm (triangles) is compared with the equivalent data taken for the $z = z_B = 0$ cm case (circles) in figure 7.2. The vertical dashed line shown in figure 7.2 corresponds to the radial position of the most radial magnetic field line that intersects with the closest end of the antenna region for the $z = z_B = -30$ cm case and has no particular significance when considering the $z_B = 0$ cm data. In figure 7.2a, the density data at $r = 0$ cm shows the same increase in axial density that was seen when moving the solenoids from $z_B = 0$ cm to $z_B = -30$ cm in figure 7.1. In the $z_B = 0$ cm case, the density decreases radially from 4.2×10^{11} cm^{-3} on axis to 2.7×10^{11} cm^{-3} at $r = 4$ cm, a reduction of 35%. In the $z_B = -30$ cm case, the density is also seen to be lower at the wall, however there is a distinct peak off-axis at approximately the same radial location as the most radial magnetic field line to intersect with the antenna. This density peak at $r \sim 3$ cm has approximately the same magnitude as that on axis, $\sim 8.5 \times 10^{11}$ cm^{-3}. It is unclear what creates this off-axis density peak, however it could be related to the radial potential profiles discussed below.

Figure 7.2b shows the radial values of T_e measured by the CP for both positions of the solenoids. The EEPFs measured in this study were characterised by single-temperature Maxwellian distributions, consistent with those observed in a similar device in [79]. The profiles show similar electron temperatures of about 5 eV on axis, most likely because the pressure is unchanged. For the $z_B = 0$ cm case, the electron temperature peaks off axis with an increase in T_e of about 1.5 eV, centred around approximately $r = 2.5$ cm. For a density of $\sim 3 \times 10^{11}$ cm^{-3} here, the radial RF skin depth, calculated using equation 5.1 is approximately 1 cm. The increase in T_e radially could therefore be due to the RF power being more effectively absorbed by the plasma within the first few skin depths from the radial wall. The electrons here are highly magnetised and would not be able to diffuse inwards to the centre, meaning that they would not thermalise across the magnetic field lines. For the $z_B = -30$ cm case, the radial T_e demonstrates different behaviour and drops by more than a factor of 2 from the centre to the edge. The decrease in T_e from 5 eV to 2 eV occurs at approximately the same radial position as the most radial magnetic field line to intersect the antenna region. The CP was also used to measure the electron temperature at $z = 0$ cm, $r = 0$ cm in the $z_B = -30$ cm case and the electron temperature was also found to be 5 eV. Therefore, the electrons heated by the RF antenna appear to be funnelled axially through the experiment to the region of high magnetic field strength along the magnetic field lines that pass through the antenna region. These heated electrons would be accelerated by the DC ambipolar field

discussed earlier and plotted in figure 7.1 for the $z_B = -30$ cm case. Radially outside the magnetic field lines that pass through the antenna, a colder electron population is present because these cannot access the RF heating region.

Figure 7.2c shows the radial profiles of V_p measured by the CP for the two values of z_B considered here. In both cases, the radial potential profile is of similar magnitude (~ 60 V) and is remarkably flat, showing that there are no large radial electric fields under the solenoid. The inset in figure 7.2c shows the same data zoomed in showing that there is actually some structure in these profiles and that small radial electric fields are generated. In the $z_B = 0$ cm case, the potential profile is centrally peaked, decreasing from an axial value of 61 V to 56 V at $r = 4$ cm. Again, this potential structure is on the order of T_e and would serve to eject ions radially from the plasma. In the $z_B = -30$ cm case, the profile is reversed with a maximum V_p of 59.5 V found at $r = 4$ cm and a minimum of 56 V on axis. Such a structure would act to radially confine ions in the plasma, even if only by a potential of 4 V. The figure also shows a local V_p maximum at $r = 1.5$ cm and a local minimum at $r = 3$ cm. For the region $r < 1.5$ cm, ions would be accelerated to the centre by this radial potential structure while electrons would be pushed towards the local maximum at $r = 1.5$ cm, however the cross-field transport of these magnetised electrons is expected to be minimal. For $r > 1.5$ cm, the structure would trap ions in the potential well at $r = 3$ cm while electrons would either be accelerated to $r = 1.5$ cm or the radial wall. The potential well could explain why there is an off-axis density peak at a similar radial location in the $z_B = -30$ cm data in figure 7.2a. The potential well itself could be a result of the radial drop in electron temperature which would cause a radial electron pressure gradient straddling the most radial field line to pass through the antenna region. It should be noted, however, that the variations in the radial potential profiles are very small when compared to the total magnitude of the measured V_p.

In figure 7.2c, the radial profiles are very flat, indicating that there is probably significant charging of the radial wall. This is true even where the electron temperature decreases suggesting that the floating potential, V_f, changes such that the relation $V_p - V_f \sim 5kT_e$, where k is the Boltzmann constant, remains true for constant V_p. Indeed, measurements of the floating potential taken with the LP (not shown here) demonstrate a minimum in the centre and increase towards the walls, similar to those shown previously [79].

The results presented here provide valuable insight into how the plasma is formed under the solenoids. The radial profiles of T_e indicate that only electrons from the area defined by the magnetic field lines that pass through the antenna region will contribute significantly to local ionisation at the distant solenoid. The velocity of these electrons would mostly be parallel to the magnetic field lines due to the axial potential profile which peaks near the solenoids. As

the electrons heated under the antenna flow towards the solenoids, the converging magnetic field geometry increases their density due to the geometry of the most radial field line which intersects the antenna. Given that this field line is located at $r = -2.5$ cm for $z = z_B = -30$ cm and the inner radius of the glass tube is 4.5 cm, the column of electrons transported to the solenoids would decrease in area by a factor of $4.5^2/2.5^2 \sim 3.2$. Hence, the density would be expected to increase by this ratio. Examining the axial density profile for the $z_B = -30$ cm case in figure 7.1 and comparing the density at $z = -30$ cm to that at $z = 0$ cm yields an axial increase by a factor of about 2.7, similar to that expected from the magnetic field topology.

Under the solenoids, the mean free path for ion-neutral charge exchange collisions, $\lambda_i \sim 2.5$ cm, is larger than the ion Larmor radius for ions with a thermal velocity of 400 m/s, $r_{Li} \sim 0.5$ cm, meaning that an ion will, on average, collide each time that it completes an orbit around a field line. Given that the radial plasma potential is flat and the radial density profile does not follow the radial T_e profile, it suggests that the gyro radius and collisions are determining the radial ion dynamics.

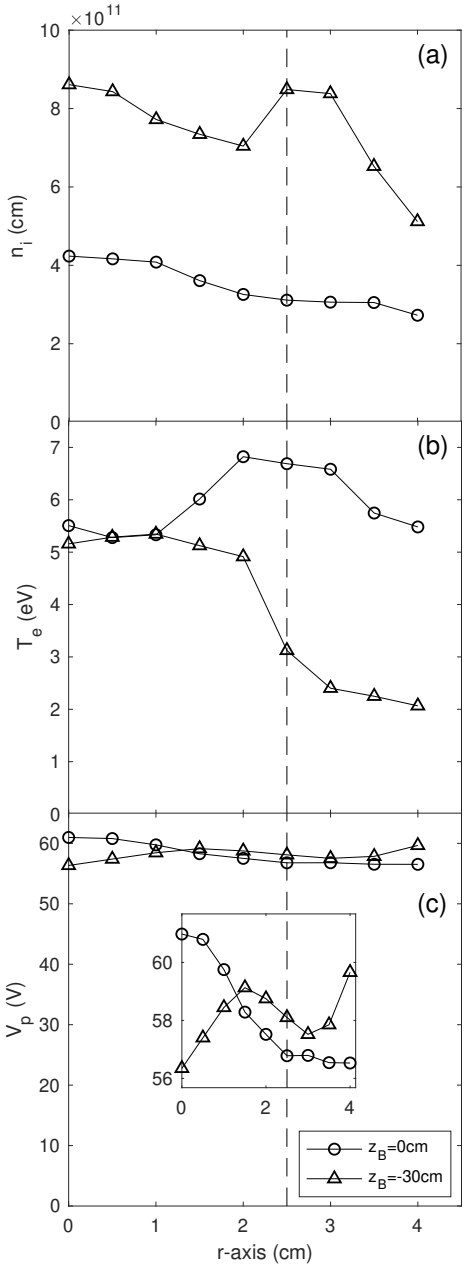

Figure 7.2: Radial measurements under the solenoids (i.e. $z = z_B$) for $z_B = 0$ cm (circles) and $z_B = -30$ cm (triangles). (a) The ion density, n_i, measured using the LP. (b) Shows the electron temperature, T_e, measured by the CP using the first-derivative method. (c) Shows the plasma potential, V_p, as determined by the minimum of the first derivative of the CP data. The inset shows the same radial V_p data but is zoomed in on the y-axis, allowing for the smaller scale structure to be seen. The dashed vertical line is the position of the most radial magnetic field line that passes through the antenna region for the $z_B = -30$ cm case.

7.4 Relation to power and pressure

Now that the behaviour of the $z_B = -30$ cm case has been established relative to the $z_B = 0$ cm case, the factors that determine the value of z_B at which there is a regime change can be investigated, as discussed earlier in relation to the axial density profiles. The results presented in figure 7.1 and figure 7.2 showed that prior to this regime change, the density was a maximum on axis due to the radial contraction of the plasma column through which electrons are transported to the region of high magnetic field. For $|z_B| > 30$ cm, this electron transport is not as efficient and results in the two regions of density seen earlier. To identify why this might be, the dependence of the plasma behaviour on RF power and pressure were investigated by increasing the power to 500 W and varying the pressure over an order of magnitude from 0.5 to 5 mTorr.

Figure 7.3 shows the axial density profiles when z_B is moved from 0 cm to -60 cm, measured with the LP during experiments run with pressures of 0.5, 1 and 5 mTorr, an RF power of 500 W and a solenoid current of 40 A. With an increase in power from 200 W to 500 W, the peak density on axis in the 1 mTorr, $z_B = -30$ cm case has increased to over 10^{12} cm^{-3} and a blue core (argon ion emission lines) can be seen under the solenoids. In a similar manner to that discussed in the last section, the density profiles exhibit a single peak under the solenoids for positions of $|z_B| < 30$ cm. When the separation between the solenoids and antenna is increased, the same transition from a singly peaked density profile to a doubly peaked profile is observed. This indicates that this behaviour is independent of the RF power in this range. Higher RF powers were not explored because the experiments were run in a continuous mode and higher density plasmas would probably damage the probes used. Future experiments operated in a pulsed mode could be done to explore if this trend holds for higher powers, e.g. in the kW range.

The existence of a high density plasma and a blue core is commonly associated with the propagation of helicon waves in similar RF plasmas. To investigate whether this is the case in Echidna, a B-dot probe following the construction described in [28] and oriented to measured RF magnetic field oscillations in the radial direction, was swept along the central axis where the maximum B_r would be expected for a propagating m=1 helicon wave mode. Disappointingly, no helicon wave fields were detected under any of the experimental conditions discussed in this study. Furthermore, no resonances in the system were observed as the solenoids were separated from the RF antenna and the magnetic field strength at $z = 0$ cm approached values where doppler shifted cyclotron resonance heating of electrons perpendicular to the field lines has been observed previously [146]. Therefore, it appears that wave related heating

effects are negligible under the current experimental conditions.

As well as being invariant to changes in RF power (i.e. comparison between the 1 mTorr case in figure 7.3 and the results in figure 7.1), the axial density behaviour shown in figure 7.3 appears to be invariant under changes in argon pressure. Figure 7.3 shows that for increasing separation of the solenoids and antenna, the axial profiles show a maximum density in the $z_B = -30$ cm case for all pressures. Here, measured T_e values of 6.4 and 3.3 eV were used for the 0.5 mTorr and 5 mTorr cases, respectively, when calculating the density. The axial behaviour for different values of z_B can be described in the same way as previously, i.e. single peak for $|z_B| < 30$ cm and double peak with decreasing density for $|z_B| > 30$. This implies that the mean free path for collisions of any type is not the determining factor for the critical value of z_B which determines the regime change. It should be noted however that for the $z_B = -50, -60$ cm cases at 5 mTorr, the density peak at $z = z_B$ is very low compared to that at 0.5 mTorr, suggesting that the plasma ionisation far from the antenna is inhibited at high pressures. Therefore, it seems that the remote ionisation occurring under the solenoid for large values of $|z_B|$ is dependent on the pressure as the mean free path of collisions decreases and electrons can't be transported as efficiently to the solenoids.

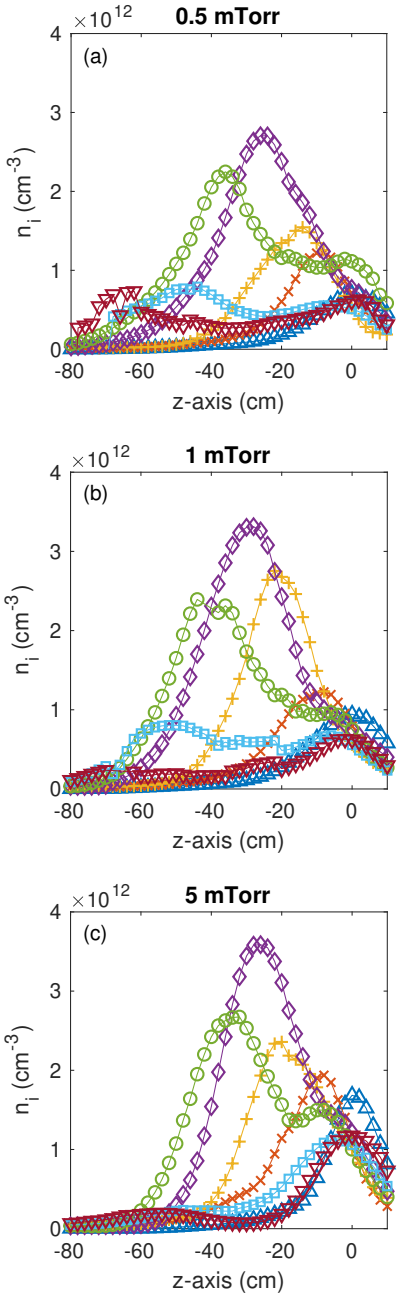

Figure 7.3: Axial plasma density profiles measured by the LP for experimental conditions of 500 W RF power, $I_{sol} = 40$ A and argon pressures of (a) 0.5 mTorr, (b) 1 mTorr, (c) 5 mTorr. The solenoids were positioned at locations of $z_B = 0$ cm (blue upward pointing triangles), $z_B = -10$ cm (orange crosses), $z_B = -20$ cm (yellow plus signs), $z_B = -30$ cm (purple diamonds), $z_B = -40$ cm (green circles), $z_B = -50$ cm (light blue squares), $z_B = -60$ cm (dark red downward pointing triangles).

7.5 Magnetic field dependence

The experiments presented thus far have been conducted with a constant magnetic field and the containment of electrons and ions in the plasma would therefore have been the same (apart from some variations in the electron temperature with different pressures). It is important to look at how the magnetisation of the plasma changes throughout the system as the solenoids are progressively separated from the antenna. For a 5 eV electron population, the thermal velocity is 9.4×10^5 m/s. For the field strengths discussed in this study, the electron Larmor radius is less than 1 mm near the solenoids and only becomes comparable to the radius of the tube over a meter from z_B. The ion Larmor radius, however, is much more comparable to the Echidna tube radius and it is instructive to investigate the effect of ion magnetisation.

Figure 7.4 shows the ion Lamor radius at the centre of the antenna, $z = 0$ cm, as the solenoids are progressively moved away, i.e. as $z_B \to -60$ cm. When the solenoids are supplied with a current of 40 A (solid line), the figure shows that the Larmor radius is less than the radius of the glass tube (dotted horizontal line) for $|z_B| < 34$ cm. For $|z_B| > 34$ cm, the Larmor radius increases rapidly as the magnitude of the magnetic field strength decreases far from the solenoids. Interestingly, this value of z_B where the ion Larmor radius exceeds the glass tube radius at $z = 0$ cm is close to the value which results in the largest density on axis in figure 7.1. It is possible that ion magnetisation under the antenna determines which of the regimes discussed earlier will be observed in the axial density profiles. To test this hypothesis, the expected ion Larmor radius for stronger and weaker magnetic fields can be calculated and the cases where $I_{sol} = 20$ A and 80 A are plotted in figure 7.4. For $I_{sol} = 20$ A, the Larmor radius is doubled as the magnetic field strength is halved and the figure shows that the r_{Li} exceeds the glass tube radius at $z_B \sim 26$ cm. Similarly, for the $I_{sol} = 80$ A case, the magnetic field strength is double that of the 40 A case, halving r_{Li} and causing the point where it exceeds the tube radius to move away from the antenna to $z_B \sim 44$ cm. Given that the regime change found earlier in the $I_{sol} = 40$ A case occurred when z_B moved from -30 cm to -40 cm, a similar regime change might be observed in the $I_{sol} = 20$ A and 80 A cases when z_B moves from $z_B = -20$ cm to -30 cm and $z_B = -40$ cm to -50 cm, respectively, if ion magnetisation in the antenna region is responsible for this behaviour.

To test this, the experiments which produced the axial density profiles in figure 7.1 were repeated with solenoid currents of 20 A and 80 A. Only the density profiles for values of z_B near that which would cause r_{Li} to exceed the glass tube radius at $z = 0$ cm are plotted in figure 7.5 for clarity. The $I_{sol} = 20$ A case is shown in figure 7.5a for z_B values of -20, -30, -40 cm. When $z_B = -20$ cm and the ions are magnetised under the antenna, the axial

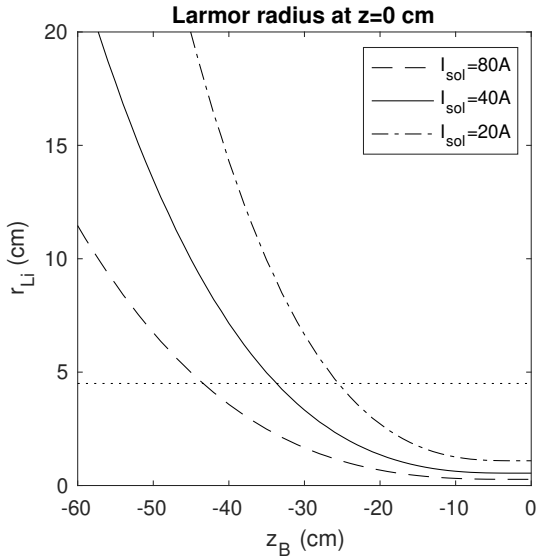

Figure 7.4: The Larmor radius of ions at $z = 0$ cm for an ion thermal velocity of 400 m/s due to the solenoidal field at z_B powered by currents of 20 A (dash-dotted line), 40 A (solid line) and 80 A (dashed line). The inner radius of the Echidna chamber is depicted by the horizontal dotted line at $r = 4.5$ cm.

density exhibits a singly peaked profile, however when z_B moves to -30 cm, and r_{Li} exceeds the tube radius, the profile shows two peaks. The density of these peaks are comparable to the $z_B = -20$ cm case, however when z_B moves even further from the antenna, the density under the solenoid decreases by a factor of ~ 2. Given that r_{Li} at $z = 0$ cm is expected to exceed the glass tube radius at $z_B \sim 26$ cm, the similarity between the densities in the $z_B = -20$ cm and $z_B = -30$ cm cases is not entirely surprising given that the transition from magnetised to unmagnetised ions might still be occurring. By $z_B = -40$ cm, the transition has occurred and the operating regime has well and truly changed from a singly peaked to doubly peaked density profile.

For the $I_{sol} = 80$ A case shown in figure 7.5b, only the results for z_B values of $-30, -40, -50$ cm are plotted. The critical value of z_B which results in the ion Larmor radius exceeding the tube radius was $z_B \sim 44$ cm. Therefore, ions are still magnetised under the antenna in the $z_B = -30$ and -40 cm cases. The axial density profiles displayed in figure 7.5b for these cases are singly peaked and the regime transition with increasing separation between antenna and solenoid has not yet occurred. When the solenoids are moved to $z_B = -50$ cm, the density profile is doubly peaked and has reduced in density nearly by a factor of 2, again aligning with the position of z_B where the ions become unmagnetised under the antenna, i.e. $z_B = -44$ cm for $I_{sol} = 80\ A$.

The calculations of r_{Li} used a constant thermal velocity of 400 m/s across all magnetic field strengths. It is unlikely that this is a constant over all experimental conditions and probably varies spatially, however the first order analysis of ion magnetisation here appears to describe the remote coupling regimes well.

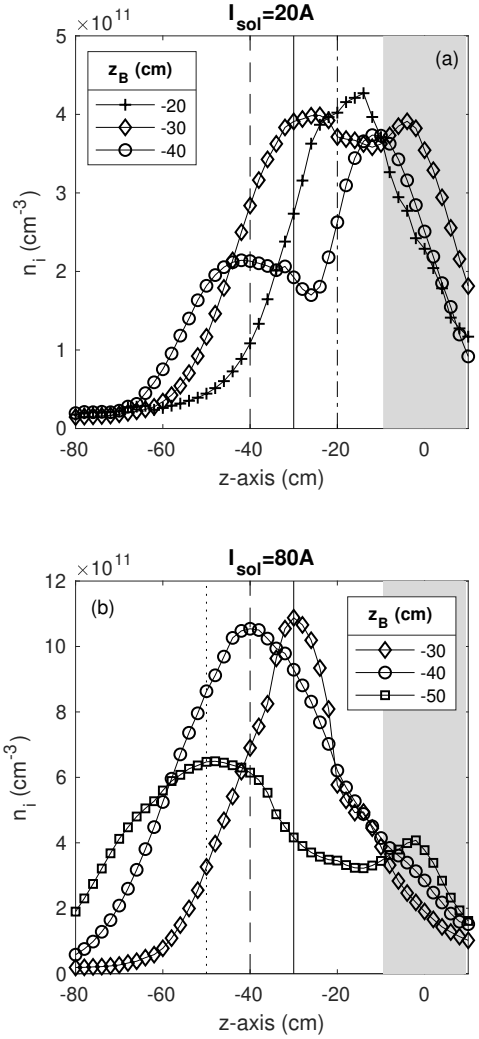

Figure 7.5: Axial density measurements for different values of z_B and experimental conditions of 1 mTorr, 200W RF power and solenoid currents of (a) $I_{sol} = 20$ A and (b) $I_{sol} = 80$ A. The region directly under the RF antenna is shaded grey and the solenoid location is indicated by the vertical lines for $z_B = -20$ cm (dash-dotted), $z_B = -30$ cm (solid), $z_B = -40$ cm (dashed) and $z_B = -50$ cm (dotted).

7.6 Discussion

The results and observations discussed above support the hypothesis that the operating regime changes based on the degree of ion magnetisation under the antenna. When ions are magnetised, the plasma supports efficient transport of electrons from the heating region under the RF antenna to the region of high magnetic field strength. Ions themselves are not transported to the region of high magnetic field strength because the mean free path for ion-neutral charge exchange collisions is ~ 2.5 cm which is much smaller than the order of z_B. The electrons have a much larger mean free path for electron-neutral and ionising collisions and are transported along a column defined by the magnetic field lines which pass through the antenna region. As these magnetic field lines feature a converging geometry, the column decreases in radius, thereby increasing the density of electrons on axis. Significant charging of the radial walls enables a flat radial potential structure: the radial density profile under the solenoids does not follow the radial T_e profile which implies that collisions and ion gyrokinetic properties are responsible for these radial density profiles. These results appear to be independent of the argon gas pressure and RF power.

The radial walls of Echidna are an insulating glass tube and can therefore be anisotropically charged, dependent on the local equilibrium flux ratio of positive and negative particles incident on the wall. If the walls were grounded and conducting, the floating potential of the walls would be forced to be 0 V everywhere. In this particular instance in a magnetised plasma, the relationship $V_p - V_f \sim 5kT_e$ remains essentially correct, however the absolute value of V_f is not forced to be 0 V. As electrons are more highly magnetised than ions and have longer mean free paths for elastic and inelastic collisions, the potential of the radial wall will be determined by considering the local ion flux arriving from the bulk of the local plasma and the non-local electron flux along the magnetic field line intersecting the wall at that location. With the solenoidal magnetic field sufficiently distant, the plasma ions under the antenna are unmagnetised and can easily drift towards the radial wall, increasing the ion flux to the radial wall under the antenna compared to the magnetised case. The build-up of positive charge on the wall attracts electrons in order to balance the flux of positive and negative charges. This would alter the cross-field electron transport locally and impact the equilibrium conditions of the non-local electron population streaming along the magnetic field lines that intersect the antenna region. Therefore, when ions become less magnetised, the equilibrium conditions of the electron populations restricted to field lines passing through the antenna region would change. Given that these electrons are those that are heated near the antenna and transported to the region of high magnetic field, it is very likely that ion magnetisation and wall charging under the antenna play a significant role in the creation of

a high density, remotely ionised plasma under the solenoids, possibly explaining the shift in operating regime.

These results open a range of interesting avenues for future research in Echidna and similar reactors. Firstly, if ion magnetisation is responsible for the observed behaviour, then an investigation with different gases could be conducted. For gases with much higher atomic/molecular weight, the ion Larmor radius is much larger due to the increased inertia and would exceed the glass tube radius for smaller distances between the solenoids and antenna. For much lighter gases, however, the Larmor radius would be smaller, meaning that the remote ionisation seen in this study could be achieved for much larger distances between the antenna and solenoids for the same magnetic field. Experiments of this kind could be conducted with xenon and helium as high and low mass gases, respectively.

An additional way to test the dependence on the magnetic field would be to study plasmas in Echidna under different magnetic field strengths and solenoid configurations. Figure 7.4 showed that the ion Larmor radius rapidly increases away from the solenoids and r_{Li} under the antenna is about 11.5 cm for $z_B = -60$ cm in the $I_{sol} = 80$ A case, i.e. much larger than the glass tube. With the solenoids currently installed on Echidna, the solenoid current would have to be about 200 A to bring the ion Larmor radius at $z = 0$ cm inside the glass tube when the solenoids are positioned at $z_B = -60$ cm. This would result in a maximum magnetic field > 1.5 kG, which is not currently possible with the DC power supply used and would overheat the solenoid coils quite quickly. Alternatively, more solenoids could be mounted on the experiment, allowing for an axially longer region of high magnetic field, potentially stretching the remotely ionised plasma.

One of the more curious results presented in this study is that the density appears to increase along the increasing magnetic field despite the large magnetic mirror ratio on axis. The results showed that the plasma potential was maximum at the solenoids when there was strong remote coupling. As briefly discussed earlier, the acceleration of electrons towards this maximum negates the magnetic mirror effect by effectively increasing the loss angle of the magnetic mirror. These dynamics are understandable in the DC operation of Echidna, however it remains to be seen how this axial potential structure is initiated. When no plasma is present there would be no accelerating potential driving electrons towards z_B and the magnetic mirror would reflect incident particles. The plasma observed under the solenoids is due to local ionisation and excitation as the lifetime of the excited atomic states is less than microseconds. It seems that hot electrons are transported along the field lines from the antenna region but they are additionally energised by an axial electric field that appears to approximately obey the Boltzman equation and negate the magnetic mirror. How this

potential structure is formed and how it is supported is unclear and leads to a severe "chicken and egg" problem. Therefore, a study of the plasma breakdown is necessary to understand how this system works. It is predicted here that the significant anisotropic charging of the dielectric radial walls could be responsible for setting up this DC potential structure, allowing electrons to initially overcome the magnetic mirror.

7.7 Chapter summary

In this chapter, axial plasma density measurements taken in the Echidna plasma reactor were reported for cases when the regions of high magnetic field and radio-frequency heating are progressively separated using a movable solenoid pair. The results show that the operating regime in Echidna changes based on the degree of ion magnetisation under the antenna. When ions are magnetised, electrons heated under the antenna are efficiently transported to the solenoids along a column defined by the magnetic field lines which connect to the antenna region. The cross-section of this column decreases due to the converging magnetic field geometry, thereby increasing the density of electrons on axis. This results in a density profile which is singly peaked and centred on the location of maximum magnetic field strength. When the ions are unmagnetised under the antenna, the flux of positive charges to the wall there is increased. Transport of electrons streaming along field lines that intersect the radial wall in the antenna region towards the antenna region is enhanced to balance this flux. This affects the equilibrium conditions along the entire magnetic field line and results in less efficient transport of electrons heated by the antenna to the region of high magnetic field strength. In this regime there is a global decrease in plasma density and the axial density profile is doubly peaked.

Chapter 8

Summary

8.1 Summary of results

In this thesis, low pressure radiofrequency (RF) argon plasmas interacting with magnetic nozzles have been studied using *in-situ* diagnostic probes across two plasma reactors. These low pressure plasmas are of particular relevance to the electric propulsion community as interest in electrodeless, neutraliser-free plasma thruster has grown over the last few decades. Experiments conducted in the Chi Kung reactor focused on plasmas that are created in the region of high magnetic field strength and expand through the diverging part of the magnetic nozzle. This is an experimental analogy to the helicon double layer thruster in which a plasma is created and expands along the diverging magnetic field into space. In the Echidna reactor, the behaviour of plasmas incident on a converging magnetic field were investigated by progressively separating the solenoidal magnetic field and the RF antenna. The studies in this reactor focused more on the fundamental plasma physics occurring in magnetic nozzles, however some results may be applicable to understanding the dynamics inside electric propulsion devices. An outline of the results can be summarised as follows:

- In chapter 3, the ion beam accelerated by a double layer (DL) or double layer-like potential profile on axis in the Chi Kung reactor was characterised for argon pressures between 0.3 mTorr and 0.7 mTorr using retarding field energy analysers (RFEA) in radial-facing and source-facing configurations. The results showed that the magnitude of the axial potential drop reduced approximately exponentially with increasing pressure while the location of the potential drop moved downstream. This shift downstream was consistent with the measured axial density profiles which showed that the position of the maximum axial density moves downstream and the peak density increases with increasing pressure. The density profiles were calculated from the raw RFEA data using

two methods: the Gaussian-flux method and the drifting Maxwellians method. These two methods demonstrated excellent agreement and validated the use of the Gaussian-flux method for the rest of the thesis.

Measurement of the ion beam velocity was achieved by comparing the data collected using the source-facing and radial-facing RFEAs. With increasing pressure, the downstream ion beam velocity decreased exponentially, results that were consistent with the reduction in the magnitude of the axial potential drop. Previously published measurements of the downstream ion beam velocity in Chi Kung, obtained using an *ex-situ* laser induced fluorescence (LIF) technique, were also consistent with the exponential trend found using the RFEA data. Next, the axial beam velocity profiles were presented and showed that the velocity increased rapidly in the region of the potential drop and plateaued downstream. The axial position at which the beam velocity plateaued also shifted downstream with increasing pressure. Limited data from the previous LIF study was shown to be in quite strong agreement with the data collected using the RFEA, thereby validating the use of the RFEA in the region of ion acceleration and allowing for the density of the beam to be measured. At low pressures, i.e. when the beam velocity is highest, the measurements demonstrated the smallest beam density at the intersection between the plasma source and expansion region. This density increased as the beam density profile shifted downstream with increasing pressure in a manner consistent with the local density and plasma potential profiles. These results helped to explain why previous studies have shown that maximising the total ion density at the outlet of HDLT-type thrusters is crucial to maximising thrust, sacrificing high beam density fraction and velocity in favour of outlet density, n_{tot}. As an example, the measurements presented in chapter 3 showed that, in the 2 mTorr case, there is no beam detected at all but the local density at the outlet is still 3 times higher than the beam density in the 0.7 mTorr case. This means that higher pressure operation of helicon thrusters could provide larger thrusts despite having a reduced beam velocity.

- In chapter 4, the dependence of the DL formation and subsequent ion beam characteristics on the relative locations of the geometric expansion and diverging magnetic field were investigated in Chi Kung. Experiments were conducted for cases when an 18.5 cm long pyrex extension tube was and was not inserted in the expansion chamber. These cases were labelled the extension and standard cases, respectively. The axial density profiles showed a similar axial peak density in both extension and standard cases, but the density gradient in the diverging region of the magnetic nozzle decreased in the extension case. This was consistent with the axial potential profiles which showed a

sharply decreasing potential profile in the standard case and a less severe potential drop in the extension case. The total magnitude of the potential drop also decreased in the extension case and this resulted in a smaller ion beam velocity when compared to the standard case. The axial velocity profiles were measured and were consistent with the profiles expected from the electric field of the potential drop in both cases.

The electron transport throughout Chi Kung was investigated in an attempt to understand why the axial profiles were affected by the addition of the extension tube in these ways. Measurements of the electron energy probability function (EEPF) in the source region showed that the radial electron temperature, T_e, profile was unchanged by the extension tube and was minimum on axis with increasing T_e towards the walls. In the extension case, these off-axis hot electrons cannot access the region where high-density conics normally form off-axis downstream because they are blocked by the extension tube. The magnetic field lines that normally act as the inner and outer radial boundaries of the high-density conics were identified by mapping the ion density in the expansion chamber for the standard case. As the electrons are tightly bound to the field lines, the electrons responsible for ionising the conics must stream along field lines sandwiched between those identified as the inner and outer boundary. The position of these field lines in the source region was found by tracing them back upstream and increased off-axis ionisation in the source region was localised to these positions. As such, it was determined that the extension tube was blocking the transport of these hot off-axis electrons and their residence time in the source region was increased, leading to higher rates of ionisation. The increased plasma density and resulting diffusion throughout the source led to changes in the axial plasma profiles and altered beam characteristics.

The results of this chapter showed that careful attention must be paid to the relative location of the diverging part of the magnetic field and the physical geometric expansion in a helicon thruster. If the transport of those electrons that would normally ionise downstream in the conics is blocked by a physical boundary then these electrons will be trapped in the source region, streaming along their magnetic field line and reflecting off the sheaths that terminate it. Therefore, if maximising the beam velocity in a helicon thruster is desired, the geometric expansion should be designed such that these electron populations can be released to the downstream, allowing for conics formation.

- In chapter 5, the results of chapter 4 were extended by introducing a gap of variable size (denoted as z_{ext}) between the extension tube and source tube. The gap acts as a geometric window allowing for select electron populations to be transported along magnetic field lines that pass through the window to the region where the high-density

conics normally form. The density in the downstream region was mapped for different values of z_{ext} and the results showed how the conics reformed as z_{ext} increases. For $z_{ext} \gtrsim 4$ cm, the conics density and shape were essentially invariant to further increases in z_{ext}. Therefore, the conics were deemed to have essentially completely reformed with a window size of $z_{ext} = 4$ cm. At $z_{ext} = 4$ cm, the measured beam velocity downstream of the axial ion accelerating potential structure showed a step change from the velocity of the extension case to that of the standard case. This indicates that the beam characteristics are somewhat dependent on the nature of electron transport from the plasma source to the conics.

The results discussed in this chapter implied that if the geometric expansion in a helicon thruster could be moved slightly upstream relative to the solenoids, the magnetic field lines that would otherwise impact the source tube wall at axial locations just upstream of the outlet would no longer intersect a physical barrier and electrons travelling along them would reach the region of high density conics. As these electrons would be closer to the antenna than those that can currently escape, it may yield an increase in the conics density and beam velocity. Therefore, care should be taken when designing the source tube of these HDLT-type thrusters, ensuring that the geometric expansion is positioned as far upstream as possible relative to the diverging section of the magnetic field.

- The results of chapters 4 and 5 demonstrated that the field-aligned transport of electrons from source to conics were important for generating a high velocity ion beam on axis. Understanding the nature of this transport is particularly important given that the electron diamagnetic current present downstream of helicon thrusters accounts for one of the major thrust components discussed in the literature [76]. In chapter 6, this transport was investigated in the standard case by measuring the plasma potential and density along the most radial magnetic field line that escapes the source region and intersects the conics. At 0.3 mTorr, a deep and narrow potential structure was measured along the field line where it passes near to the radial wall at the interface between the plasma source and expansion chamber. The potential structure was identified as an electric triple layer (TL) featuring a potential dip approximately 2 times the electron temperature and was shown to agree with the measured density profiles via the Boltzmann relation. The potential dip was also seen at 2 mTorr, however it was much less severe. For electrons created at the location of maximum density, the TL acts as a ~ 40 V potential barrier for electrons travelling from the source to the conics. Those that overcome the potential barrier gain ~ 22 eV of energy as they are accelerated by the other side of the TL into

the conics. Measurements of the break energy in the EEPFs measured upstream and downstream where consistent with these values, thereby supporting the assertion that the TL is present and influencing the field-aligned electron transport as expected.

Radial measurements of the plasma potential and density were presented to determine how far the TL penetrated into the bulk plasma and the sharply decreasing part of the radial potential profile was localised to within ~ 1 cm of the radial wall. A previously published 2-D map of the floating potential throughout the source region measured under similar experimental conditions in the Chi Kung reactor showed increasingly negative floating potentials near to the radial source tube wall [92]. These indicate significantly negative charging of the radial walls and, indeed, measurements of the floating potential discussed in this thesis demonstrated a floating potential of ~ -40 V at the bottom of the triple layer. This build up of negative charges on the insulating source wall repels electrons streaming along the magnetic field line that passes nearby and the plasma potential decreases as a result. The creation of the TL was therefore explained by the proximity of the field line to the negatively charged radial wall.

The most radial magnetic field line escaping the source region in Chi Kung intersects the wall at an oblique angle of 30° and the potential structure could be acting similarly to a magnetic presheath first discussed by Chodura [136]. The possibility of the spatial structure of the potential profile measured along the field was related to a magnetic presheath effect was assessed by increasing the magnetic field strength and measuring the field-aligned floating potential and ion saturation current profiles near the TL using a Langmuir probe. Previous theoretical work had determined that the width of the field-aligned magnetic presheath would decrease linearly with increasing magnetic field strength and the measured profiles of the ion saturation current showed that the width of the TL also decreased linearly increasing magnetic field strength. Using the equation derived by Kim et al. [140], the expected width of the magnetic presheath for these experimental conditions was also shown to be similar to the length of the decreasing section of the field-aligned potential structure measured in Chi Kung. While these measurements do not prove that a magnetic presheath is responsible for the observed plasma behaviour, the measurements do exhibit similar properties. It is unclear how the features discussed in chapter 6 would directly affect the design of a thruster but future studies could investigate the existence and/or importance of magnetic presheaths in helicon reactors generally as almost all of the magnetic field lines generated by solenoidal will intersect a chamber wall at an oblique angle.

- An exploratory study conducted in the newly built Echidna reactor was presented in

chapter 7 and focused on the behaviour of a low pressure argon plasma interacting with an increasingly remote solenoidal magnetic field. Axial plasma density profiles were presented for cases in which the centre of the solenoids was progressively shifted away from the RF antenna in increments of 10 cm. Two modes of operation were identified from these profiles: when the centre of the solenoids was positioned within 30 cm of the RF antenna, the density profiles were singly peaked, the peak was centred on the centre of the solenoids and the peak density increased as the solenoids were moved away. When the separation between the solenoids and the RF antenna was greater than 40 cm, the operating regime changed and the density profile became doubly peaked with one peak centred on the solenoids and the other localised to the RF heating region. In this regime, increases in the separation between the solenoids and RF antenna resulted in global decreases in the plasma density.

In the first operating regime, radial profiles of the plasma density, electron temperature and plasma potential were taken at the axial location directly under the centre of the solenoids for cases when the solenoids and RF antenna were colocated and when they were separated by 30 cm, i.e. the case which demonstrated maximum density on axis. In the colocated case, the density was centrally peaked but only reduced by $\sim 25\%$ off-axis. For the separated case, the density was centrally peaked but also exhibited an increase in density off-axis centred around the most radial magnetic field line that passes through the antenna region. The electron temperature in the separated case was shown to decrease by about 50% outside of these field lines, implying that the electrons are heated by the antenna and then transported up the magnetic field to the solenoid region. The cross-section of the column along which these electrons are transported shrinks, thereby increasing their density and resulting in higher ionisation. The axial plasma potential profile in this case was also peaked in the vicinity of the solenoids and the system appears to behave in a Boltzmann-like manner.

As the solenoids are further separated from the RF heating region, the system enters the second operating regime. The cause of the transition between these regimes was investigated by varying the RF power, argon gas pressure and magnetic field strength. The separation between the solenoids and RF heating region at which the operating regime changes was observed to be independent of both RF power and pressure. For stronger magnetic fields, this critical separation was seen to increase while it decreased for weaker field strengths. The critical separation appeared to be related to the ion Larmor radius underneath the RF antenna. When the solenoids are moved further away from the RF antenna, the ion Larmor radius increases and eventually exceeds

the Pyrex tube radius. As the walls are insulating, they will charge to some floating potential dependent on the relative fluxes of positive and negative charges. When ions are unmagnetised, the flux of positive charges to the wall increases and will affect the equilibrium condition of the electron populations which are bound to magnetic field lines that intersect the wall here. These electrons were identified to be those that are heated by the RF antenna and transported to the solenoids region and the changes to their equilibrium conditions were deemed to be the reason for the less efficient electron transport in the second regime.

Of the results presented in chapter 7, probably the most relevant to thruster applications is the generation of a high density plasma in a magnetic nozzle using relatively low RF powers. Previous studies on helicon thrusters showed that a magnetic field configuration consisting of a single solenoid positioned slightly downstream of the RF antenna resulted in a larger thrust than the same thruster operated with a Helmholtz pair solenoid configuration centred on the antenna [76]. Given the similarity between the Echidna device and the single-solenoid thruster, it is possible that antenna-solenoid configurations like those presented in chapter 7 could yield even further improved thrust characteristics. If a thruster was designed based on these results, it could be done so with an antenna positioned upstream of a solenoid providing a sufficiently strong magnetic field such that the ions are magnetised under the antenna.

While these results might have applications in the electric propulsion community, the novel nature of the Echidna reactor means that there are many other avenues for future research. To continue and further validate the work presented in this thesis, future experiments could focus on particle transport when ions are unmagnetised under the antenna. In this regime, the axial density profiles featured peaks located underneath the solenoids and the RF antenna yet the maximum axial plasma potential profile was found underneath the solenoids. Investigating how this plasma potential profile is created and what supports it could uncover important information about the operation of RF plasma sources operating in nonuniform magnetic fields. To do this, experiments could use pulsed plasmas to study plasma breakdown and wall charging. Furthermore, the hypothesis that ion magnetisation in the antenna region determines the operating regime of the reactor could be tested by using gases with different atomic weights. This would cause the mass term in the Larmor radius equation to change and therefore affect the ion magnetisation throughout the reactor. These future studies would give further insights into the nature of plasma generation in the presence of non-uniform magnetic fields like those inherent to helicon thrusters.

In this thesis, the plasmas in the Echidna reactor were only created using a very narrow set of experimental conditions. Future studies could also investigate entirely different experimental conditions. By exploring a wider range of RF powers, the RF coupling regime could be investigated more thoroughly for different magnetic field configurations. At high powers and magnetic field strengths, this could result in helicon wave coupling, allowing for studies of wave propagation in these nonuniform magnetic fields. Furthermore, experiments could be run under different magnetic field configurations where the spacing between solenoids is varied or more solenoids are installed.

Bibliography

[1] R. V. Lovelace. 'Dynamo model of double radio sources'. *Nature* 262.5570 (1976), pp. 649–652. ISSN: 00280836. DOI: 10.1038/262649a0.

[2] F. F. Chen. *Introduction to plasma physics and controlled fusion*. New York, 1984. DOI: 10.1007/978-1-4757-5595-4.

[3] M. A. Lieberman and A. J. Lichtenberg. *Principles of Plasma Discharges and Materials Processing: Second Edition*. 1994. DOI: 10.1002/0471724254.

[4] D. B. Graves. 'Plasma processing in microelectronics manufacturing'. *AIChE Journal* 35.1 (1989), pp. 1–29. ISSN: 15475905. DOI: 10.1002/aic.690350102.

[5] D. M. Goebel and I. Katz. *Fundamentals of Electric Propulsion: Ion and Hall Thrusters*. 2008. DOI: 10.1002/9780470436448.

[6] M. J. L. Turner. *Rocket and spacecraft propulsion: principles, practice and new developments*. 2008. DOI: 10.1007/978-3-540-69203-4.

[7] C. Charles. 'Plasmas for spacecraft propulsion'. *Journal of Physics D: Applied Physics* 42.16 (2009), p. 163001. ISSN: 0022-3727. DOI: 10.1088/0022-3727/42/16/163001.

[8] J Black. *Lectures on the Elements of Chemistry: Delivered in the University of Edinburgh*. Ed. by J Robinson. vol. 1. Mathew Carey, 1803. URL: https://books.google.com.au/books?id=lqI9AQAAMAAJ.

[9] P. Chabert and N. Braithwaite. *Physics of radio-frequency plasmas*. 2011. DOI: 10.1017/CBO9780511974342.

[10] D Bohm. 'The Characteristics of Electrical Discharges in Magnetic Fields'. *Qualitative Description of the Arc Plasma in a Magnetic Field*. McGraw-Hill: New York, 1949. URL: https://ci.nii.ac.jp/naid/10018428953/en/.

[11] D. J. Griffiths. *Introduction to Electrodynamics*. Pearson international edition. Prentice Hall, 1999. ISBN: 9780139199608.

[12] R. F. Post et al. 'Stable confinement of a high-temperature plasma'. *Physical Review Letters* 4.4 (1960), pp. 166–170. ISSN: 00319007. DOI: 10.1103/PhysRevLett.4.166.

[13] H. B. Smith, C. Charles and R. W. Boswell. 'Breakdown behavior in radio-frequency argon discharges'. *Physics of Plasmas* 10.3 (2003), pp. 875–881. ISSN: 1070664X. DOI: 10.1063/1.1531615.

[14] A. W. Degeling et al. 'Plasma production from helicon waves'. *Phys. Plasmas* 3.7 (1996), p. 2788. ISSN: 1070664X. DOI: 10.1063/1.871712.

[15] V. A. Godyak. 'Statistical heating of electrons at an oscillating plasma boundary'. *Sov. Phys.-Tech. Phys. (Engl. Transl.) 16: No. 7, 1073-6(Jan 1972).* 16 (1972), p. 1073. URL: http://adsabs.harvard.edu/abs/1972SPTP...16.1073G.

[16] M. A. Lieberman. 'Analytical Solution for Capacitive RF Sheath'. *IEEE Transactions on Plasma Science* 16.6 (1988), pp. 638–644. DOI: 10.1109/27.16552.

[17] V. A. Godyak and A. S. Khanneh. 'Ion Bombardment Secondary Electron Maintenance of Steady RF Discharge'. *IEEE Transactions on Plasma Science* PS-14.2 (1986), pp. 112–123. DOI: 10.1109/TPS.1986.4316513.

[18] F. A. Haas, A. Goodyear and N. S. J. Braithwaite. 'Tailoring of electron energy distributions in low temperature plasmas'. *Plasma Sources Science and Technology* 7.4 (1998), pp. 471–477. ISSN: 09630252. DOI: 10.1088/0963-0252/7/4/005.

[19] M. M. Turner and M. A. Liebeirman. 'Hysteresis and the E-to-H transition in radiofrequency inductive discharges'. *Plasma Sources Science and Technology* 8.2 (1999), pp. 313–324. ISSN: 09630252. DOI: 10.1088/0963-0252/8/2/312.

[20] R. W. Boswell and F. F. Chen. 'Helicons-the early years'. *IEEE Transactions on Plasma Science* 25.6 (1997), pp. 1229–1244. ISSN: 00933813. DOI: 10.1109/27.650898.

[21] J. P. Klozenberg, B. Mcnamara and P. C. Thonemann. 'The dispersion and attenuation of helicon waves in a uniform cylindrical plasma'. *Journal of Fluid Mechanics* 21.3 (1965), pp. 545–563. ISSN: 14697645. DOI: 10.1017/S0022112065000320.

[22] R. W. Boswell. 'A study of waves in gaseous plasmas'. PhD thesis. Flinders University of South Australia, 1970.

[23] R. W. Boswell. 'Plasma production using a standing helicon wave'. *Physics Letters A* 33.7 (1970), pp. 457–458. ISSN: 03759601. DOI: 10.1016/0375-9601(70)90606-7.

[24] R. W. Boswell. 'Very efficient plasma generation by whistler waves near the lower hybrid frequency'. *Plasma Phys. Control. Fusion* 26 (1984), p. 1147. DOI: 10.1051/0004-6361:200809946.

[25] F. F. Chen and R. W. Boswell. 'Helicons-the past decade'. *IEEE Transactions on Plasma Science* 25.6 (1997), pp. 1245–1257. ISSN: 00933813. DOI: 10.1109/27.650899.

[26] K. P. Shamrai. 'Volume and surface rf power absorption in a helicon plasma source'. *Plasma Sources Science and Technology* 5.3 (1996), pp. 474–491. DOI: 10.1088/0963-0252/5/3/015.

[27] F. F. Chen and D. D. Blackwell. 'Upper limit to landau damping in helicon discharges'. *Physical Review Letters* 82.13 (1999), pp. 2677–2680. ISSN: 10797114. DOI: 10.1103/PhysRevLett.82.2677.

[28] T. A. Lafleur. 'Helicon Wave Propagation in Low Diverging Magnetic Fields'. PhD thesis. Australian National University, 2011.

[29] L. P. Block. 'A double layer review'. *Astrophysics and Space Science* 55.1 (1978), pp. 59–83. ISSN: 0004640X. DOI: 10.1007/BF00642580.

[30] N. Hershkowitz. 'Review of recent laboratory double layer experiments'. *Space scicence reviews* 41.3-4 (1985), pp. 351–391.

[31] C. Charles. 'A review of recent laboratory double layer'. *Plasma Sources Science and Technology* 16.4 (2007), R1–R25. ISSN: 0963-0252. DOI: 10.1088/0963-0252/16/4/R01.

[32] H. S. Maciel and J. E. Allen. *Free double layers in mercury-arc discharges*. Vol. 42. 2. Australian National University, 1989, pp. 321–352. ISBN: 0022377800014. DOI: 10.1017/S0022377800014380.

[33] J. S. Levine and F. W. Crawford. 'Langmuir probe measurements of double-layers in a pulsed discharge'. *Journal of Plasma Physics* 24.2 (1980), pp. 359–383. ISSN: 14697807. DOI: 10.1017/S002237780002287X.

[34] F. S. Mozer et al. 'Observations of paired electrostatic shocks in the polar magnetosphere'. *Physical Review Letters* 38.6 (1977), pp. 292–295. ISSN: 00319007. DOI: 10.1103/PhysRevLett.38.292.

[35] F. S. Mozer and C. A. Kletzing. 'Direct observation of large, quasi-static, parallel electric fields in the auroral acceleration region'. *Geophysical Research Letters* 25.10 (1998), pp. 1629–1632. DOI: 10.1029/98GL00849.

[36] S. Torven and D. Andersson. 'Observations of electric double layers in a magnetised plasma column'. *Journal of Physics D: Applied Physics* 12.5 (1979), pp. 717–722. ISSN: 00223727. DOI: 10.1088/0022-3727/12/5/012.

[37] N. Sato et al. 'Ultrastrong stationary double layers in a nondischarge magnetoplasma'. *Physical Review Letters* 46.20 (1981), pp. 1330–1333. ISSN: 00319007. DOI: 10.1103/PhysRevLett.46.1330.

[38] P. Coakley et al. 'Experimental observations of strong double layers'. *Physical Review Letters* 40.4 (1978), pp. 230–233. ISSN: 00319007. DOI: 10.1103/PhysRevLett.40.230.

[39] G. Hairapetian and R. L. Stenzel. 'Particle dynamics and current-free double layers in an expanding, collisionless, two-electron-population plasma'. *Physics of Fluids B* 3.4 (1991), pp. 899–914. ISSN: 08998221. DOI: 10.1063/1.859847.

[40] C. Charles and R. Boswell. 'Current-free double-layer formation in a high-density helicon discharge'. *Applied Physics Letters* 82.9 (2003), pp. 1356–1358. ISSN: 00036951. DOI: 10.1063/1.1557319.

[41] S. A. Andersen et al. 'Continuous supersonic plasma wind tunnel'. *Physics Letters A* 27.8 (1968), pp. 527–528. ISSN: 03759601. DOI: 10.1016/0375-9601(68)90901-8.

[42] S. A. Cohen et al. 'Ion acceleration in plasmas emerging from a helicon-heated magnetic-mirror device'. *Physics of Plasmas* 10.6 (2003), pp. 2593–2598. ISSN: 1070664X. DOI: 10.1063/1.1568342.

[43] C. Charles and R. W. Boswell. 'Time development of a current-free double-layer'. *Physics of Plasmas* 11.8 (2004), pp. 3808–3812. ISSN: 1070664X. DOI: 10.1063/1.1764829.

[44] C. Charles. 'Hydrogen ion beam generated by a current-free double layer in a helicon plasma'. *Applied Physics Letters* 84.3 (2004), pp. 332–334. ISSN: 00036951. DOI: 10.1063/1.1643548.

[45] C. Charles and R. W. Boswell. 'Laboratory evidence of supersonic ion beam generated by a current-free "helicon" double-layer'. *Physics of Plasmas* 11.4 (2004), pp. 1706–1714. ISSN: 1070664X. DOI: 10.1063/1.1652058.

[46] C Charles, R. W. Boswell and M. A. Lieberman. 'Xenon ion beam characterization in a helicon double layer thruster'. *Applied Physics Letters* 89.26 (2006), pp. 2004–2007. ISSN: 00036951. DOI: 10.1063/1.2426881.

[47] C. Charles et al. 'An experimental investigation of alternative propellants for the helicon double layer thruster'. *Journal of Physics D: Applied Physics* 41.17 (2008), pp. 3–8. ISSN: 00223727. DOI: 10.1088/0022-3727/41/17/175213.

[48] X. Sun et al. 'Parallel velocity and temperature of argon ions in an expanding, helicon source driven plasma'. *Plasma Sources Science and Technology* 13.3 (2004), pp. 359–370. ISSN: 09630252. DOI: 10.1088/0963-0252/13/3/001.

[49] X. Sun et al. 'Observations of ion-beam formation in a current-free double layer'. *Physical Review Letters* 95.2 (2005), pp. 1–4. ISSN: 00319007. DOI: 10.1103/PhysRevLett.95.025004.

[50] A. M. Keesee et al. 'The ion velocity distribution function in a current-free double layer'. *Physics of Plasmas* 12.9 (2005), pp. 1–7. ISSN: 1070664X. DOI: 10.1063/1.2033647.

[51] A. Meige et al. 'One-dimensional particle-in-cell simulation of a current-free double layer in an expanding plasma'. *Physics of Plasmas* 12.5 (2005), pp. 1–10. ISSN: 1070664X. DOI: 10.1063/1.1897390.

[52] A. Meige et al. 'One-dimensional simulation of an ion beam generated by a current-free double-layer'. *IEEE Transactions on Plasma Science* 33.2 I (2005), pp. 334–335. ISSN: 00933813. DOI: 10.1109/TPS.2005.844956.

[53] C. Biloiu et al. 'Evolution of the parallel and perpendicular ion velocity distribution functions in pulsed helicon plasma sources obtained by time resolved laser induced fluorescence'. *Plasma Sources Science and Technology* 14.4 (2005), pp. 766–776. ISSN: 0963-0252. DOI: 10.1088/0963-0252/14/4/016.

[54] O. Sutherland et al. 'Experimental evidence of a double layer in a large volume helicon reactor'. *Physical Review Letters* 95.20 (2005), pp. 1–4. ISSN: 00319007. DOI: 10.1103/PhysRevLett.95.205002.

[55] N. Plihon, P. Chabert and C. S. Corr. 'Experimental investigation of double layers in expanding plasmas'. *Physics of Plasmas* 14.1 (2007). ISSN: 1070664X. DOI: 10.1063/1.2424429.

[56] K Takahashi and T Fujiwara. 'Observation of weakly and strongly diverging ion beams in a magnetically expanding plasma'. *Applied Physics Letters* 94.6 (2009), p. 061502. ISSN: 00036951. DOI: 10.1063/1.3080205.

[57] Å Fredriksen, L. N. Mishra and H. S. Byhring. 'The effects of downstream magnetic field on current-free double layers and beam formation in the Njord helicon plasma device'. *Plasma Sources Science and Technology* 19.3 (2010), p. 034009. ISSN: 0963-0252. DOI: 10.1088/0963-0252/19/3/034009.

[58] M. Wiebold, Y. T. Sung and J. E. Scharer. 'Experimental observation of ion beams in the Madison Helicon eXperiment'. *Physics of Plasmas* 18.6 (2011). ISSN: 1070664X. DOI: 10.1063/1.3596537.

[59] S. K. Saha et al. 'Two-dimensional double layer in plasma in a diverging magnetic field'. *Physics of Plasmas* 19.9 (2012). ISSN: 1070664X. DOI: 10.1063/1.4752074.

[60] L. T. Williams and M. L. Walker. 'Plume structure and ion acceleration of a helicon plasma source'. *IEEE Transactions on Plasma Science* 43.5 (2015), pp. 1694–1705. ISSN: 00933813. DOI: 10.1109/TPS.2015.2419211.

[61] C. Charles and R. W. Boswell. 'The magnetic-field-induced transition from an expanding plasma to a double layer containing expanding plasma'. *Applied Physics Letters* 91.20 (2007), pp. 2005–2008. ISSN: 00036951. DOI: 10.1063/1.2814877.

[62] K. Takahashi et al. 'Double-layer ion acceleration triggered by ion magnetization in expanding radiofrequency plasma sources'. *Applied Physics Letters* 97.14 (2010), pp. 2008–2011. ISSN: 00036951. DOI: 10.1063/1.3499653.

[63] F. N. Gesto et al. 'Ion Detachment in the Helicon Double-Layer Thruster Exhaust Beam'. *Journal of Propulsion and Power* 22.1 (2008), pp. 24–30. ISSN: 0748-4658. DOI: 10.2514/1.13914.

[64] A. Aanesland et al. 'Upstream ionization instability associated with a current-free double layer'. *Physical Review Letters* 97.7 (2006), pp. 1–4. ISSN: 00319007. DOI: 10.1103/PhysRevLett.97.075003.

[65] A. Aanesland et al. 'Experiments and theory of an upstream ionization instability excited by an accelerated electron beam through a current-free double layer'. *Physics of Plasmas* 13.12 (2006). ISSN: 1070664X. DOI: 10.1063/1.2398929.

[66] K Takahashi et al. 'Measurement of the energy distribution of trapped and free electrons in a current-free double layer'. *Physics of Plasmas* 14.11 (2007), p. 114503. ISSN: 1070664X. DOI: 10.1063/1.2803763.

[67] K. Takahashi et al. 'Radial characterization of the electron energy distribution in a helicon source terminated by a double layer'. *Physics of Plasmas* 15.7 (2008), p. 074505. ISSN: 1070664X. DOI: 10.1063/1.2959137.

[68] K. Takahashi et al. 'Transport of energetic electrons in a magnetically expanding helicon double layer plasma'. *Applied Physics Letters* 94.19 (2009), p. 191503. ISSN: 00036951. DOI: 10.1063/1.3136721.

[69] R. W. Boswell et al. 'Non-local electron energy probability function in a plasma expanding along a magnetic nozzle'. *Frontiers in Physics* 3.March (2015), pp. 1–5. ISSN: 2296-424X. DOI: 10.3389/fphy.2015.00014.

[70] C. Charles. 'High density conics in a magnetically expanding helicon plasma'. *Applied Physics Letters* 96.5 (2010), p. 051502. ISSN: 00036951. DOI: 10.1063/1.3309668.

[71] S. K. Saha et al. 'Plasma density accumulation on a conical surface for diffusion along a diverging magnetic field'. *Physics of Plasmas* 21.4 (2014), p. 043502. ISSN: 10897674. DOI: 10.1063/1.4870758.

[72] K. Takahashi et al. 'High temperature electrons exhausted from rf plasma sources along a magnetic nozzle'. *Physics of Plasmas* 24.8 (2017), p. 084503. ISSN: 10897674. DOI: 10.1063/1.4990110.

[73] N. Gulbrandsen and Å. Fredriksen. 'RFEA Measurements of High-Energy Electrons in a Helicon Plasma Device with Expanding Magnetic Field'. *Frontiers in Physics* 5.January (2017), pp. 1–8. ISSN: 2296-424X. DOI: 10.3389/fphy.2017.00002.

[74] S. Ghosh et al. 'Formation of annular plasma downstream by magnetic aperture in the helicon experimental device'. *Physics of Plasmas* 24.2 (2017), p. 020703. ISSN: 1070-664X. DOI: 10.1063/1.4975665.

[75] E. M. Aguirre et al. 'Spatial structure of ion beams in an expanding plasma'. *Physics of Plasmas* 24.12 (2017), pp. 0–12. ISSN: 10897674. DOI: 10.1063/1.5003722.

[76] K. Takahashi et al. 'Electron diamagnetic effect on axial force in an expanding plasma: Experiments and theory'. *Physical Review Letters* 107.23 (2011), pp. 1–4. ISSN: 00319007. DOI: 10.1103/PhysRevLett.107.235001.

[77] Y. Zhang, C. Charles and R. Boswell. 'Effect of radial plasma transport at the magnetic throat on axial ion beam formation'. *Physics of Plasmas* 23.8 (2016), p. 083515. ISSN: 10897674. DOI: 10.1063/1.4960828.

[78] Y. Zhang, C. Charles and R. Boswell. 'Measurement of bi-directional ion acceleration along a convergent-divergent magnetic nozzle'. *Applied Physics Letters* 108.10 (2016). ISSN: 00036951. DOI: 10.1063/1.4943583.

[79] C. M. Samuell et al. 'Plasma parameters and electron energy distribution functions in a magnetically focused plasma'. *Physics of Plasmas* 20.3 (2013). ISSN: 1070664X. DOI: 10.1063/1.4794841.

[80] M. J. Burin et al. 'On the transition to drift turbulence in a magnetized plasma column'. *Physics of Plasmas* 12.5 (2005), p. 052320. ISSN: 1070664X. DOI: 10.1063/1.1889443.

[81] S. Chakraborty Thakur et al. 'Suppression of drift wave turbulence and zonal flow formation by changing axial boundary conditions in a cylindrical magnetized plasma device'. *Physics of Plasmas* 20.1 (2013). ISSN: 1070664X. DOI: 10.1063/1.4775775.

[82] G. A. Navratil, J. Slough and A. K. Sen. 'A steady state linear machine for collisionless plasma studies'. *Plasma Physics* 24.2 (1982), pp. 185–196. ISSN: 00321028. DOI: 10.1088/0032-1028/24/2/006.

[83] D. M. Goebel, G. Campbell and R. W. Conn. 'Plasma surface interaction experimental facility (PISCES) for materials and edge physics studies'. *Journal of Nuclear Materials* 121.C (1984), pp. 277–282. ISSN: 00223115. DOI: 10.1016/0022-3115(84)90135-1.

[84] B. D. Blackwell et al. 'Design and characterization of the Magnetized Plasma Interaction Experiment (MAGPIE): A new source for plasma-material interaction studies'. *Plasma Sources Science and Technology* 21.5 (2012). ISSN: 09630252. DOI: 10.1088/0963-0252/21/5/055033.

[85] J. Santoso et al. 'Negative hydrogen ion production in a helicon plasma source'. *Physics of Plasmas* 22.9 (2015). ISSN: 10897674. DOI: 10.1063/1.4931469.

[86] M. Yoshitaka et al. 'Focusing magnetic field contribution for helicon plasma on Mini-RFTF'. *Thin Solid Films* 506-507 (2006), pp. 583–587. ISSN: 00406090. DOI: 10.1016/j.tsf.2005.08.063.

[87] F. F. Chen. 'Experiments on helicon plasma sources'. *Journal of Vacuum Science & Technology A: Vacuum, Surfaces, and Films* 10.4 (1992), pp. 1389–1401. ISSN: 0734-2101. DOI: 10.1116/1.578256.

[88] M. Krämer. 'Propagation and damping of m= +1 and m= -1 helicon modes in an inhomogeneous plasma column'. *Physics of Plasmas* 6.4 (1999), pp. 1052–1058. ISSN: 1070664X. DOI: 10.1063/1.873352.

[89] X. M. Guo et al. 'Helicon experiments and simulations in nonuniform magnetic field configurations'. *Physics of Plasmas* 6.8 (1999), pp. 3400–3407. ISSN: 1070664X. DOI: 10.1063/1.873580.

[90] V. F. Virko et al. 'Wave phenomena, hot electrons, and enhanced plasma production in a helicon discharge in a converging magnetic field'. *Physics of Plasmas* 11.8 (2004), pp. 3888–3897. ISSN: 1070664X. DOI: 10.1063/1.1764830.

[91] R. L. Stenzel and J. M. Urrutia. 'Whistler modes in highly nonuniform magnetic fields. III. Propagation near mirror and cusp fields'. *Physics of Plasmas* 25.8 (2018). ISSN: 10897674. DOI: 10.1063/1.5039355.

[92] W. D. Cox. 'Magnetic Steering of the Ion Beam in the Helicon Double Layer Thruster'. PhD thesis. The Australian National University, 2010.

[93] S. A. L. Dixon. 'Experimental Study of Expanding Hollow Cathode Discharges'. PhD thesis. The Australian National University, 2014.

[94] I. Langmuir and H. M. Mott-Smith. 'The Theory of Collectors in Gaseous Discharges'. *Physical Review* 28 (1926), pp. 727–763. ISSN: 0031-899X. DOI: 10.1103/PhysRev.28.727.

[95] F. F. Chen. 'Saturation ion currents to langmuir probes'. *Journal of Applied Physics* 36.3 (1965), pp. 675–678. ISSN: 00218979. DOI: 10.1063/1.1714200.

[96] N. Hershkowitz. 'How Langmuir probes work'. *Plasma diagnostics* 1 (1989), pp. 113–183.

[97] R. L. Merlino. 'Understanding Langmuir probe current-voltage characteristics'. *American Journal of Physics* 75.12 (2007), pp. 1078–1085. ISSN: 0002-9505. DOI: 10.1119/1.2772282.

[98] T. E. Sheridan. 'How big is a small Langmuir probe?' *Physics of Plasmas* 7.7 (2000), pp. 3084–3088. ISSN: 1070-664X. DOI: 10.1063/1.874162.

[99] Y. Zhang, C. Charles and R. W. Boswell. 'Density Measurements in Low Pressure, Weakly Magnetized, RF Plasmas: Experimental Verification of the Sheath Expansion Effect'. *Frontiers in Physics* 5.July (2017), pp. 1–6. ISSN: 2296-424X. DOI: 10.3389/fphy.2017.00027.

[100] M. J. Druyvesteyn. 'Der Niedervoltbogen'. *Zeitschrift für Physik* 64.11-12 (1930), pp. 781–798. ISSN: 0001-6489. DOI: 10.1007/BF01773007.

[101] M. J. Druyvesteyn and N Warmoltz. 'I. Energy balance, electron temperature, and voltage gradient in the positive column in mixtures of Na vapour with Ne, He, and Ar'. *The London, Edinburgh, and Dublin Philosophical Magazine and Journal of Science* 17.110 (1934), pp. 1–27. ISSN: 1941-5982. DOI: 10.1080/14786443409462366.

[102] V. A. Godyak, R. B. Piejak and B. M. Alexandrovich. 'Probe diagnostics of non-Maxwellian plasmas'. *Journal of Applied Physics* 73.8 (1993), pp. 3657–3663. ISSN: 00218979. DOI: 10.1063/1.352924.

[103] I. D. Sudit and F. F. Chen. 'Rf compensated probes for high-density discharges'. *Plasma Sources Science and Technology* 3.2 (1994), pp. 162–168. ISSN: 13616595. DOI: 10.1088/0963-0252/3/2/006.

[104] K. Takahashi. *Private communication*. 2016.

[105] V. I. Demidov et al. 'Probe measurements of electron energy distributions in a strongly magnetized low-pressure helium plasma'. *Physics of Plasmas* 6.1 (1999), pp. 350–358. ISSN: 1070664X. DOI: 10.1063/1.873288.

[106] V. A. Godyak and V. I. Demidov. 'Probe measurements of electron-energy distributions in plasmas: What can we measure and how can we achieve reliable results?' *Journal of Physics D: Applied Physics* 44.23 (2011), p. 233001. ISSN: 00223727. DOI: 10.1088/0022-3727/44/23/233001.

[107] V. I. Demidov, S. V. Ratynskaia and K. Rypdal. 'Electric probes for plasmas: The link between theory and instrument'. *Review of Scientific Instruments* 73.10 (2002), p. 3409. ISSN: 00346748. DOI: 10.1063/1.1505099.

[108] V. Godyak, R. Piejak and B Alexandrovich. 'Measurements of electron energy distribution in low-pressure R F discharges'. *Plasma Sources Science and Technology* 1 (1992), pp. 36–58. DOI: 10.1088/0963-0252/1/1/006.

[109] A. Fruchtman, D. Zoler and G. Makrinich. 'Potential of an emissive cylindrical probe in plasma'. *Physical Review E - Statistical, Nonlinear, and Soft Matter Physics* 84.2 (2011), pp. 1–4. ISSN: 15393755. DOI: 10.1103/PhysRevE.84.025402.

[110] G. D. Conway, a. J. Perry and R. W. Boswell. 'Evolution of ion and electron energy distributions in pulsed helicon plasma discharges'. *Plasma Sources Science and Technology* 7.3 (1999), pp. 337–347. ISSN: 0963-0252. DOI: 10.1088/0963-0252/7/3/012.

[111] C. Charles. 'Measurement and modeling of ion energy distribution functions in a low pressure argon plasma diffusing from a 13.56 MHz helicon source'. *Journal of Vacuum Science & Technology A: Vacuum, Surfaces, and Films* 10.2 (1992), p. 398. ISSN: 07342101. DOI: 10.1116/1.578063.

[112] A. Savitzky and M. J. Golay. 'Smoothing and Differentiation of Data by Simplified Least Squares Procedures'. *Analytical Chemistry* 36.8 (1964), pp. 1627–1639. ISSN: 15206882. DOI: 10.1021/ac60214a047.

[113] N. Gulbrandsen et al. 'A comparison of ion beam measurements by retarding field energy analyzer and laser induced fluorescence in helicon plasma devices'. *Physics of Plasmas* 22.3 (2015), p. 033505. ISSN: 10897674. DOI: 10.1063/1.4913990.

[114] W. Cox et al. 'Spatial retarding field energy analyzer measurements downstream of a helicon double layer plasma'. *Applied Physics Letters* 93.7 (2008), p. 071505. ISSN: 00036951. DOI: 10.1063/1.2965866.

[115] Y. Zhang. 'Transport Properties of Charged Particles in Low Pressure Plasmas'. PhD. Australian National University, 2016.

[116] Z. Harvey et al. 'Comparison of gridded energy analyzer and laser induced fluorescence measurements of a two-component ion distribution'. *Review of Scientific Instruments* 79.10 (2008), pp. 10–12. ISSN: 00346748. DOI: 10.1063/1.2953411.

[117] S. C. Thakur, A. Hansen and E. E. Scime. 'Threshold for formation of a stable double layer in an expanding helicon plasma'. *Plasma Sources Science and Technology* 19.2 (2010), p. 025008. ISSN: 09630252. DOI: 10.1088/0963-0252/19/2/025008.

[118] C Charles et al. 'Absolute measurements and modeling of radio frequency electric fields using a retarding field energy analyzer'. *Physics of Plasmas* 7.12 (2000), p. 5232. ISSN: 1070664X. DOI: 10.1063/1.1322557.

[119] L. Conde and L. León. 'Multiple double layers in a glow discharge'. *Physics of Plasmas* 1.8 (1994), pp. 2441–2447. ISSN: 1070-664X. DOI: 10.1063/1.870572.

[120] I. A. Biloiu and E. E. Scime. 'Temporal evolution of double layers in pulsed helicon plasmas'. *Applied Physics Letters* 95.5 (2009), pp. 3–5. ISSN: 00036951. DOI: 10.1063/1.3204014.

[121] Y. Zhang, C. Charles and R. Boswell. 'Transport of ion beam in an annular magnetically expanding helicon double layer thruster'. *Physics of Plasmas* 21.6 (2014). ISSN: 10897674. DOI: 10.1063/1.4885350.

[122] M. D. West, C. Charles and R. W. Boswell. 'Testing a Helicon Double Layer Thruster Immersed in a Space-Simulation Chamber'. *Journal of Propulsion and Power* 24.1 (2008), pp. 134–141. ISSN: 0748-4658. DOI: 10.2514/1.31414.

[123] K. Takahashi et al. 'Direct thrust measurement of a permanent magnet helicon double layer thruster'. *Applied Physics Letters* 98.14 (2011), p. 141503. ISSN: 0003-6951. DOI: 10.1063/1.3577608.

[124] T. Lafleur et al. 'Direct thrust measurements and modelling of a radio-frequency expanding plasma thruster'. *Physics of Plasmas* 18.8 (2011), pp. 1–4. ISSN: 1070664X. DOI: 10.1063/1.3610570.

[125] Y. Zhang, C. Charles and R. Boswell. 'Thermodynamic Study on Plasma Expansion along a Divergent Magnetic Field'. *Physical Review Letters* 116.2 (2016). ISSN: 10797114. DOI: 10.1103/PhysRevLett.116.025001.

[126] X. Sun et al. 'On-axis parallel ion speeds near mechanical and magnetic apertures in a helicon plasma device'. *Physics of Plasmas* 12.10 (2005), pp. 1–8. ISSN: 1070664X. DOI: 10.1063/1.2121347.

[127] A. Fruchtman et al. 'A magnetic nozzle calculation of the force on a plasma'. *Physics of Plasmas* 19.3 (2012). ISSN: 1070664X. DOI: 10.1063/1.3691650.

[128] T Lafleur, C Charles and R. W. Boswell. 'Electron temperature characterization and power balance in a low magnetic field helicon mode'. *Journal of Physics D: Applied Physics* 44.18 (2011), p. 185204. ISSN: 0022-3727. DOI: 10.1088/0022-3727/44/18/185204.

[129] K. Takahashi et al. 'Electron energy distribution of a current-free double layer: Druyvesteyn theory and experiments'. *Physical Review Letters* 107.3 (2011), pp. 1–4. ISSN: 00319007. DOI: 10.1103/PhysRevLett.107.035002.

[130] T. Schröder, O. Grulke and T. Klinger. 'The influence of magnetic-field gradients and boundaries on double-layer formation in capacitively coupled plasmas'. *EPL (Europhysics Letters)* 97.6 (2012), p. 65002. ISSN: 0295-5075. DOI: 10.1209/0295-5075/97/65002.

[131] S. Ghosh et al. 'Transition from single to multiple axial potential structure in expanding helicon plasma'. *Journal of Physics D: Applied Physics* 50.6 (2017), p. 065201. ISSN: 0022-3727. DOI: 10.1088/1361-6463/aa5068.

[132] W. Cox et al. 'Three-dimensional mapping of ion density in a double-layer helicon plasma'. *IEEE Transactions on Plasma Science* 36.4 PART 1 (2008), pp. 1386–1387. ISSN: 00933813. DOI: 10.1109/TPS.2008.924429.

[133] H. S. Butler and G. S. Kino. 'Plasma sheath formation by radio-frequency fields'. *Physics of Fluids* 6.9 (1963), pp. 1346–1355. ISSN: 10706631. DOI: 10.1063/1.1706905.

[134] K. Takahashi, A. Komuro and A. Ando. 'Operating a magnetic nozzle helicon thruster with strong magnetic field'. *Physics of Plasmas* 23.3 (2016). ISSN: 10897674. DOI: 10.1063/1.4943406.

[135] A. Simon. 'Ambipolar diffusion in a magnetic field'. *Physical Review* 98.2 (1955), pp. 317–318. ISSN: 0031899X. DOI: 10.1103/PhysRev.98.317.

[136] R. Chodura. 'Plasma-wall transition in an oblique magnetic field'. *Physics of Fluids* 25.9 (1982), pp. 1628–1633. ISSN: 10706631. DOI: 10.1063/1.863955.

[137] K. U. Riemann. 'Theory of the collisional presheath in an oblique magnetic field'. *Physics of Plasmas* 1.3 (1994), pp. 552–558. ISSN: 1070664X. DOI: 10.1063/1.870800.

[138] E. Ahedo. 'Structure of the plasma-wall interaction in an oblique magnetic field'. *Physics of Plasmas* 4.12 (1997), pp. 4419–4430. ISSN: 1070664X. DOI: 10.1063/1.872606.

[139] I. I. Beilis, M. Keidar and S. Goldsmith. 'Plasma-wall transition: The influence of the electron to ion current ratio on the magnetic presheath structure'. *Physics of Plasmas* 4.10 (1997), pp. 3461–3468. ISSN: 1070664X. DOI: 10.1063/1.872242.

[140] G. H. Kim et al. 'Magnetic and collisional effects on presheaths'. *Physics of Plasmas* 2.8 (1995), pp. 3222–3233. ISSN: 10897674. DOI: 10.1063/1.871153.

[141] A. Meige. 'Numerical modeling of low-pressure plasmas: applications to electric double layers'. PhD thesis. Australian National University, 2006.

[142] K. K. Barada et al. 'Wall charging of a helicon antenna wrapped plasma filled dielectric tube'. *Physics of Plasmas* 22.1 (2015), p. 013507. ISSN: 10897674. DOI: 10.1063/1.4906360.

[143] R. W. Boswell, E. Marsch and C. Charles. 'The Current-Free Electric Double Layer in a Coronal Magnetic Funnel'. *The Astrophysical Journal* 640.2 (2006), pp. L199–L202. ISSN: 0004-637X. DOI: 10.1086/503155.

[144] N. Krupp. 'New surprises in the largest magnetosphere of our solar system'. *Science* 318.5848 (2007), pp. 216–217. ISSN: 00368075. DOI: 10.1126/science.1150448.

[145] Y.-M. Wang and J. Frank. 'Plasma Infall and X-ray Production in the Magnetic Funnel of an Accreting Neutron Star'. *Astronomy and Astrophysics* 93 (1981), pp. 255–268.

[146] T. Lafleur, C. Charles and R. W. Boswell. 'Plasma control by modification of helicon wave propagation in low magnetic fields'. *Physics of Plasmas* 17.7 (2010). ISSN: 1070664X. DOI: 10.1063/1.3460351.